CHARACTERIZATION OF RARE EARTH PARTICLES FROM THE FLORIDA PHOSPHATE INDUSTRY THROUGH DUAL ENERGY RADIOGRAPHY AND X–RAY TOMOGRAPHY

by

Raquel Crossman

A thesis submitted to the faculty of
The University of Utah
in partial fulfillment of the requirements for the degree of

Master of Science

Department of Metallurgical Engineering

The University of Utah

December 2014

The University of Utah Graduate School

STATEMENT OF THESIS APPROVAL

The thesis of **Raquel Crossman**

has been approved by the following supervisory committee members:

Jan D. Miller , Chair **6/16/14** Date Approved

Chen–Luh Lin , Member **6/16/14** Date Approved

Raj Rajamani , Member **6/16/14** Date Approved

and by **Manoranjan Misra** , Chair/Dean of

the Department/College/School of **Metallurgical Engineering**

and by David B. Kieda, Dean of The Graduate School.

ABSTRACT

Mineral identification is an extremely important topic in metallurgical engineering, and rare earth particle identification grows increasingly important as national and global demand increases. Due to the small concentration wherein they are usually found in the Florida phosphate industry, particle identification methods often overlook, miscount, and do not adequately describe the rare earth particles in sample streams. In this regard, dual energy radiography followed by X–ray tomography is used to quantitatively identify rare earth particles and to establish their characteristics in selected samples. It is hypothesized that by combining these two methods, better data can be gathered to make an accurate accounting of the parts per million concentration of the minerals and that time can be saved by employing both processes instead of only using X–ray tomography, which would be one procedure for mineral identification and liberation analysis. To verify that the proposed methodology does as claimed, it was used to identify rare earth particles in three sample streams provided by the Florida Industrial and Phosphate Research Institute (FIPR). Each sample was separated by size, prepared, then scanned by dual energy radiography, thresholded, and prepared and scanned by high resolution X–ray microtomography. The results were then analyzed. Based on the final digital 3D reconstruction of the samples, it was concluded that this methodology was indeed faster and more time efficient than only X–ray tomography. It was also concluded that some additional data could be gathered from the preconcentration of the X–ray

tomography samples caused by preliminary dual energy radiography, but that data were dependent on the sample stream and not guaranteed for every sample scanned using this method. Therefore, it was finally concluded that the proposed methodology was time beneficial and that the potential additional data that could be gathered made this process worth exploring for future projects, especially if they involved identification of trace particles concentrated on a small, parts per million scale.

TABLE OF CONTENTS

CHAPTERS

APPENDICES

LIST OF TABLES

LIST OF FIGURES

ACKNOWLEDGEMENTS

I would like to take this opportunity to acknowledge the support given to me by the professors at the University of Utah. In particular, I wish to thank Dr. Miller and Dr. Lin for giving me this opportunity and their continual advice and direction throughout this process. I would like to acknowledge the support of the Florida Industrial and Phosphate Research Institute for providing the project samples and financial support. I would also like to thank fellow research students, Yan Wang and Ts.Tsend–Ayush, for their guidance in learning about this topic and aid in the progress of the project. Finally, as always, I would like to thank my family for their continual support throughout my academic career.

CHAPTER 1

INTRODUCTION

A topic of important recent discussion involves the proper identification and characterization of mineral resources. As more of the planet's mineral resources are used at quicker and quicker rates, it is essential to optimize the efficient processing and production of these resources. One of the best and most common ways to improve processing and efficiency is the proper characterization of the resources at hand.

Especially in recent years, the need to identify rare earth (RE) mineral deposits is growing increasingly more vital. RE oxides are used to produce a number of things, including automotive catalytic converters, phosphors in color television and flat panel displays (i.e. cell phones, laptops, etc.), permanent magnets, and a number of defense devices such as engines, guidance systems, satellites, and communication systems. Currently, China is responsible for approximately 97% of the world's RE production. As consumer demand grows, the production grows more and more inadequate. To help alleviate this, investigations have begun to evaluate RE minerals in phosphate rock, particularly in Florida. The hope is that the production of RE minerals in the United States can aide in the global shortage as well as lessen the nation's dependence on China for these products.

To identify, characterize, and quantify these RE minerals, there are a variety of methods available. The more traditional methods include elemental analysis done by X–

ray fluorescence (XRF), mineralogical analysis by X–ray diffraction (XRD), and mineral phase liberation analysis using automated scanning electron microscopy (SEM) such as QEMSCAN or MLA. However, although effective in their own ways, in all of these cases there are issues. These issues are mostly due to the sample alteration required for preparation and the limited two dimensional polished section information afforded with SEM. Sample preparation often involves destroying or altering the sample in order to accomplish the analysis. In the case of polished section analysis, the third dimension is always estimated, and so particle analysis has an indeterminable degree of error.

As a solution, in this thesis DE radiography is used to isolate trace RE particles of interest, followed by HRXMT in order to further identify and describe these particles. To demonstrate the efficiency of this method, the technique was used to identify and isolate RE phosphate particles in the shaking table concentrate, acid plant feed, and phosphogypsum samples provided by the Florida Industrial and Phosphate Research Institute.

This project is particularly fitting for the proposed method of analysis due to the general difficulty in identifying RE containing particles. As a whole, RE particles are complex and vary by a large degree in the chemical composition of the phases and often only appear in very small concentrations. This means that previous methods of identification may have overlooked significant amounts of RE particles (Smythe et al., 2013). By using DE radiography to first select which particles potentially contain RE elements and HRXMT to identify the spatial distribution within particles, significant time might be saved and new RE resources might be established. In order to fully understand the goals and results from this project, a thorough background of HRXMT and DE radiography, as well as the X–ray machine and software in use, are provided.

CHAPTER 2

BACKGROUND

To begin, a short background is provided for other traditional methods of resource identification. The techniques are introduced and explained and their flaws categorized in order to describe why the proposed methodology is an improvement on the existing methods. A brief introduction to the proposed methodology and a thorough background on the X–ray tomography machine that was used in this project is provided and then an in depth examination of the theory behind DE radiography and HRXMT follows. A background on the project is then provided as well as a discussion of the goals for the project and this thesis.

2.1 Methods for Resource Characterization

2.1.1 X–Ray Fluorescence

As in many of these methods, XRF sends X–rays through a sample and uses the outputted information to analyze the sample's elemental makeup. The idea behind XRF is that when X–rays enter the sample, "characteristic" or fluorescent X–rays are generated and released. A spectrometer measures either the wavelength of the fluorescent X–rays or the photon energy, depending on the preferred type of analysis, which is how the elemental analysis of the sample can be found (Beckhoff et al., 2006). The fluorescent X–rays are dependent on the excitation source intensity, concentration of the elements within the sample, and absorption properties of the sample (Markowicz, 2011).

This method is often considered precise and effective, but there are disadvantages. One problem is that the sample itself must be altered in order to examine it. The sample needs to show a flat surface without flaws to avoid problems due to absorption effects, which often requires polishing with an abrasive material. The accuracy of XRF often depends on the homogenous nature of the material as well. If the sample contains impurities or, in the case of individual particles, multiple mineral phases, the accuracy of XRF can decrease and could introduce errors and misidentification of the elemental makeup of the sample (Van Grieken and Markowicz, 2001).

2.1.2 X–Ray Diffraction

Similar to XRF, XRD bombards the sample with X–rays and measures the outputted information to determine the elemental composition. Unlike XRF, XRD is based on the reflection of the continuous X–rays and not the generation of characteristic X–rays. X–ray waves interact with each other, either constructively or destructively, based on the wave reflection in the crystal structure. The pattern of the waves created is recorded after they leave the crystal, which is called the diffraction pattern. The angle at which the diffracted waves hit the detector is also measured, as well as their intensities, and these values are used to determine the interatomic spacing that corresponds to different crystal structures (Rhodes, 2000).

XRD also has its limitations. Samples can only be accurately analyzed at low resolutions; otherwise, the propagation of the diffracted x–rays within the sample cannot be neglected and therefore the projection approximation cannot be used (Takahashi et al., 2010). Like XRF, a smooth, polished surface is required for XRD analysis. In the case of powder XRD, the sample must be ground into a fine powder before it can be analyzed (Dutrow and Clark, 2013).

2.1.3 Scanning Electron Microscopy

Unlike the previous method that uses a beam of X–rays to produce interpretable results, SEM uses a focused beam of electrons. The signals resulting from the electron–sample interactions can give detailed information about the texture, elemental composition, and crystalline structure of the sample. The electrons in the incident beam carry a high amount of kinetic energy, which dissipates in the sample with its interactions. The resulting signals include secondary electrons, backscattered electrons, diffracted backscattered electrons, photons, visible light, and heat. Each of these types of signals can produce different information about the sample. For example, diffracted backscattered electrons determine the crystalline structure, similar to XRD, and the photons are characteristic X–rays that provide elemental analysis.

The breadth of available analysis that can be provided by SEM makes it one of the most prominent and effective methods for sample analysis. However, it, too, is not without its own downfalls. SEM is only a two dimensional analysis, meaning that the sample must either be nearly completely flat or analysis in the third dimension can only be estimated. Estimation limits the accuracy of the analysis of the sample and a completely flat sample often requires alteration to the original sample. Additionally, samples must be dehydrated and coated by a conductive material in order to be examined (Radiological and Environmental Management, 2014).

2.2 Proposed Methodology

2.2.1 Methodology Introduction

As a solution to some of these problems and as an alternative analytical procedure, increasing interest and research has been given to high resolution X–ray microtomography (HRXMT). Similar to the upcoming field of high resolution X–ray diffraction microscopy, both methods involve taking 2D X–ray projections while rotating the sample about an axis normal to the beam and then using inverse problem solving techniques to reconstruct the 3D image (Chapman et al., 2006). However, instead of recording the far–field diffraction patterns, HRXMT involves using a computer to record the X–ray photons that are not absorbed by the sample. For this process, there is little done to prepare the sample. Nothing is done to actually change or damage the sample, making it a nondestructive testing technique. Also, because the sample is rotated a full 360° for full 3D reconstruction, there is little to no inaccuracy in the spatial description of the particles.

However, despite solving issues involved with other techniques, HRXMT has its own limitations. The biggest issue is the length of time necessary for each sample analysis to be completed. This is especially significant when searching for trace mineral particles, which are often only present on the parts per million (ppm) scale. This means that literally millions of particles must be analyzed in order to get a statistically reliable approximation of the particle concentration.

A solution to this particular problem that has been presented recently suggests that dual energy (DE) radiography can be used for resource identification. DE radiography involves taking two projections, one at high energy and one at low energy, and using the results of both scans to calculate the effective atomic number, leading to elemental analysis. The downfall to this method is that it is difficult to differentiate between particles of similar effective atomic numbers, leading to errors in the elemental analysis and particle identification.

2.2.2 X–Ray Machine

The University of Utah houses an Xradia MicroXCT–400 machine that was used to develop the analytical procedure (see Figure 2.1), and its user's manual (Xradia, 2010) is the primary source for the information provided in this section. The interior of the machine, shown in Figure 2.2, contains three main components: the X–ray source, sample stage, and detector. Figure 2.3 shows the orientation of axes which will be referenced in relation to the interior of the machine.

The X–ray source is a point source that generates X–rays in cone beam mode between 40 and 150 kV at a power between 4 and 10 W. The source also includes a

Figure 2.1. Xradia MicroXCT–400 machine, property of the University of Utah.

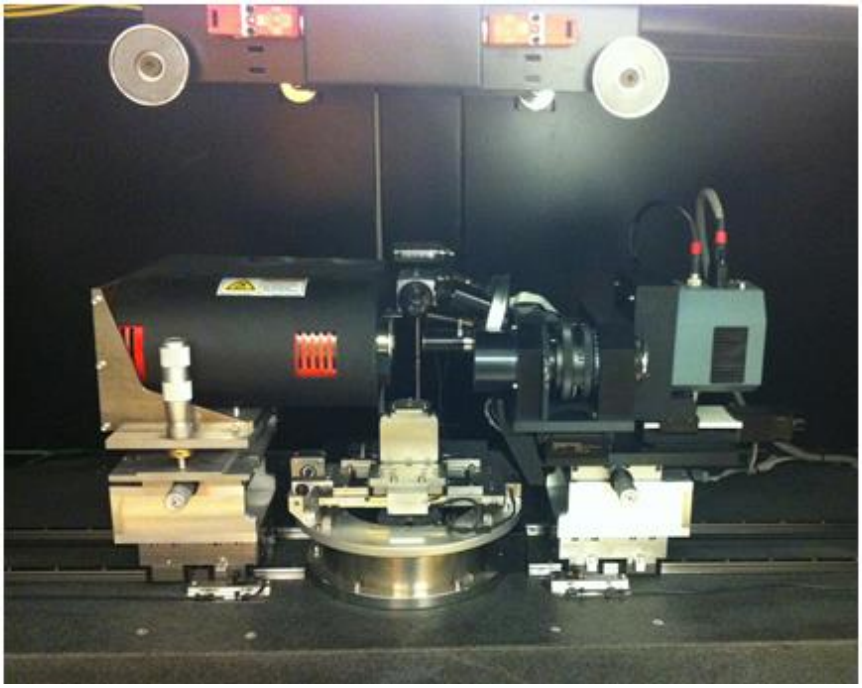

Figure 2.2. Interior of Xradia MicroXCT–400 machine. Note the X–ray source on the far left, the sample stage in the center, and the lens/detector at the far right.

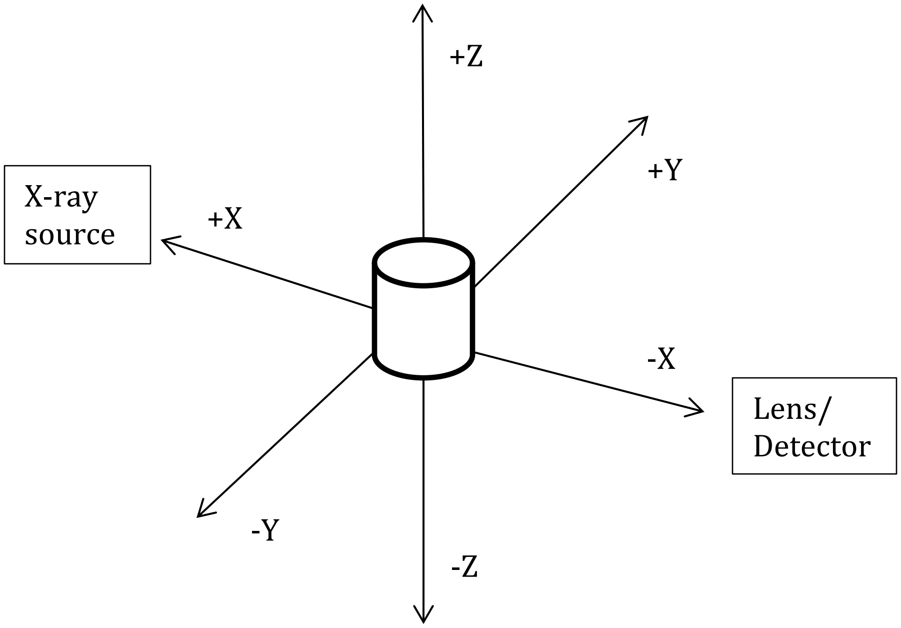

Figure 2.3. Axes orientation in relation to the interior of Xradia MicroXCT–400 machine.

holder for a filter that removes low–energy X–rays that do not provide any useful information about the sample, making the reconstructed image clearer. The source can be moved forward or backward on the +x axis to adjust the distance between the source and the sample stage, but not on the y or z axes.

The sample stage, as the name implies, is the platform where the sample is placed after it has been mounted. It can rotate through a full 360° and move in all three axial directions in micrometer precision. To mount a sample, it is simply clipped into place using the thumbscrew on one of the Xradia included mounts, shown in Figure 2.4.

The detector contains a turret upon which lenses of different magnification can be mounted. Table 2.1 shows the different lenses available on the University of Utah's machine, as well as their maximum resolutions and corresponding fields of view. The detector, through the chosen magnification lens, records X–rays after they have passed through the sample. Higher density material will absorb more X–rays, resulting in fewer X–rays being recorded at the detector and a darker image. This corresponds to particles with higher effective atomic numbers as well.

These three components are arranged according to conventional fan beam system principals, as shown in Figure 2.5. However, the X–ray beam extends as a cone in three

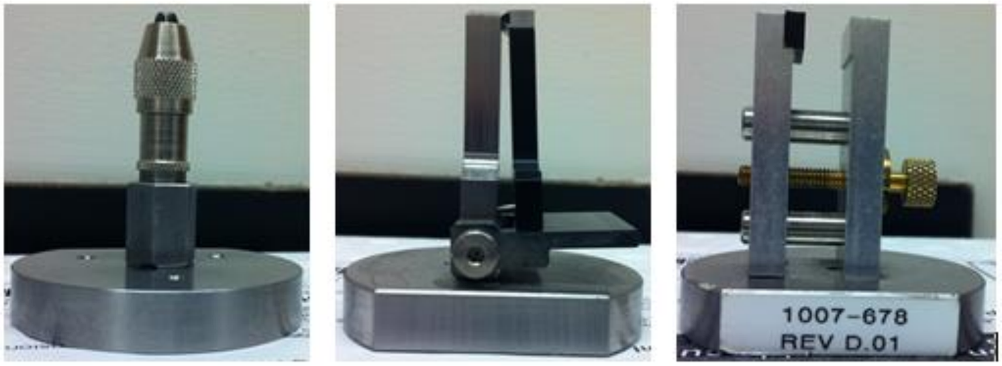

Figure 2.4. Three possible sample mounts included in Xradia machine.

Table 2.1. Lens magnification, corresponding resolution, and maximum field of view

Magnification	Resolution	Maximum field of view
0.5X	30 microns	40 mm x 40 mm
4X	4.5 microns	5 mm x 5 mm
10X	1.8 microns	2 mm x 2 mm
20X	1 microns	2 mm x 2 mm
40X	0.7 microns	1 mm x 1 mm

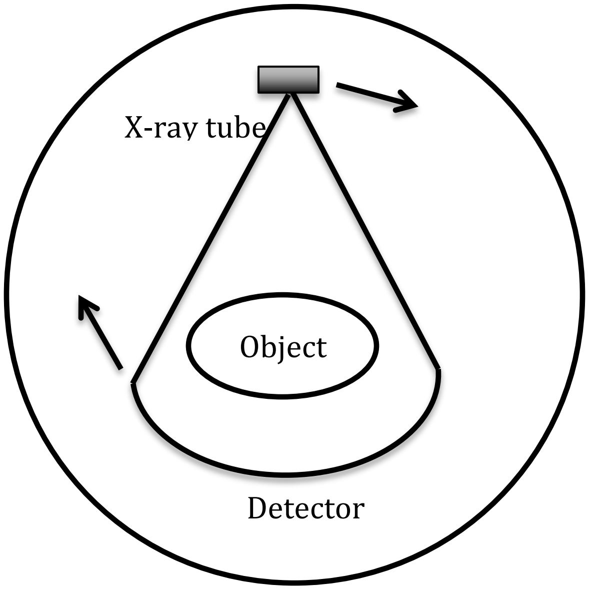

Figure 2.5. Traditional fan–beam system setup.

dimensions and not just two as a fan, and instead of the source and detector rotating around the sample, the sample itself rotates while the source and detector remain in place, as shown in Figure 2.6. Before the scan begins, the source and detector can be moved in the x–direction to gain a larger field of view, but this is also limited by the magnification and resolution desired. For larger samples that require a higher resolution image analysis, more than one scan must be done.

To aid in aligning the sample stage with the source and detector, a visual light camera is also included in the machine behind the sample stage at the back of the

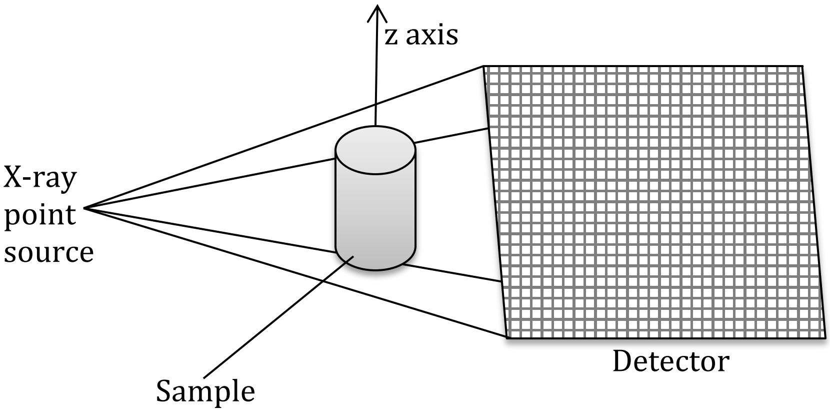

Figure 2.6. Cone beam setup, with sample rotating around z axis.

machine. As stated, the sample stage can be moved in all three axial directions in micrometer precision to position the sample correctly so that the desired field of view is obtained in the resulting image. The source, detector, and sample stage are all positioned using Xradia's included and attached software, XMController.

When the sample is arranged correctly and the scan ready to begin, the doors close using an interlock. When X–rays are actually being produced, the doors seal shut to prevent any radiation from escaping. This is done automatically by the machine so as to prevent any danger due to user neglect. Once the X–ray source is powered and aged, data acquisition can begin.

There are several types of data acquisition available using the MicroXCT–400 machine. The first is continuous mode. Collecting continuous images allows for fine–tuning the placement of the sample while X–rays are being produced. This gives a more exact idea of what the field of view on the sample will be in the final analysis. The exposure time for continuous mode is usually one second, and the images are generally not saved.

The next type of data acquisition is done in single mode. A single 2D image can be collected where the exposure time is user chosen. Single images can be used to simply see the internal structure of a sample without providing a detailed analysis of the material itself. A single image can also give a generalized “pretomography” idea of what the attenuation coefficient is at different points in the sample, which can provide a rough estimation of the materials contained within the sample without waiting for a full tomographical analysis. Single images can also be used for future reference in terms of sample positioning and scan conditions.

The averaging mode takes a number of single images and averages their results to give a more exact and accurate attenuation coefficient. There is only one resulting image, which can then be used for further analysis. The number of images to be averaged is user chosen, as well as the exposure time for each image.

In mosaic mode, a mosaic of images can be made. This large image is created by scanning the sample then tiling the images acquired at each scanned (x,y) location. This method provides an overview of the sample and can aid in seeing patterns in a specific area of interest. Once again, the exposure time is user chosen but is usually between 5 and 20 seconds.

It is important to note that in all of the modes mentioned above, it is a good idea to take a reference image and apply it to the final image before the data are analyzed. A reference image is acquired with the sample out of the field of view and is used to normalize the actual image by translating the intensity to a percentage of X–ray transmission. The settings used on the actual image should also be used for the reference image.

The last type of data acquisition available is tomography or multitomography. This mode rotates the sample from start angle to end angle while taking a user chosen number of images, each with user chosen exposure time. It is also possible to choose to take and apply multiple references automatically, each after a certain number of images have been collected. Reconstruction for 3D tomography can be done automatically by the software once all the data have been collected, or it can be done manually by the user at their leisure. The multitomography setting is essentially the same, except it is possible to do one tomography right after another. This mode is used when a larger sample needs a higher resolution and so the whole sample cannot be contained in the field of view.

2.2.3 Dual Energy Radiography

A thorough discussion of the theory behind dual energy radiography is helpful in fully understanding the proposed methodology. This is a brief summary of the theory discussed in the literature (Naydenov et al., 2003; Lin et al., 2013). As stated, the MicroXCT–400 records the X–rays that reach the detector after passing through the sample. Another way to think about this is in terms of the intensity, which is the number of photons per unit time and area. The photon intensity that hits the detector is related to the initial photon intensity by

$$I = I_o * \exp(-\mu(\rho, Z, E) * x) \tag{1}$$

where μ is the linear attenuation coefficient, which is dependent on the material's density (ρ), atomic number (Z), and energy of the X–ray beam I; x is the material thickness; I_o is the incident photon intensity; and I is the emerging photon intensity. This equation can be rearranged to give

$$\ln\left(\frac{I}{I_o}\right) = -\mu(\rho, Z, E) * x \tag{2}$$

It should be noted that equation 2 can be used, when written at two different energy levels, to solve for the thicknesses of two different materials that the same X–ray beam passes through. The model and approximate solution for this can be found in Appendix A. However, for the DE radiography that will be presented here, only a thin, single layer of particles will be used and so the thicknesses will not be calculated.

For the purposes of this research, the linear attenuation coefficient, μ, can be written in a somewhat simplified form as

$$\mu(E_i) = \rho[\alpha(E_i) + \beta(E_i)Z^p]Z, \text{ i = Low, High} \tag{3}$$

where α_i defines the energy dependence of the Compton effect and β_i defines the energy dependence of the photoelectric effect, and p is a number that accounts for how much of each effect is created. As is consistent with the form stated above, the linear attenuation coefficient is still directly dependent on the material density, effective atomic number, and the energy of the X–ray beam.

Now, the term *reflex* can be defined. For a specific energy level, E_i,

$$R(E_i) = R_i = \ln\left(\frac{I_{o,i}}{I_i}\right) \tag{4}$$

Therefore, substituting in equation 2 and 3, it is evident that

$$R(E_i) = \rho[\alpha(E_i) + \beta(E_i)Z^p]Z * x \tag{5}$$

which, rearranged again, gives

$$\frac{R(E_i)}{\rho x} = \mu_m(E_i) = [\alpha(E_i) + \beta(E_i)Z^p]Z \qquad (6)$$

where $\mu_{m,i} = \mu_i/\rho$ is the mass attenuation coefficient. Using this equation, it is possible to find the effective atomic number, Z, by defining a relative reflex as $X = \frac{R_1}{R_2}$.

This relative reflex does several important things. First, X is not dependent on either the thickness (x) or the density (ρ) of the material. This is easy to see by working through the mathematics:

$$X = \frac{R(E_1)}{R(E_2)} = \frac{\mu_m(E_1)\rho x}{\mu_m(E_2)\rho x} = \frac{\mu(E_1)x}{\mu(E_2)x} = \frac{\mu(E_1)}{\mu(E_2)}$$

Because X depends only on an attenuation coefficient, either mass or linear, the effective atomic number, therefore, can be found independent of knowing either thickness or density. The second thing X does is make it possible to actually solve for the effective atomic number:

$$Z_{eff} = \left(\frac{k_1 X + k_2}{k_3 X + k_4}\right)^{\frac{1}{p}} \qquad (7)$$

where the constants k_1, k_2, k_3, and k_4 are defined as

$$\begin{aligned} k_1 &= Z_1^p Z_2^p (X_1 - X_2) - Z_1^p Z_3^p (X_1 - X_3) + Z_2^p Z_3^p (X_2 - X_3) \\ k_2 &= X_1 X_2 Z_3^p \left(Z_1^p - Z_2^p\right) - X_1 X_3 Z_2^p \left(Z_1^p - Z_3^p\right) + X_2 X_3 Z_1^p \left(Z_2^p - Z_3^p\right) \\ k_3 &= X_1\left(Z_2^p - Z_3^p\right) - X_2\left(Z_1^p - Z_3^p\right) + X_3(Z_1^p - Z_2^p) \\ k_4 &= X_1 X_2 \left(Z_1^p - Z_2^p\right) - X_1 X_3 \left(Z_1^p - Z_3^p\right) + X_2 X_3 \left(Z_2^p - Z_3^p\right) \end{aligned} \qquad (8)$$

and X_1, X_2, and X_3 are the relative reflexes of three known materials, and Z_1, Z_2, and Z_3 are their known effective atomic numbers. The process of calculating the constants k_1, k_2,

k_3, and k_4 and the plotting of the function $Z_{eff}(X)$ is known as calibration. This process of calibration allows for elements to be chosen specific to the minerals of interest, as widespread or narrow as desired.

While it might seem like DE radiography is an ideal solution to particle identification, it is not without its own flaws. Using this method, it is easy to differentiate between elements with a large difference between their effective atomic numbers; for example, it is easy to tell the difference between quartz ($Z_{eff} = 11.8$) and gold ($Z_{eff} = 79.0$). However, for minerals with closer atomic numbers, such as quartz ($Z_{eff} = 11.8$) and aluminum ($Z_{eff} = 13.0$), it is nearly impossible to differentiate between them using DE radiography. Because elements are rarely found in pure form, it is therefore a molecular compound that the effective atomic number is referring to, and because of all the possible combinations of elements in compounds, this effective atomic number is not unique to a single mineral. This is demonstrated visually with Figure 2.7. There is some obvious overlapping between minerals with close effective atomic numbers. This means that although the relative reflex can be found for a particle and an effective atomic number calculated, there is no guarantee for which compound those then refer to.

Because DE radiography is based on the experimental analysis of the measured attenuation coefficient versus known effective atomic numbers, there is some degree of error. This is evident in Figure 2.7 as well. Notice that each compound does not have a single relative reflex or effective atomic number, but rather a range for both values. This is because different calibrations result in different relative reflexes mapping to different effective atomic numbers. Therefore, DE radiography cannot be seen as giving the absolute effective atomic number, but rather an approximation that needs to be verified

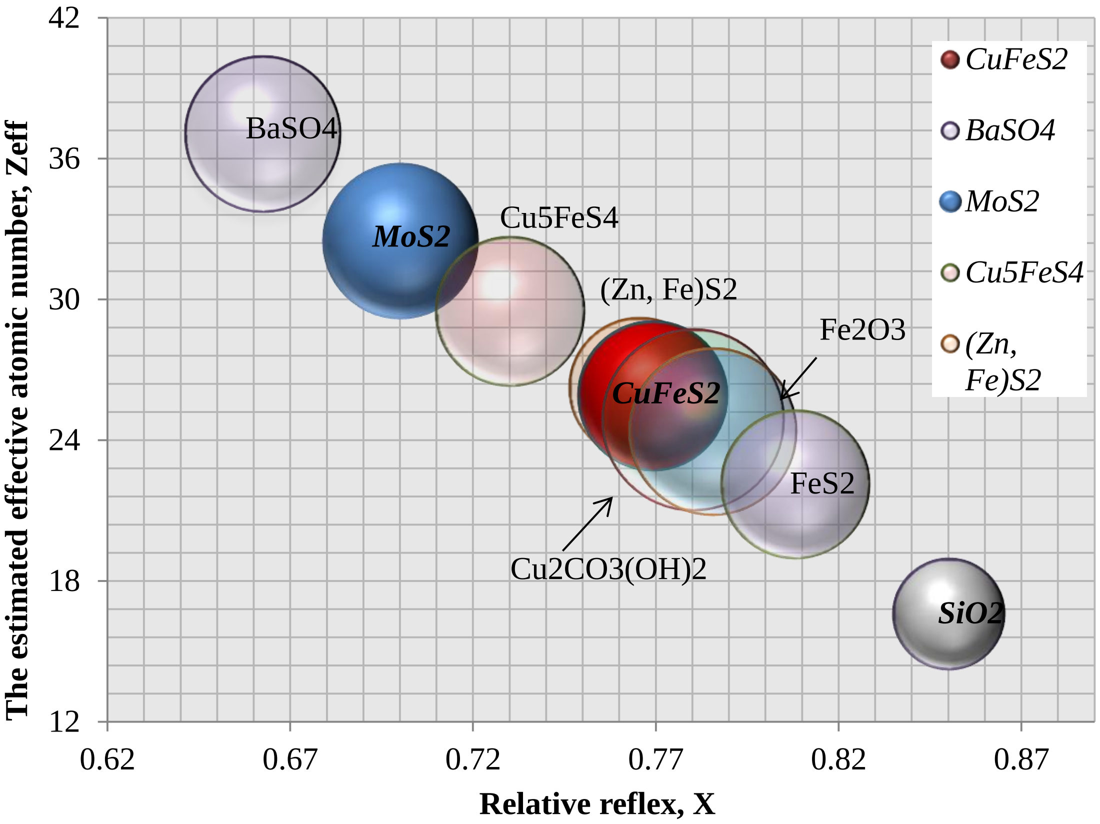

Figure 2.7. Graph relating the relative reflex to the effective atomic number. Note that more than one X value leads to the same element and that the some of the same X values lead to different elements.

using a more accurate system.

Because DE radiography uses X–rays to determine the attenuation coefficients, it is very dependent on the ability of the X–rays to penetrate the sample. This means that for higher density materials, the machine in use may not be able to produce X–rays with a high enough energy to go completely through the sample. This, therefore, further limits which compounds can be identified using DE radiography. It is recommended for the MicroXCT–400 in use that for effective atomic numbers greater than 40 that DE radiography be used to identify only semiquantitatively particles of interest and a secondary method be used after DE radiography for a more complete analysis.

2.2.4 High Resolution X–Ray Microtomography

As this thesis evaluates the use of high resolution X–ray microtomography (HRXMT) as the follow up method to DE radiography, a comprehensive background on HRXMT is also needed. As with DE radiography, this is a summary of the concepts presented in the related literature (Rosenfeld and Kak, 1982; Cho et al., 1993). As stated, in the case of the MicroXCT–400, HRXMT involves sending a cone beam X–ray of a set energy level at the sample and recording the photons that emerge on the other side. To ensure complete accuracy, the sample is rotated a full 360°**,** and the projections recorded a user set number of times using the tomography mode on the machine.

To reconstruct the sample in 3D from 2D projections, several mathematical concepts are applied. The software included in the Xradia MicroXCT–400 machine can run through this math and corresponding algorithms with minimal input from the user, but to fully understand how it is possible to go from 2D projections to a 3D object, I found it extremely useful to work through the concepts step by step. Therefore, I will first walk through some of the math behind the reconstruction then go through the steps for using the software. The step by step breakdown of the mathematics behind what will be presented can be found in Appendix B.

The first concept to work through is realizing that the act of sending X–rays through a sample and recording the photon intensities that emerge as attenuation coefficients can be considered a series of Radon transforms. The Radon transform is defined as the line integral of a function along a line that is parallel with the y'–axis at a distance x' from the origin, where (x', y') are the rotated coordinates of (x, y) through an angle φ. Mathematically, this is denoted as

$$p_{\varphi}(x') = \Re[f(x,y)] = \int_{-\infty}^{\infty} f(x'\cos\varphi - y'\sin\varphi\,, x'\sin\varphi + y'\cos\varphi)\,dy' \quad (9)$$

In terms of HRXMT, each 2D cross sectional slice of the sample can be considered a different f(x,y) and the corresponding 1D slice on the projection image as $p_{\varphi}(x')$. This can be seen visually in Figure 2.8. The attenuation coefficients are the resulting values from the line integrals and each φ corresponds to the next angle 360°/n from the last, where n is the user chosen number of projections to be taken.

Considering the projections as Radon transformations is the fundamental concept behind the 3D reconstruction. Before discussing the next essential theorem, a brief recap of Fourier transforms is necessary. Fourier transforms take functions at a given angle and transforms them into values on the Fourier frequency domain at the same angle. 1D Fourier transforms take functions of one dimension and plots them as a point. 2D Fourier transforms take functions of two dimensions and maps them as a two dimensional line in the frequency domain. This can be seen more easily with a visual representation, shown in Figure 2.9. Likewise, 3D Fourier transforms takes three dimensional shapes to a sphere, but as this is harder to picture two dimensionally, it is not shown. Fourier transforms lie at the heart of reconstructing images, and so understanding completely

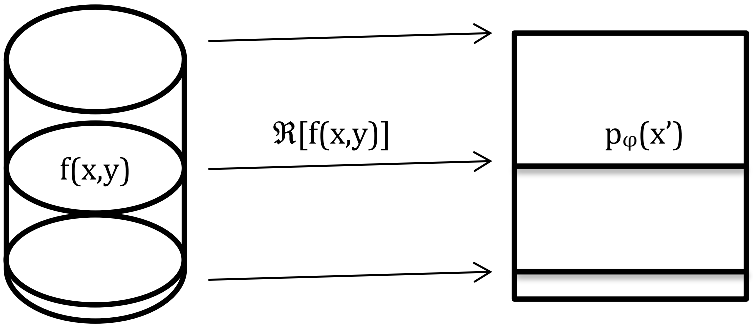

Figure 2.8. Depiction of transforming 2D cross sectional area into 1D line using a series of Radon transforms.

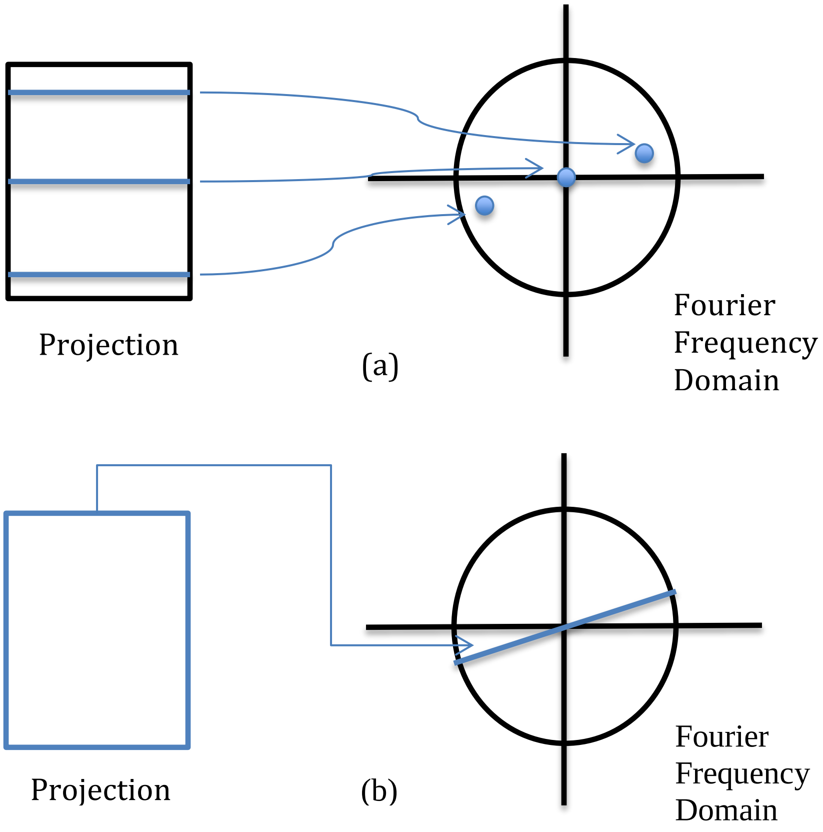

Figure 2.9. Visual representation of Fourier transforms at a given angle φ (a) showing the 1D transform from a one dimensional line to a point and (b) showing the 2D transform from a box to a two dimensional line.

how they work is absolutely necessary. The next mathematical concept and the basis of all image reconstruction is the Projection Theorem or Fourier Slice Theorem, which will be given first in 2D then extrapolated to 3D. The basis of this theorem is that the 2D Fourier transform of f(x,y) is the same as the 1D Fourier transform of the projection data $p_{\varphi}(x')$. Visually, this can be seen by Figure 2.10 and mathematically by equation set 10,

$$\begin{aligned} P_{\varphi}(\omega) &= \mathcal{F}_1\left[p_{\varphi}(x')\right] = \int_{-\infty}^{\infty} p_{\varphi}(x') \exp(-i\omega x')\, dx' \\ &= \iint_{-\infty}^{\infty} f(x,y) \exp[-i\omega(x\cos\varphi + y\sin\varphi)]\, dx\, dy \\ &= F\left(\omega_x, \omega_y\right)\big|_{\varphi} = F(\omega,\varphi) = \mathcal{F}_2[f(x,y)] \end{aligned} \tag{10}$$

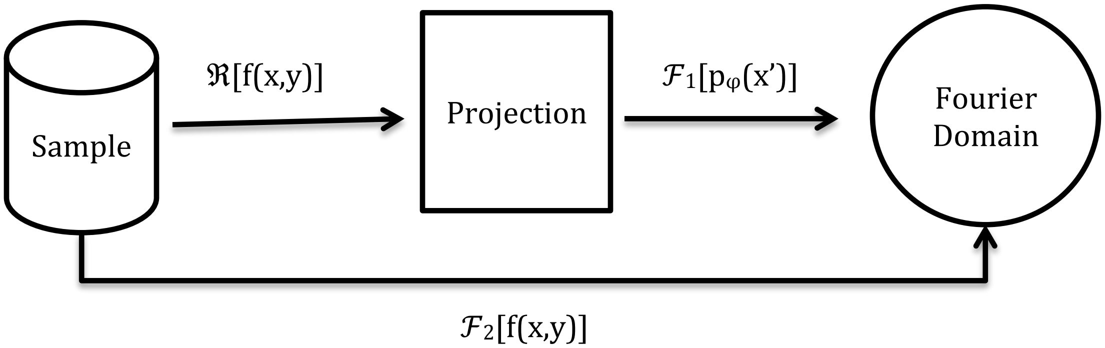

Figure 2.10. Visual representation showing that the 1D Fourier transform of the projections data is the same as the 2D Fourier transform of the original sample.

where $F(\omega_x, \omega_y)$ represents Cartesian coordinates and $F(\omega, \varphi)$ represents polar coordinates in the Fourier domain. By rotating the sample and taking projections at certain intervals, with each projection corresponding to a line in the Fourier domain, the whole domain can be mapped, demonstrated in Figure 2.11. This theorem is important because it provides a way to get back to the original object by applying a 2D inverse Fourier transform after the 1D Fourier transform has been applied to the projection data. Again, this can be seen visually in Figure 2.12 and mathematically in equation set 11.

$$\hat{f}(x,y) = \mathcal{F}_2^{-1}\left[F\left(\omega_x, \omega_y\right)\right] = \iint_{-\infty}^{\infty} F\left(\omega_x, \omega_y\right) \exp\left[i\left(x\omega_x + y\omega_y\right)\right] d\omega_x d\omega_y \qquad (11)$$
$$= \hat{f}(r,\theta) = \int_0^{\pi} \int_0^{\infty} F(\omega, \varphi) \exp[i\omega(x\cos\varphi + y\sin\varphi)]\,|\omega| d\omega\, d\varphi$$

As mentioned, the 2D Fourier Slice Theorem can be extrapolated to 3D relatively easily. In terms of three dimensions, the theorem essentially says that the Fourier transform of 2D projection data corresponds to the original object function going through a 3D Fourier transform. Therefore, taking the 2D projection data as $p_{\theta,\varphi}(s,t)$, this is represented in the formula as

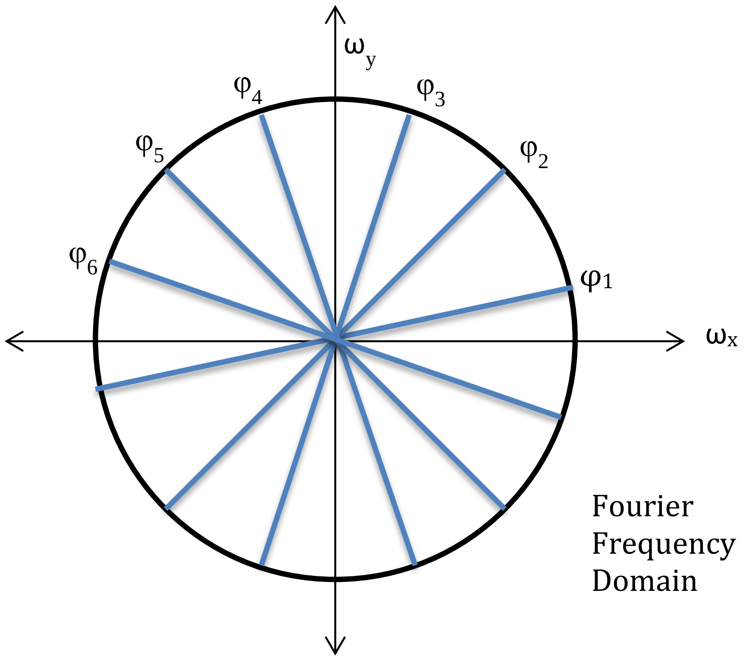

Figure 2.11. By taking projections of the sample at set angles between 0° and 360° and taking the 1D Fourier transform of each projection, the entire Fourier frequency domain can be mapped.

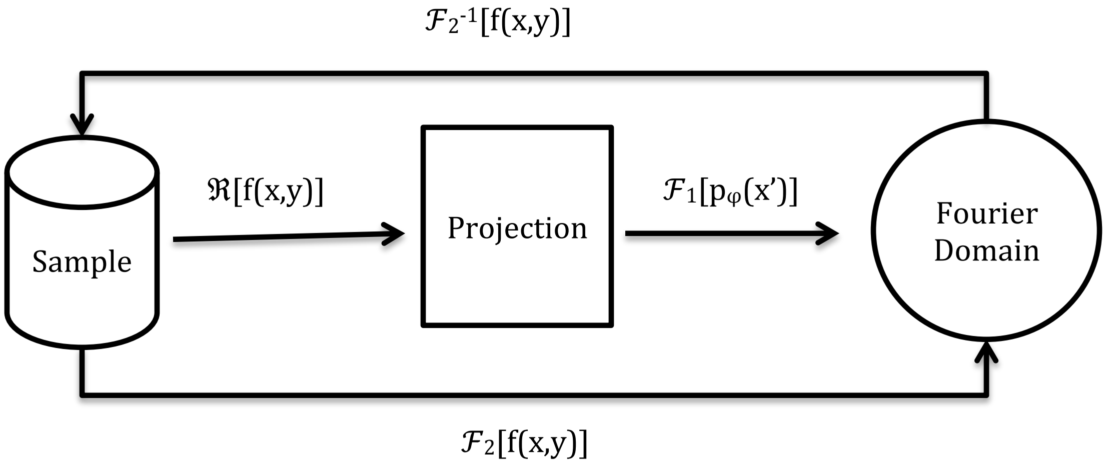

Figure 2.12. Visual representation of reconstructing the original sample by applying a 1D Fourier transform then a 2D inverse Fourier transform.

$$\mathcal{F}_2\left[p_{\theta,\varphi}(s,t)\right] = F(\omega_s, \omega_t; \theta, \varphi) \tag{12}$$

and leads to the final 3D algorithm

$$f(x,y,z) = \frac{1}{4\pi^2}\int_0^{\pi} d\theta \cos\theta \int_0^{2\pi} d\varphi \left[\mathcal{F}_2^{-1}[\rho] ** p_{\theta,\varphi}(s,t)\right] \tag{13}$$

where ρ is a filter to counteract the traditional 1/r blur when $\rho = (\omega_s^2 + \omega_t^2)^{1/2}$ and ** indicates a 2D convolution operator.

As already mentioned, the software attached to the MicroXCT–400 goes through these algorithms in the program XMReconstructor. The first step to use this program is to open the projection file in the program and find the center shift. Sometimes when taking the projections, the field of view is not exactly centered on the y–axis that the sample rotates on. This causes artifacts to appear, as seen in Figure 2.13, and so the program allows for shifting the center to correct it. Once the center shift has been determined, the reconstruction can begin by inputting values for the file name, center shift, beam hardening, and mineral standard, if desired. The window for this is shown in Figure 2.14.

The beam hardening value accounts for two things. The first is the X–rays that are emitted at different energy levels due to the polychromatic source. While the glass filter usually used in the machine takes care of some of these by stopping far lower X–rays from going through the sample, there are still X–rays present at differing energy levels, both lower and higher than desired. Because, as discussed in section 2.2.3, the attenuation coefficient is dependent on the energy level E, these X–rays at energy levels other than the desired one must be accounted for in the reconstruction. The second thing beam hardening accounts for is the different distances each X–ray travels before reaching the sample. Because the MicrotXCT–400 emits X–rays in cone beam mode, the X–rays

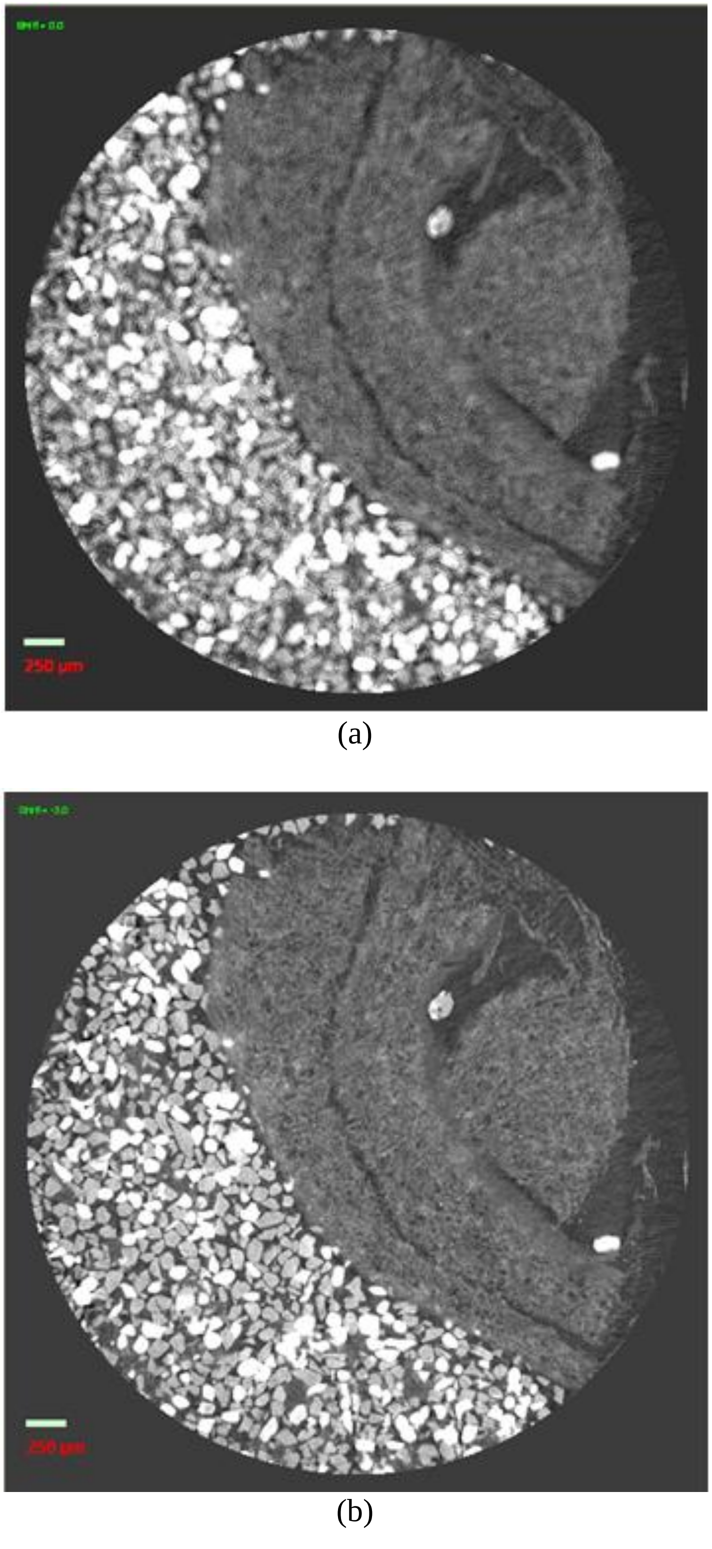

Figure 2.13. Image slice from shaking table concentrate, demonstrating in (a) what the sample reconstruction looks like without a center shift and in (b) what the sample reconstruction looks like with the correct center shift of –3. Note the blurriness and artifacts that appear in image (a) but disappear in image (b).

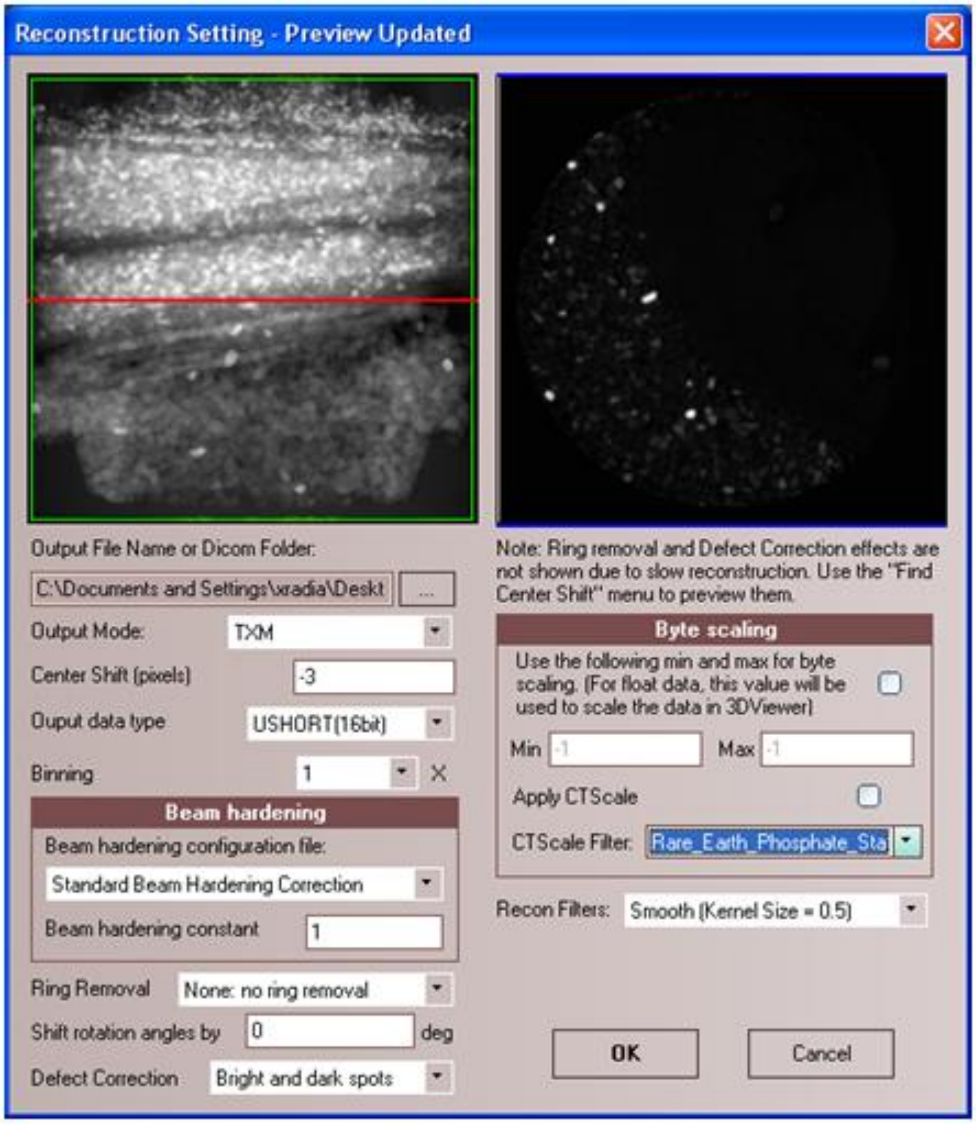

Reconstruction Setting - Preview Updated

Output File Name or Dicom Folder: C:\Documents and Settings\xradia\Deskt

Output Mode: TXM

Center Shift (pixels) -3

Ouput data type USHORT(16bit)

Binning 1

Beam hardening

Beam hardening configuration file: Standard Beam Hardening Correction

Beam hardening constant 1

Ring Removal None: no ring removal

Shift rotation angles by 0 deg

Defect Correction Bright and dark spots

Note: Ring removal and Defect Correction effects are not shown due to slow reconstruction. Use the "Find Center Shift" menu to preview them.

Byte scaling

Use the following min and max for byte scaling. (For float data, this value will be used to scale the data in 3DViewer) ☐

Min -1 Max -1

Apply CTScale ☐

CTScale Filter: Rare_Earth_Phosphate_Sta

Recon Filters: Smooth (Kernel Size = 0.5)

Figure 2.14. Reconstruction window to input desired settings. The most important values to input are the file name, center shift, beam hardening constant, and CT scale filter.

travelling directly along the x– and z–axes to the sample go the shortest distance and the X–rays going through the top, bottom, far left, and far right of the sample travel the farthest. Again, as discussed in section 2.2.3, because the X–ray intensity, and therefore the attenuation coefficient, depends on the distance the photon passes through, the differing distances must be accounted for in the reconstruction as well. These are both handled in the beam hardening value.

The mineral standard aids in the identification of desired particles. The MicroXCT–400 uses a global scale to establish scaled CT numbers for each voxel of the sample image. This means that each voxel is numbered in relation to each other's attenuation coefficient, from the minimum to the maximum. However, when dealing with a sample that has both low and high densities, the numbers between are compressed, and the contrast between particles significantly reduced. A mineral standard adjusts the scale by allowing the CT numbers of air and the mineral of interest to be inputted and then adjusting the scale accordingly. To establish a standard, a pure, homogenous sample consisting of a single phase of the desired mineral is scanned with the same settings the unknown sample is going to be scanned with in the future. The globally scaled CT number for the whole sample is calculated and inputted along with the globally scaled CT number for air. When the standard is applied, it uses these values to adjust the scale of the sample and make the contrast between particles more clear.

After these values have been decided and entered into the window, the reconstruction proceeds automatically. This file can then be saved under a number of extensions, including .txm, .bin, and .raw, and can be viewed by several programs, including XMController (Xradia, 2010), TXM3DViewer (Xradia, 2010), ImageJ (Rasband, 2014), MIPAV (McAuliffe, 2012), and Drishti (Limaye, 2006). It can be viewed as either 2D slices on the XY plane, shown in Figure 2.15, or as a complete 3D figure, as in Figure 2.16. Altogether, the reconstruction process takes about 20 minutes to complete. From here, a number of things can be determined, including the number of particles of a certain type within the given sample, which is of particular interest for this thesis as described below.

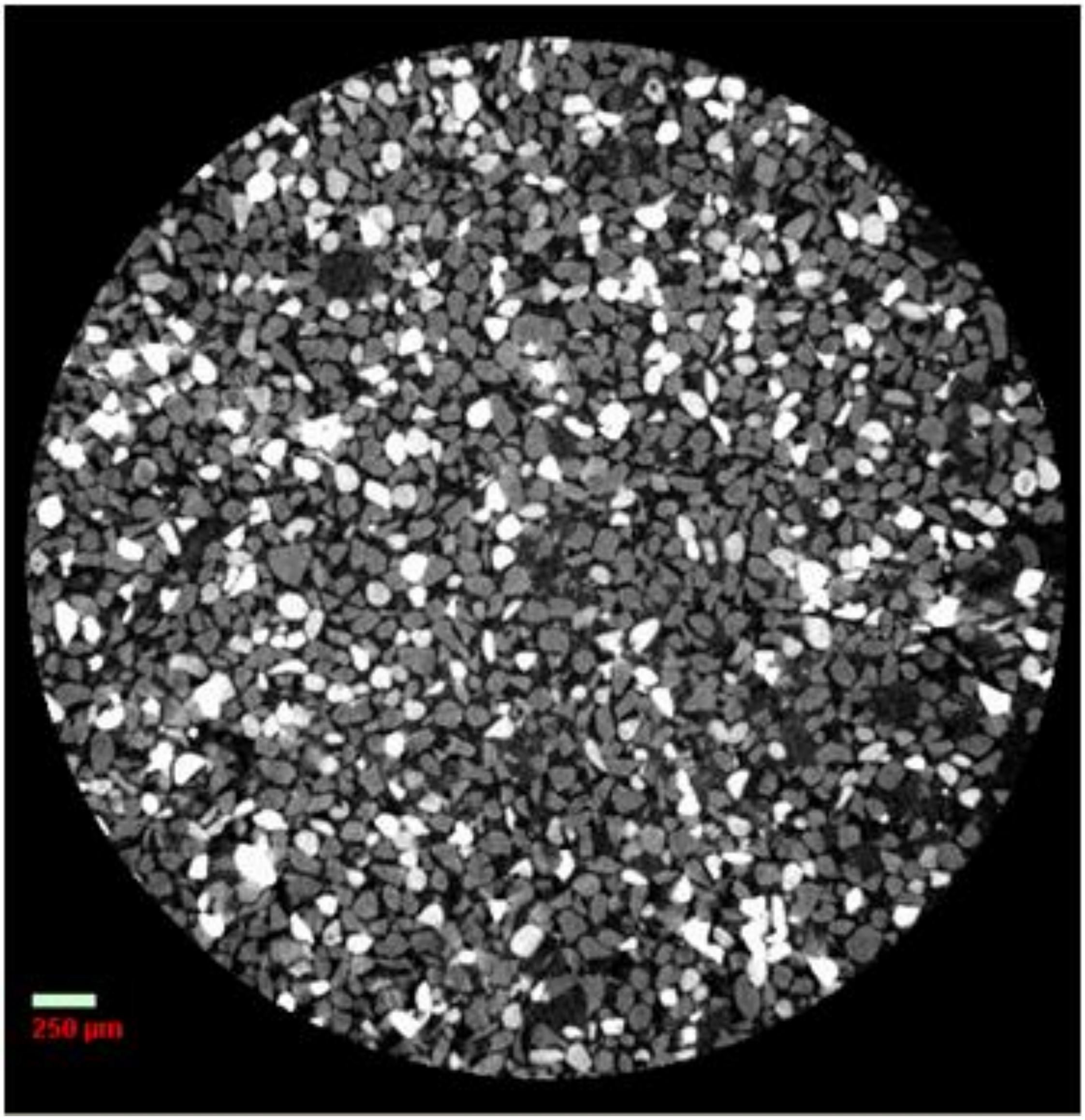

Figure 2.15. An example of a 2D image slice of shaking table concentrate taken from a 3D reconstruction using XMController.

Figure 2.16. Volume rendering from 3D reconstructed image set, created using Drishti.

2.3 Justification and Thesis Goals

RE oxides are used to produce a number of things, including green energy devices like electric motors and solar cells, electronics like fiber optics and lasers, magnetics like disk drives and refrigeration, medical equipment like MRI machines and surgical tools, and lightings like flat screen TVs and cell phone screens.

In the US, between 2002 and 2010, about 5 to 11 kilotons of RE oxides were consumed each year, the majority of which were imported. Globally, it is estimated that the demand for RE elements will reach 160,000 metric tons by 2016. About 97% of the world's RE production comes from China, making the global supply chain almost entirely dependent on China and subjective to its political and economic disputes and whims. In addition to this, with increasing global demands it is also predicted that there will be a shortage of RE elements produced (Humphries, 2013).

In order to change this and satisfy the demands for RE production in the United States, the Florida Industrial and Phosphate Research Institute decided to investigate the recovery of RE minerals from phosphate rock. In a preliminary study, RE particles were found to be distributed in Florida phosphate rock in the product, waste clay material, and flotation tailings on a parts per million (ppm) scale.

As stated briefly in the introduction, the purpose of this project is to identify phosphate RE particles from concentrate and tailing samples from the Florida Industrial and Phosphate Research Institute. This method of using DE radiography to identify potential RE particles and then using HRXMT to follow up on chemical composition and liberation analysis was chosen because of the difficulty in identifying RE particles using traditional methods. The combination of DE radiography and HRXMT was chosen to make the process less time consuming

A goal of this thesis research was to obtain an accurate accounting of RE particles in concentrate and tailing samples of phosphate rock. In addition, liberation analysis on the RE particles were to be calculated based on the HRXMT scans to determine if any helpful information can be gathered. For purposes of this thesis, the times required for each scan and the number of particles that can be scanned in a given time frame were also recorded and compared to projects completed by only HRXMT. The liberation information was also compared to determine if the concentration of RE particles produced by the preliminary DE radiography is more beneficial than liberation information provided by HRXMT alone without preconcentration. Based on the results gathered from the project, it was determined if the proposed methodology should be used in the future for more effective and efficient resource identification and characterization.

CHAPTER 3

EXPERIMENTAL PROCEDURES

3.1 Step 1: Particle Separation by Size

To begin the procedure, each sample was first divided into size classes. Separating the samples into sizes is important for several reasons. The first has to do with the X–ray scans, from both the DE radiographs and the HRXMT images. Particles that are too small can cause the images to come out “fuzzy” and “blurry” because the edges of the particles cannot be made distinct unless the magnification is large enough. In order to make sure that the proper magnification is used for each particle size, they must be separated by size. Knowing the size of the particles is also useful for the liberation analysis. By knowing the particle size and the degree of liberation, the average size of RE minerals and how fine the particles should be for liberation of the RE minerals can be determined.

Initially, the Florida Industrial and Phosphate Research Institute (FIPR) only sent two samples: shaking table concentrate and acid plant feed. About a kilogram of each sample was received, and sieve sizes were decided based on visual examination by Dr. Lin and myself. The sieve sizes chosen were 140 mesh (106 μm), 200 mesh (75 μm), and 270 mesh (53 μm). Due to the amount of each sample to be separated, a preliminary separation was done by dry sieving on a vibrating sieve shaker (see Figure 3.1).

There was some initial difficulty in determining how much of each sample could

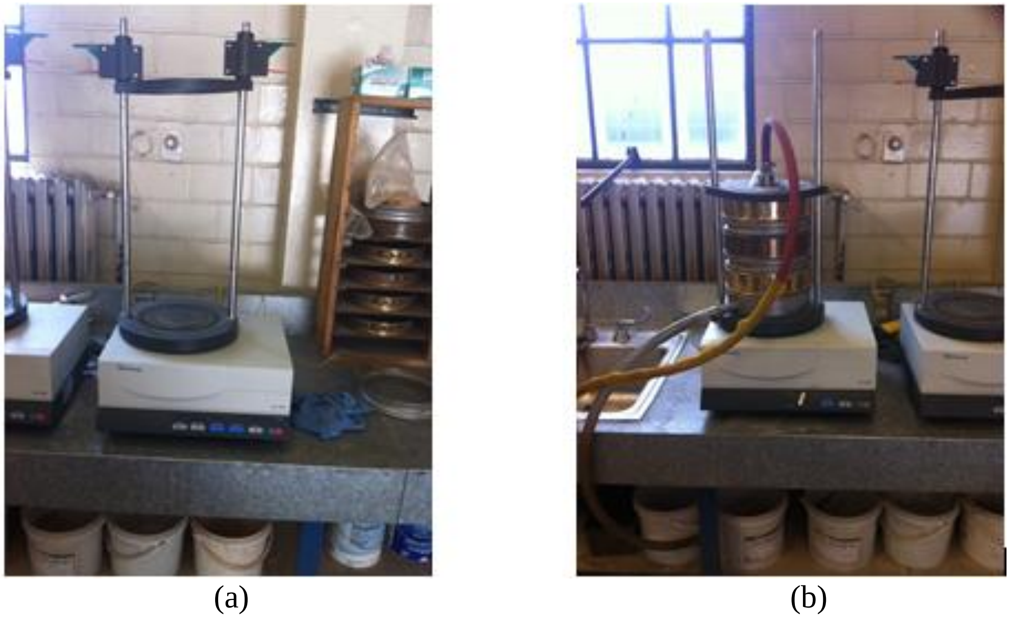

(a) (b)

Figure 3.1. Vibrating sieve shaker (a) without sieves in place and (b) set up for wet sieving process.

be sieved at once, but after consulting with some other graduate students who used the vibrating sieve shaker regularly it was determined that about 100 g could be screened at a time to ensure good separation. As a dry sample, each 100 g batch was shaken for 20 minutes. This time was recommended by a fellow researcher, who had much more experience using the vibrating sieve shaker, as the time that allowed for optimum separation of a dry sample. Each size fraction then underwent wet sieving for a more thorough separation. A 100 g batch was first mixed with water in a flask then, using the same sieves and vibrating sieve shaker, separated while running a continuous stream of water through the sieves. This was done for 8 minutes, the time that was recommended by the previous researcher. After each batch of wet sieving, the samples were dried in an oven (see Figure 3.2) at approximately 100 °C. Once dry, it was collected out of the sieves using brushes and each size fraction for each sample placed in its own bag.

Doing this process took an extremely long time in order to separate the entire bulk

(a) (b)

Figure 3.2. (a) Outside and (b) inside view of the oven used to dry samples after wet sieving.

of sample. This was primarily due to sharing the vibrating sieve shaker with several other researchers. Because we all had to share and be considerate of each other's project deadlines, I was only able to run one or two batches a day, and sometimes none at all. It also took longer because of the double separation of dry and wet sieving.

Because of the length of time required for this process, when the third sample of phosphogypsum arrived, an alternate method was used. After consulting with Dr. Miller, it was decided to use coning and quartering instead of dry sieving. Coning and quartering was completed by pouring the entire bulk sample into a cone (Figure 3.3a) then pressing it flat (Figure 3.3b). The sample was then divided into quarters (Figure 3.3c) and two kitty corner sections chosen to continue (Figure 3.3d). This process was repeated, alternating which sections were chosen (i.e., if the top right and bottom left were taken first, then the top left and bottom right were taken the second time) until the bulk sample was significantly reduced. Then, wet sieving was done to the phosphogypsum in the same

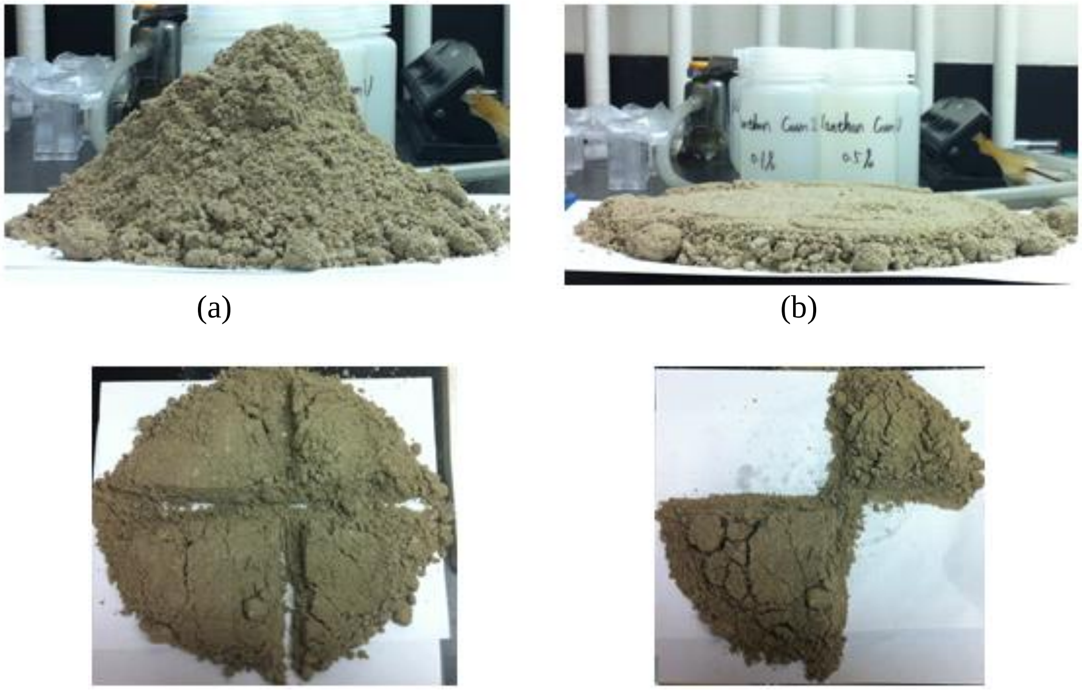

(a) (b)

(c) (d)

Figure 3.3. Coning and quartering method, with (a) cone pile, (b) pressed flat, (c) quartered, and (d) choosing two sections.

way as the previous two samples. The samples after size separation by wet and dry sieving can be seen in Figures 3.4, 3.5, and 3.6.

Once each sample was divided by size, an accurate sample for each size class of each sample was needed for dual energy radiography. To do this, a vibrating riffler was utilized (Figure 3.7). The vibrating riffler separates each size fraction of each sample into eight equal groups by vibrating the pouring dispenser and rotating the eight sample collectors. Three of these groups were chosen at random to be used in Step 3 of the project.

(a) (b) (c)

Figure 3.4. Shaking table concentrate after size separation where (a) >106 μm, (b) 75–106 μm, and (c) 53–75 μm.

(a) (b) (c)

Figure 3.5. Acid plant feed after size separation where (a) >106 μm, (b) 75–106 μm, and (c) 53–75 μm.

(a) (b) (c)

Figure 3.6. Phosphogypsum after size separation where (a) >106 μm, (b) 75–106 μm, and (c) 53–75 μm.

(a) (b)

Figure 3.7. Vibrating riffler, showing both (a) side view and (b) top view.

3.2 Step 2: Calibration

The next step in the project was calibration for HRXMT and calculation of the DE radiography coefficients. This involves several steps in itself. In order to get an accurate calibration, the approximate chemical makeup of the samples needed to be known. Therefore, a mineralogical analysis by XRD was performed and a 3D reconstruction completed using HRXMT.

To do this, part of the largest size group of the shaking table concentrate sample was further separated. One portion of the eight groups of the vibrating riffler was taken and, using gravity separation by hand panning, the heavy particles were separated out from the lighter particles. The heavier particles were more likely to contain RE particles, and so this portion was used to complete the XRD and HRXMT. Half were scanned using HRXMT and half were taken for XRD analysis.

3.2.1 Heavy Particle XRD Analysis

In order to get the mineralogical analysis by XRD, the heavy density sample was ground to a fine powder using agate mortar and pestle. Then, the fine powder was placed on a glass slide and a drop of water was added. The sample was mixed and spread over the surface of half of the slide. The sample became dry after half an hour. Then, the glass slide with powder was covered with another glass slide for XRD analysis. The results of XRD analysis are shown in Figure 3.8. As can be seen, the mineralogical analysis indicates the presence of monazite, zircon, and apatite.

3.2.2 HRXMT Calibration

The HRXMT calibration involves figuring out what conditions to set for the scans and then what standards to use for reconstruction and scaling. The first step is to estimate the attenuation coefficient before the HRXMT scan has been taken. The mass attenuation coefficient has a linear relationship with energy according to Beer’s law. So scans for heavy materials with high density and high atomic number require a high–level X–ray energy source to get enough X–ray photons to the detector. Therefore, it is very important to determine which level of X–ray energy is sufficient to pass through high atomic number and high–density rare earth samples. The preview of the linear relationship of x–ray mass attenuation coefficient and energy, done using XMuDat software, is shown in Figure 3.9. From the estimation of mineral attenuation coefficients, it is evident that the lower the photon energy, the greater the attenuation coefficient difference between minerals. In addition, the photon energy should be large enough to pass through the high atomic number and high density minerals known to be present in the sample (monazite and zircon). Taking both of those factors into consideration, an energy voltage 70 kV was

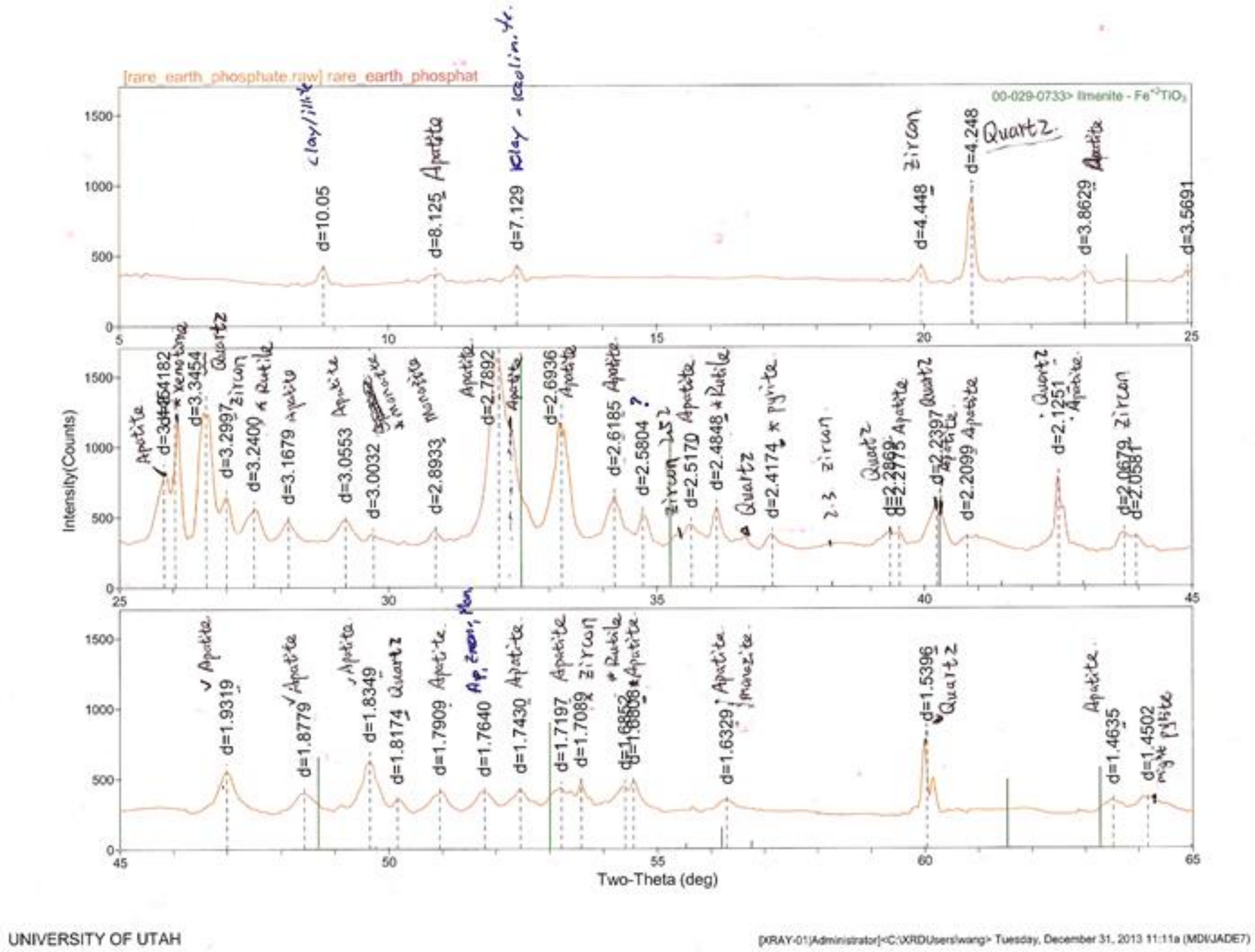

Figure 3.8. XRD analysis of heavy particles from shaking table concentrate.

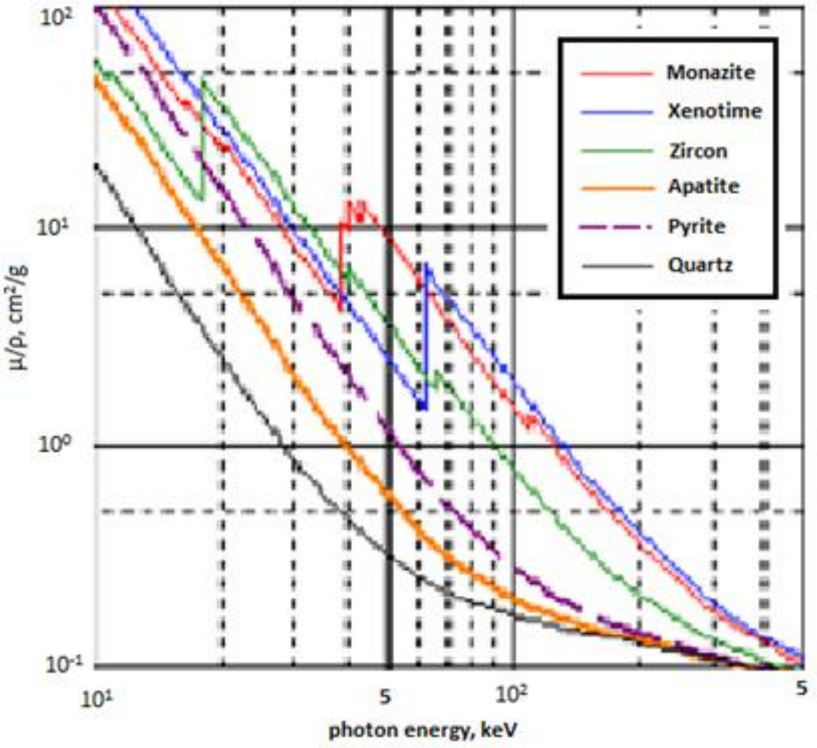

Figure 3.9. Mineral attenuation coefficients versus energy produced using XMuDat.

selected to scan the samples. Other parameters are defined by considering the projection quality and include exposure time 10 seconds and magnification level 4X.

In order to obtain an accurate analysis of the RE sample, the CT standard has to be set for the appropriate mineral characterization. In this instance, from the initial XRD analysis, it is expected to contain monazite, zircon, apatite, and quartz minerals in the samples. As the only RE mineral, monazite is the mineral of interest. Therefore, monazite and zircon standards were scanned using the same conditions as the rare earth sample, which are 4X magnification level, 70 kV energy voltage, and 10 seconds exposure time. After the reconstruction of CT standards, the scaled CT number distribution map can be exported and transformed into extension .txt file, which can then be plotted using EXCEL or XMGrace. The scaled CT number distribution map of minerals is shown in Figure

3.10. From the scaled CT number distribution map of CT standards, it can be seen that monazite has the highest attenuation coefficient and apatite has the lowest. There is a large difference between the high density and high atomic number minerals and the gangue mineral apatite. The minerals are clearly distinguished based on their attenuation coefficient. However, there is some overlap between monazite and zircon, but this is not a serious problem as the overlap is minor.

3.2.3 Heavy Particle HRXMT Scans

The preparation for the HRXMT scans was much simpler than for XRD analysis. The half portion was placed in a 5 mm syringe and secured using its own plunger and

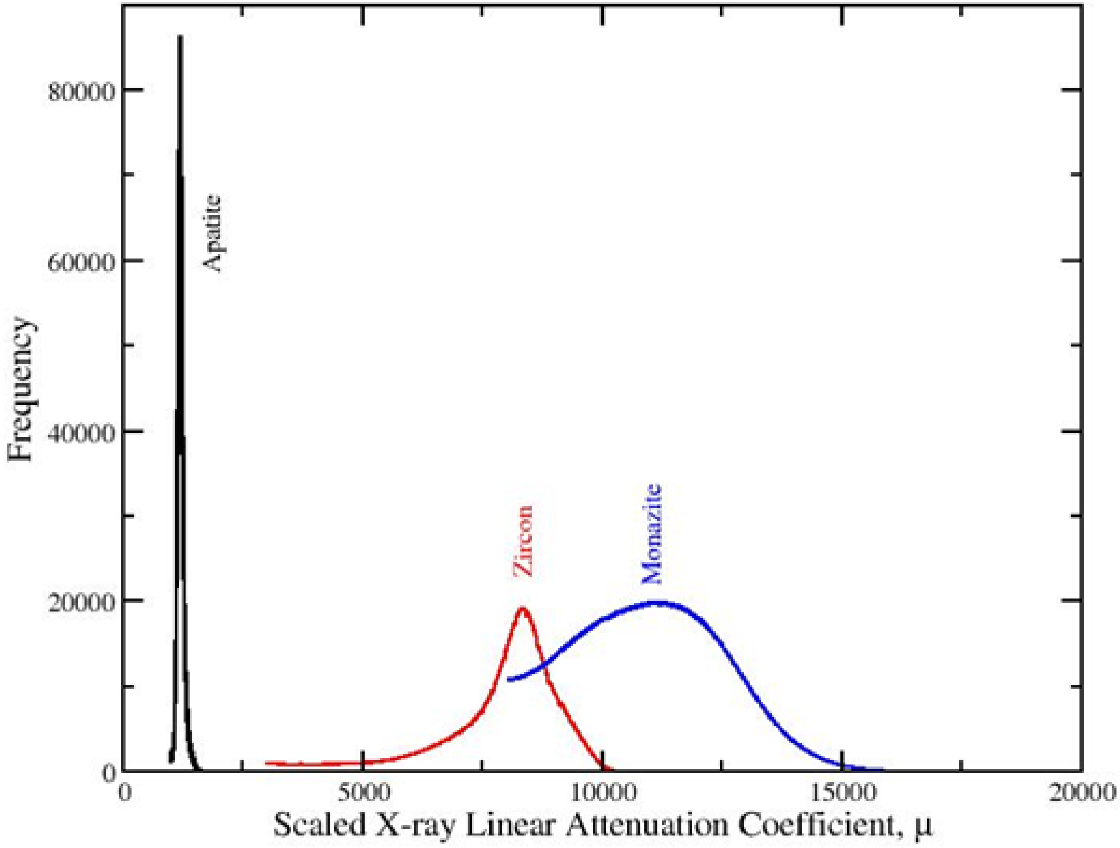

Figure 3.10. Scaled CT number distribution of minerals, scaled using rare earth standard.

mounted on a toothpick. The sample was scanned using 4X magnification level, 70 kV energy voltage, and 10 seconds exposure time. The backprojection was then reconstructed and scaled using the CT standards of pure monazite, zircon, and apatite samples to obtain the attenuation coefficients of each voxel in the sample. The resulting 3D images are shown in Figure 3.11.

3.2.4 DE Radiography Coefficients

Therefore, because it is known that the samples contain apatite, zircon, and monazite, aluminum, copper, and lead can be used as the reference samples to calculate the DE radiography coefficients. These can be used as the reference samples because they approximately coincide with the three mineral phases usually present in a sample from metal mining operations (gangue, base metal minerals, and precious metals) as well as the three minerals known to be contained in the samples. Gangue minerals will have a low attenuation coefficient, base metal minerals will have a medium attenuation coefficient, and precious metals will have a high attenuation coefficient.

Using the aluminum, copper, and lead reference samples, the DE radiography coefficients were calculated to be $k_1 = -8.97\text{x}10^{11}$, $k_2 = 7.95\text{x}10^{11}$, $k_3 = 1.88\text{x}10^{6}$, and $k_4 = -1.16\text{x}10^{6}$ using equation 8 found in section 2.2.3 above and $p = 3.8$ to account for the different absorption mechanisms (Naydenov et al., 2003; Lin et al., 2013). These coefficients produce the curve shown in Figure 3.12. Figure 3.12 also shows how close the estimated effective atomic number was to its actual effective atomic number.

From this, all the information for relating the relative reflex to the effective atomic number as well as the conditions to use for HRXMT scans and standards for reconstruction are now known and the rest of the steps completed without issue.

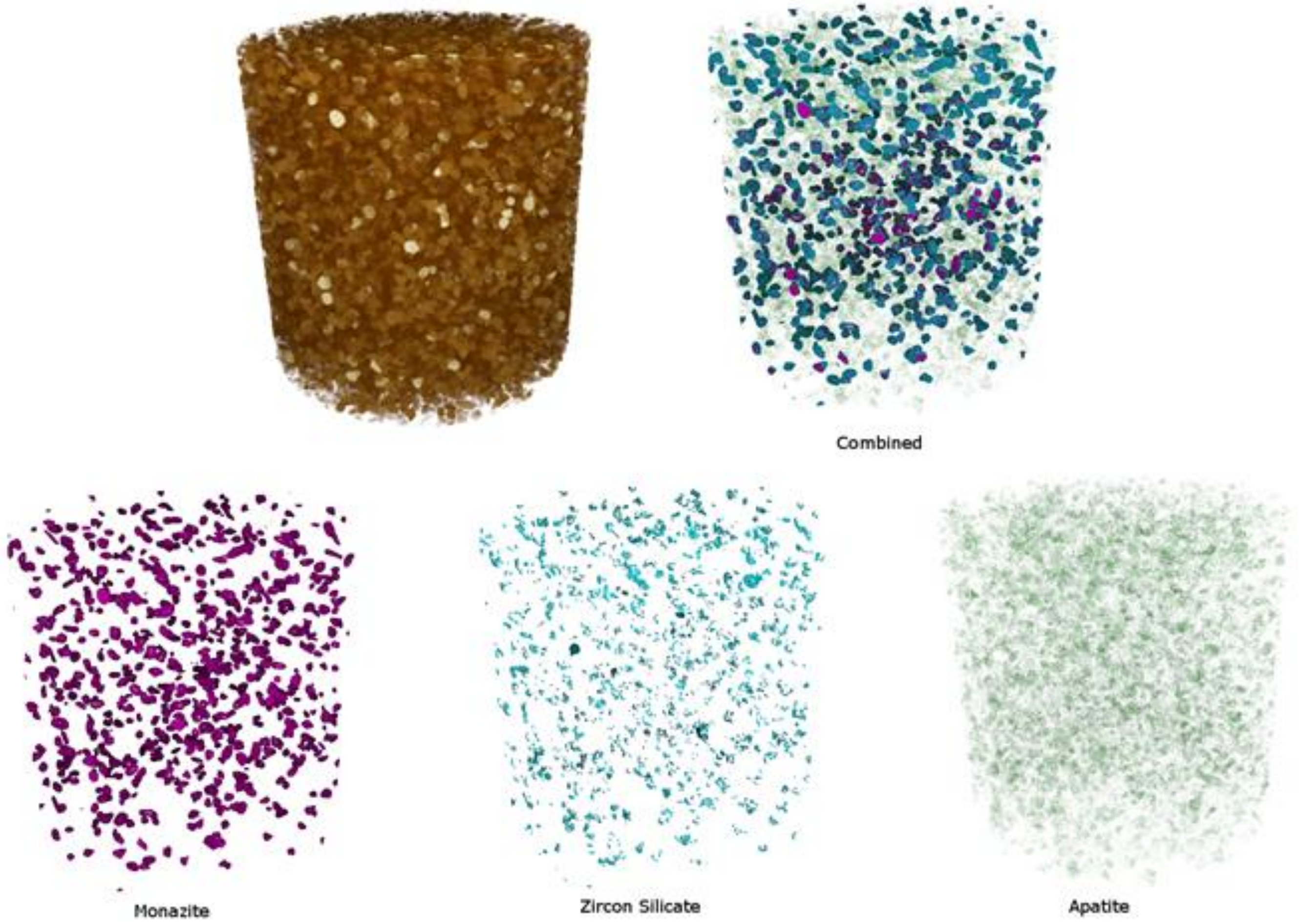

Figure 3.11. Reconstructed 3D rendered images from HRXMT scans of the heavy particles of shaking table concentrate containing monazite, zircon, apatite, etc. (voxel resolution= 4.59x4.59x4.59 µm). Reconstruction viewed by Drishti.

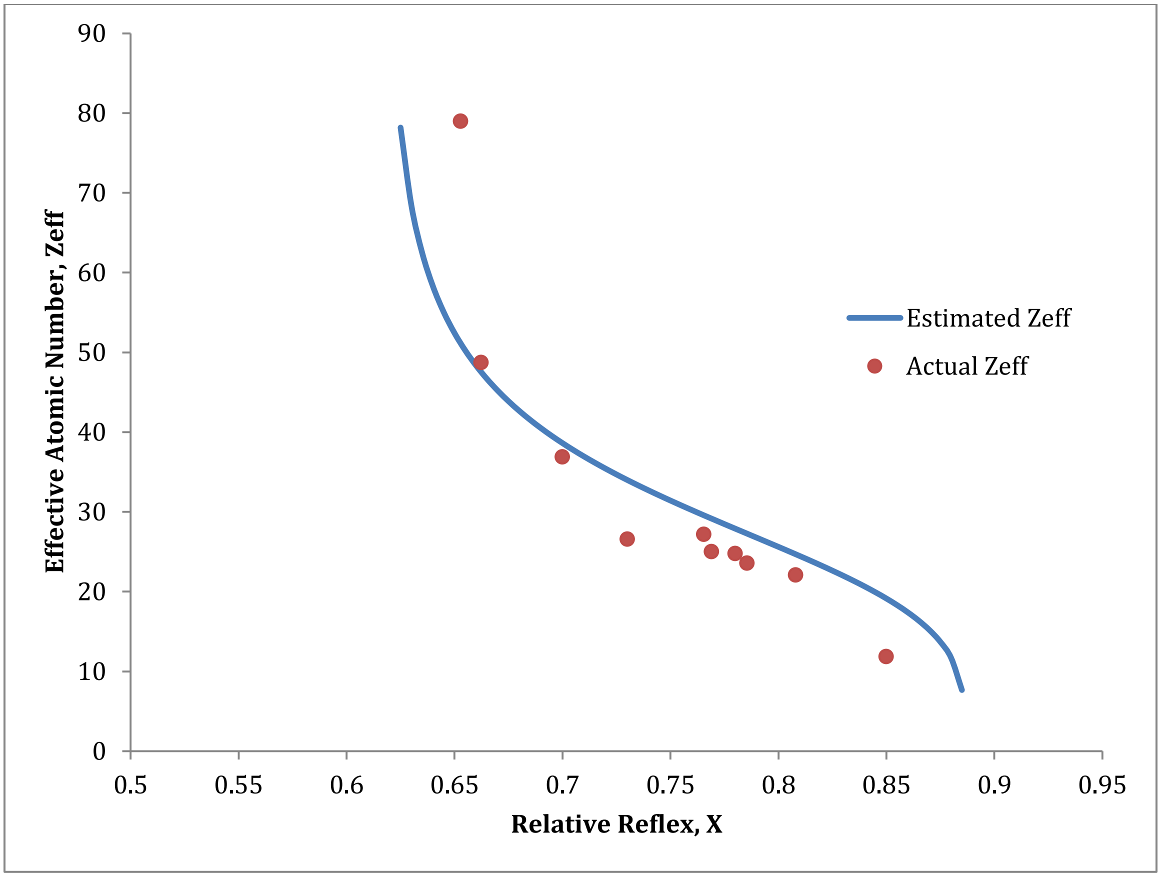

Figure 3.12. Calibration curve for given k and p values and comparison between predicted and actual effective atomic numbers.

3.3 Step 3: DE Slide Preparation

The next step was to prepare the slides for DE radiography. One of the eight subgroups created by the vibrating riffler in Step 1 was chosen at random and used for each slide. 3/4" double sided sticky tape was attached to a 3"x1" glass slide. To make sure each slide could be scanned the same and to ensure correct particle identification in future steps, a plastic mold, shown in Figure 3.13, was then attached to the double sided sticky tape. The contents of the chosen group were spread inside the plastic mold and then the mold removed. A second slide was then taped on top, creating a sandwich with the sample particles to be scanned on the inside of two glass slides. A few of the DE

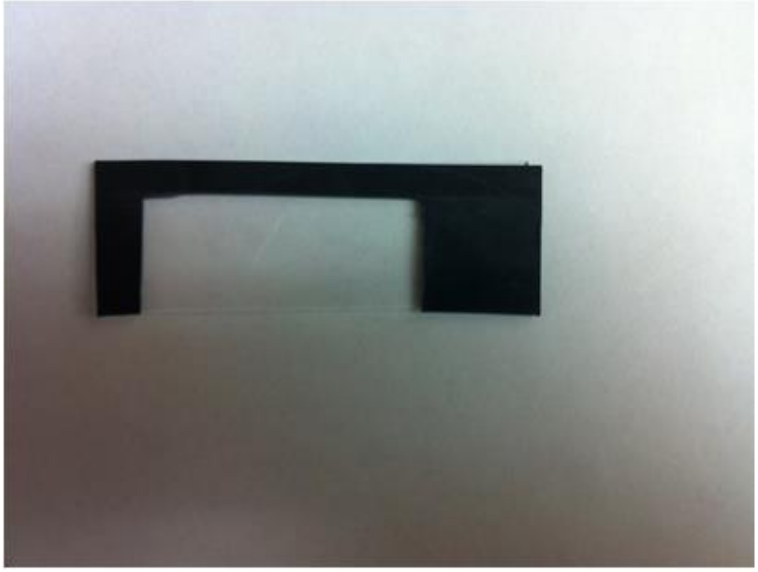

Figure 3.13. Plastic mold used to shape sample particles on slide to ensure uniformity.

slides can be seen in Figure 3.14. Three slides were made for each size class of each sample, except for those <53 microns. It was decided that these particles would be too small for DE radiography using 4X magnification and so were excluded. This gave a total of nine slides for each sample and a total of 27 slides for the whole project. Each slide contains roughly 34,000 particles, so a total of 102,000 particles from each slide class for each sample were imaged and 306,000 total particles from each sample stream.

3.4 Step 4: DE Scans

The DE radiography scans were completed by splitting the slide into 40 sections, making a 4x10 grid, and scanning each section at a low energy level (80 kV) and a high energy level (140 kV). They were scanned using the averaging mode on the Xradia MicroXCT–400 machine, taking three images at 10 seconds each to average together and produce a single image. The sample was set at a distance of 44 mm from the source and 20 mm from the detector. As each sample was prepared carefully with the mold, locating

Figure 3.14. Three examples of DE radiography slides.

each of the 40 sections was a simple matter of using the continuous mode to make sure the edge of the sample aligned with the edge of the scan when set at the predetermined position of sample x = -250 µm and sample y = -6600 µm. From this position, the sample was shifted approximately 4700 microns on either the x-axis or y-axis to complete each successive scan. Figure 3.15 shows the tool used to control the position of the sample. In addition, a reference image was taken at both low and high energies for every slide so that a correct reference could be applied for every slide. As stated in section 2.2.2, the reference image normalizes the attenuation coefficients into a percentage of the transmission. This essentially makes the difference between attenuation coefficients larger, increasing the contrast in the image. This can be seen in Figure 3.16 in a side by side comparison of a scan where a reference is not applied and where it is.

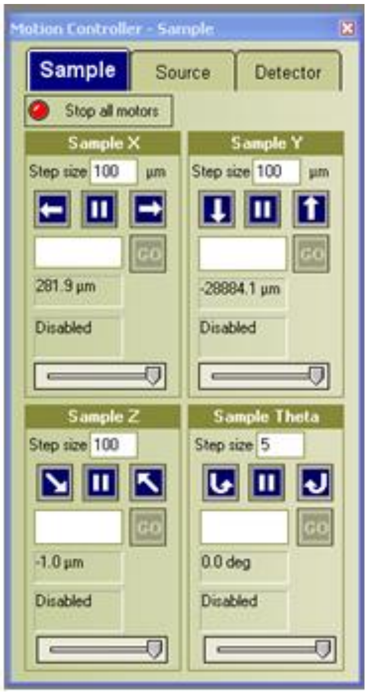

Sample X
Step size 100 µm
281.9 µm
Disabled

Sample Y
Step size 100 µm
-28884.1 µm
Disabled

Sample Z
Step size 100
-1.0 µm
Disabled

Sample Theta
Step size 5
0.0 deg
Disabled

Figure 3.15. Tool used to move the sample a set amount of microns in either the x or y direction for each DE scan.

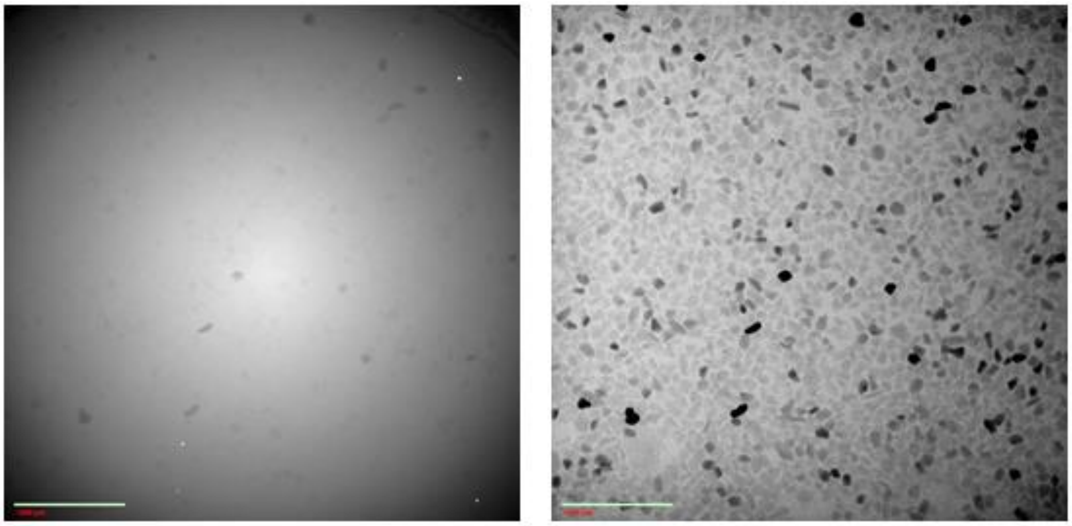

Figure 3.16. Image on left is radiography scan before reference is applied and image on right is after reference has been applied.

Mathematically, the reference image is the $I_{0,i}$ in the DE calculations, used to find the attenuation coefficient, relative reflex, and, from there, the effective atomic number. Several examples of the resulting scans are shown in Figures 3.17, 3.18, and 3.19. The light blue line at the bottom of each scan indicates a scale of 1,000 microns. Note the darker particles in each radiography scan. These are potential RE minerals.

3.5 Step 5: DE Analysis

After the DE scans were completed, Matlab was used for analysis and calculations. The scans were imported into the program then analyzed pixel by pixel. First, the reflex, described in section 2.2.3, was calculated using the individual energy scans and the reference images. Then, the relative reflex, X, was found by dividing the reflexes from the low and high energy scans. Some of the resulting relative reflex radiographs can be seen in Figures 3.20, 3.21, and 3.22, which correspond to the same sections and slides shown in Figures 3.17, 3.18, and 3.19. It is important to note on these radiographs that some of them appear darker due to the color scaling automatically applied by Matlab in relation to the attenuation coefficients. The images that appear darker have lower overall attenuation coefficients and so appear as a darker image, even though other sections may have more potential RE particles.

Once the relative reflex had been calculated, a threshold was then applied to identify potential RE particles. Thresholding discards all the relative reflex values above a given point and accepts those below it, highlighting which particles may be of interest. The threshold number used was $X = 0.70$, which corresponds to $Z_{eff} = 38$. This means that all of the values where $X < 0.70$ were accepted, giving particles with $Z_{eff} > 38$. This threshold was chosen based on the calibration curve, and tested on a sample of pure

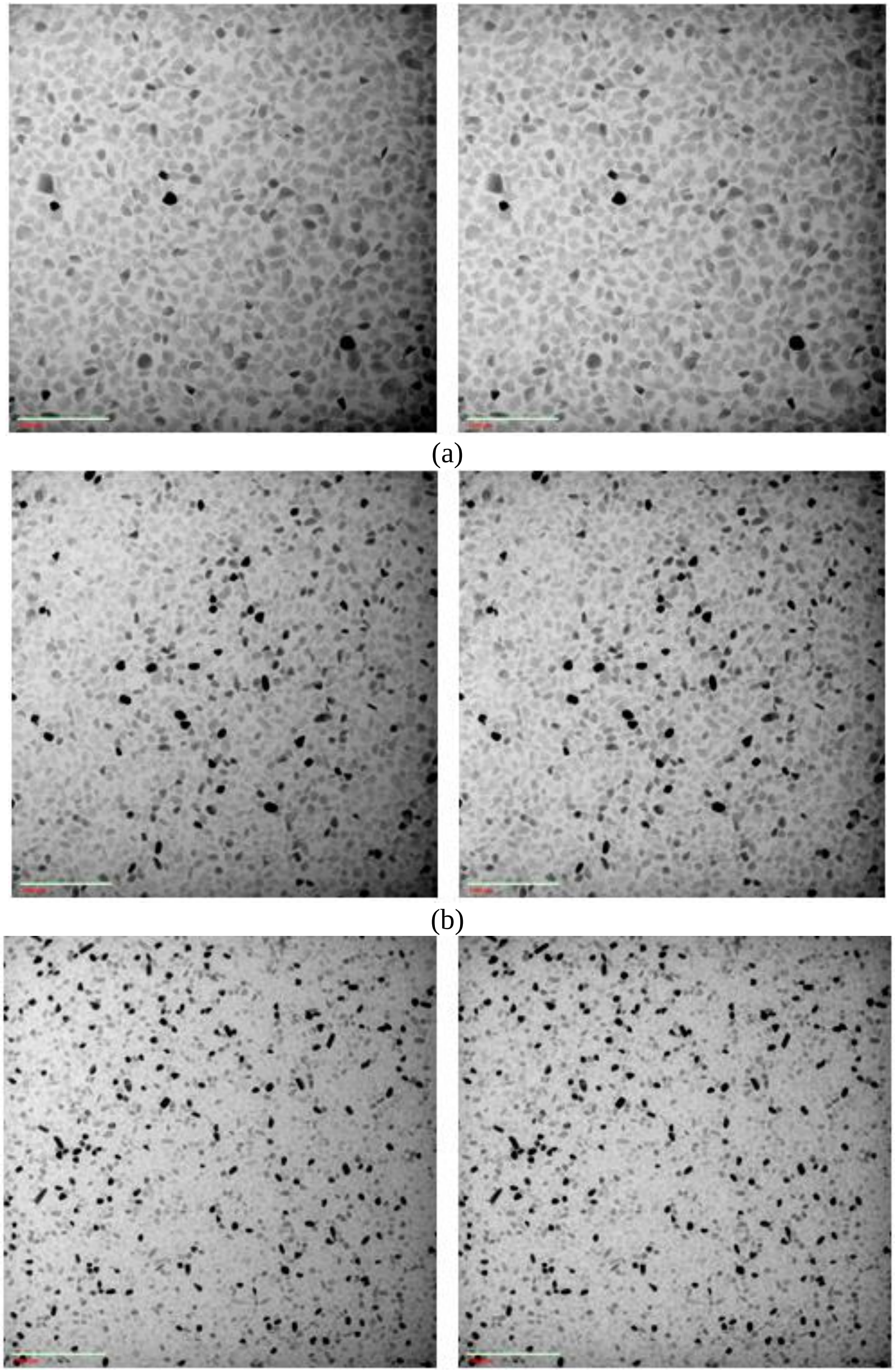

(a)

(b)

(c)

Figure 3.17. DE radiography scans from shaking table concentrate size fractions (a) >106 μm, (b) 75–106 μm, and (c) 53–75 μm. The images on the left are of low energy (80 kV), and the images on the right are of high energy (140 kV).

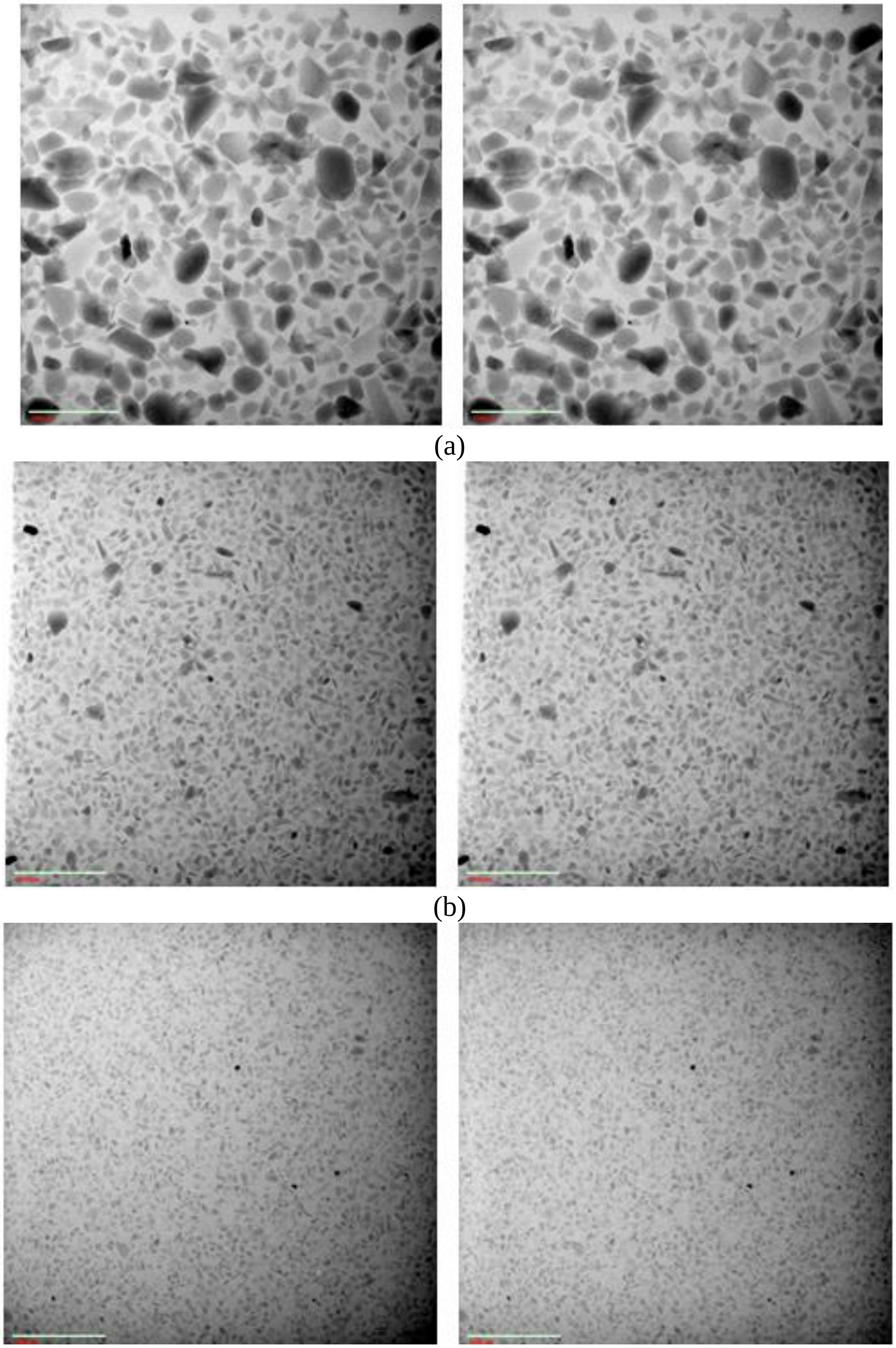

(a)

(b)

(c)

Figure 3.18. DE radiography scans from acid plant feed size fractions (a) >106 µm, (b) 75–106 µm, and (c) 53–75 µm. The images on the left are of low energy (80 kV), and the images on the right are of high energy (140 kV).

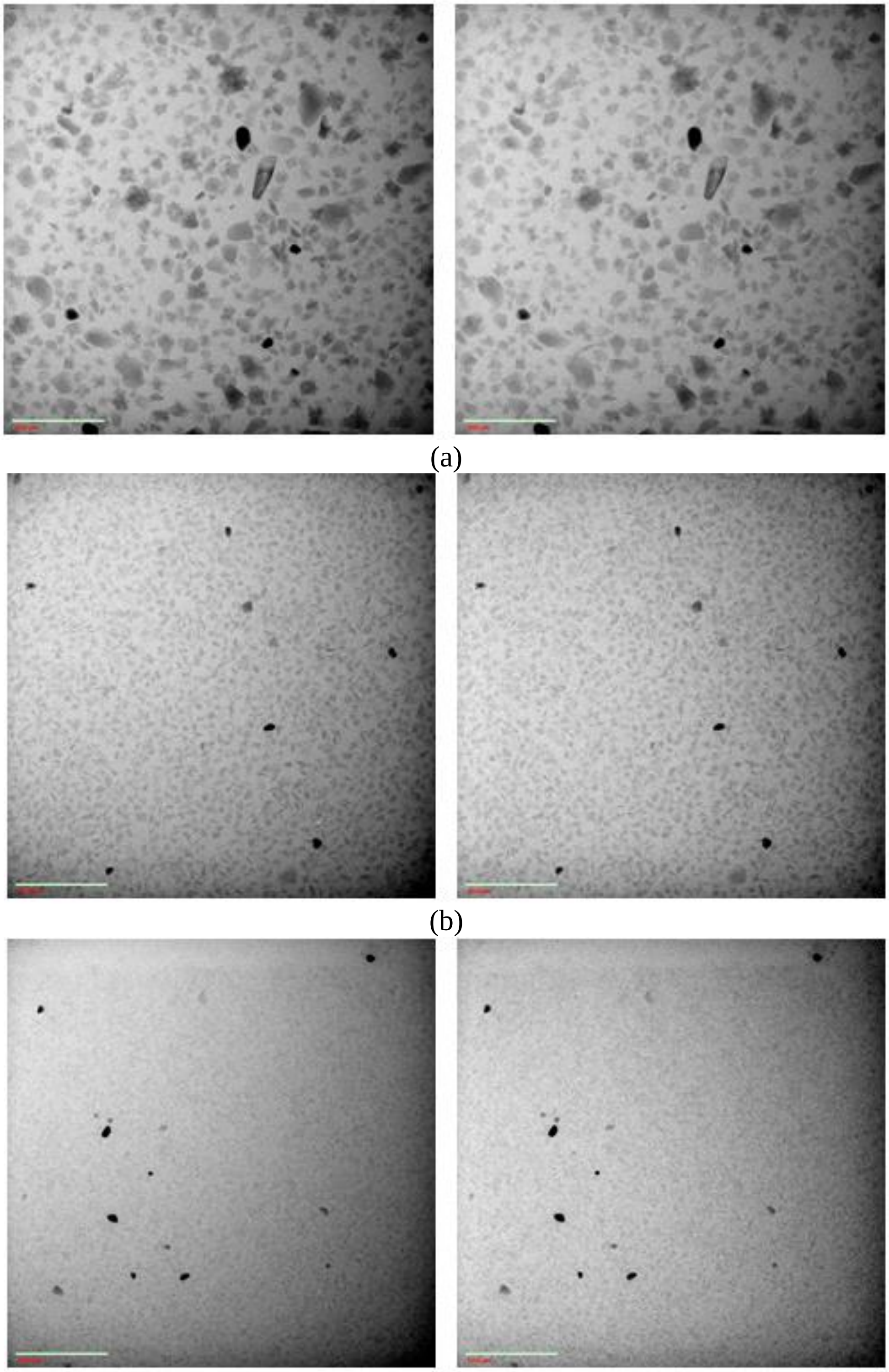

(a)

(b)

(c)

Figure 3.19. DE radiography scans from phosphogypsum size fractions (a) >106 μm, (b) 75–106 μm, and (c) 53–75 μm. The images on the left are of low energy (80 kV), and the images on the right are of high energy (140 kV).

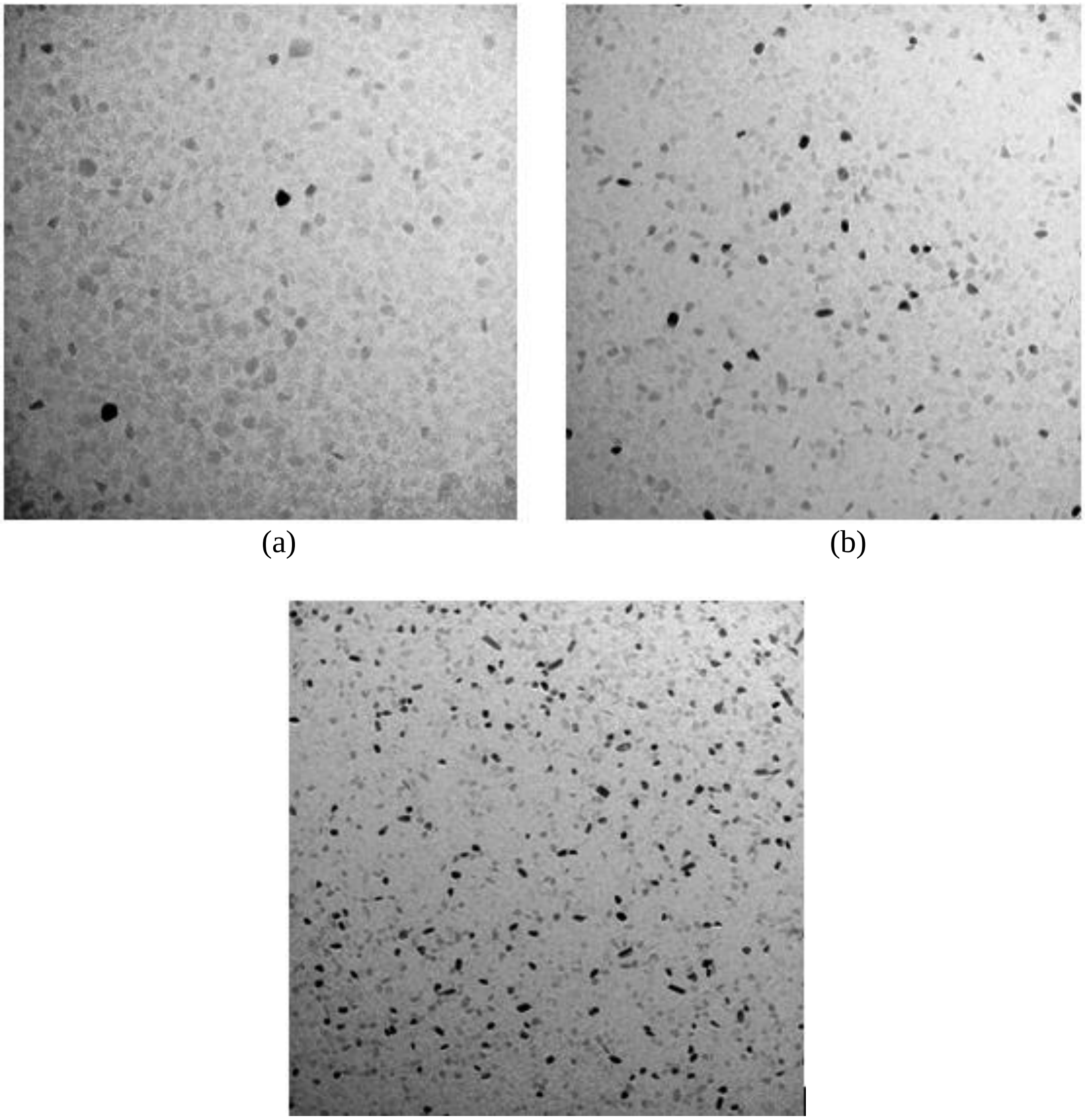

(a) (b)

(c)

Figure 3.20. Radiographs of the relative reflex calculated using Matlab for the shaking table concentrate with size fraction (a) >106 μm, (b) 75–106 μm, and (c) 53–75 μm.

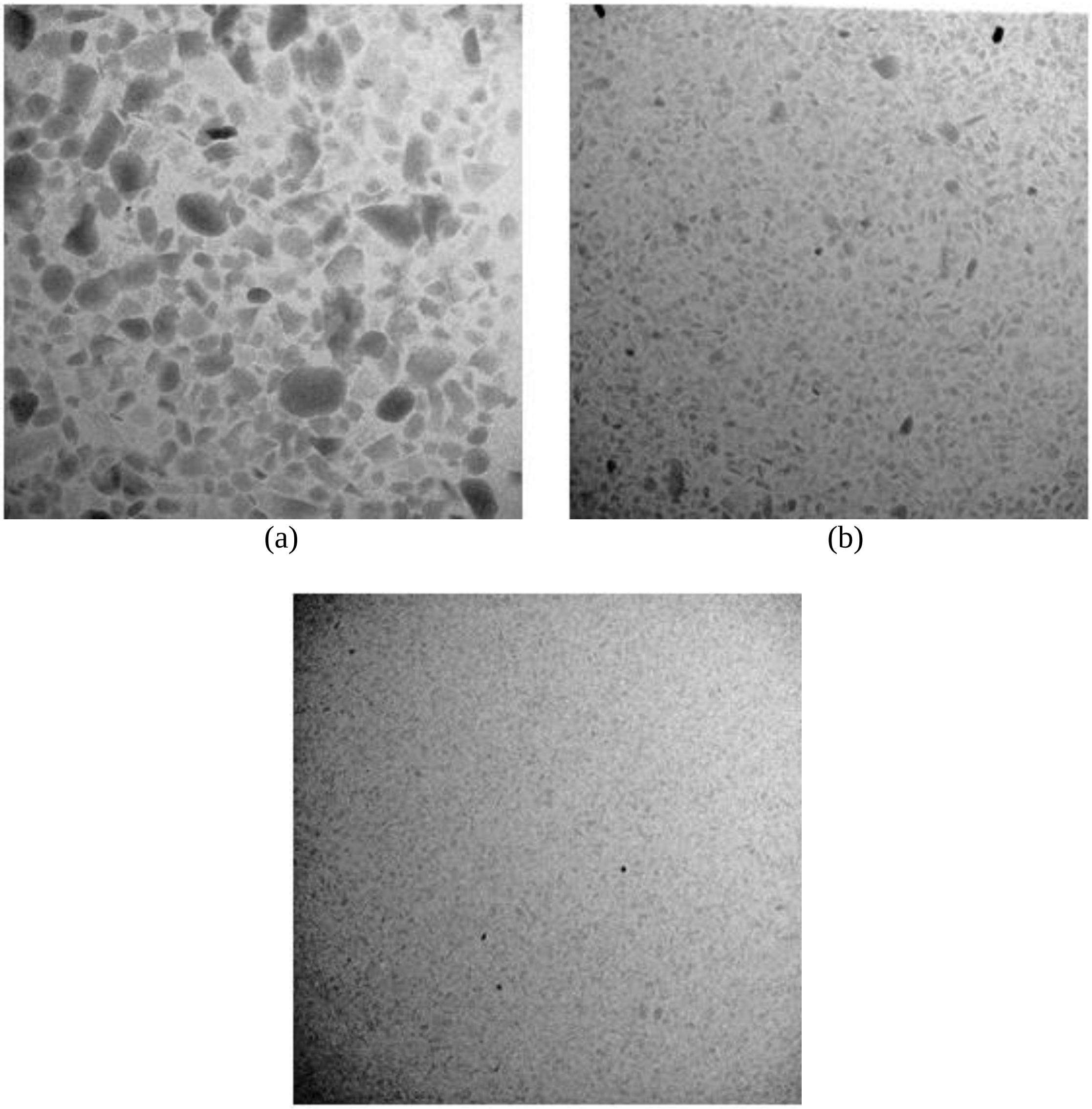

(a)

(b)

(c)

Figure 3.21. Radiographs of the relative reflex calculated using Matlab for the acid plant feed with size fraction (a) >106 μm, (b) 75–106 μm, and (c) 53–75 μm.

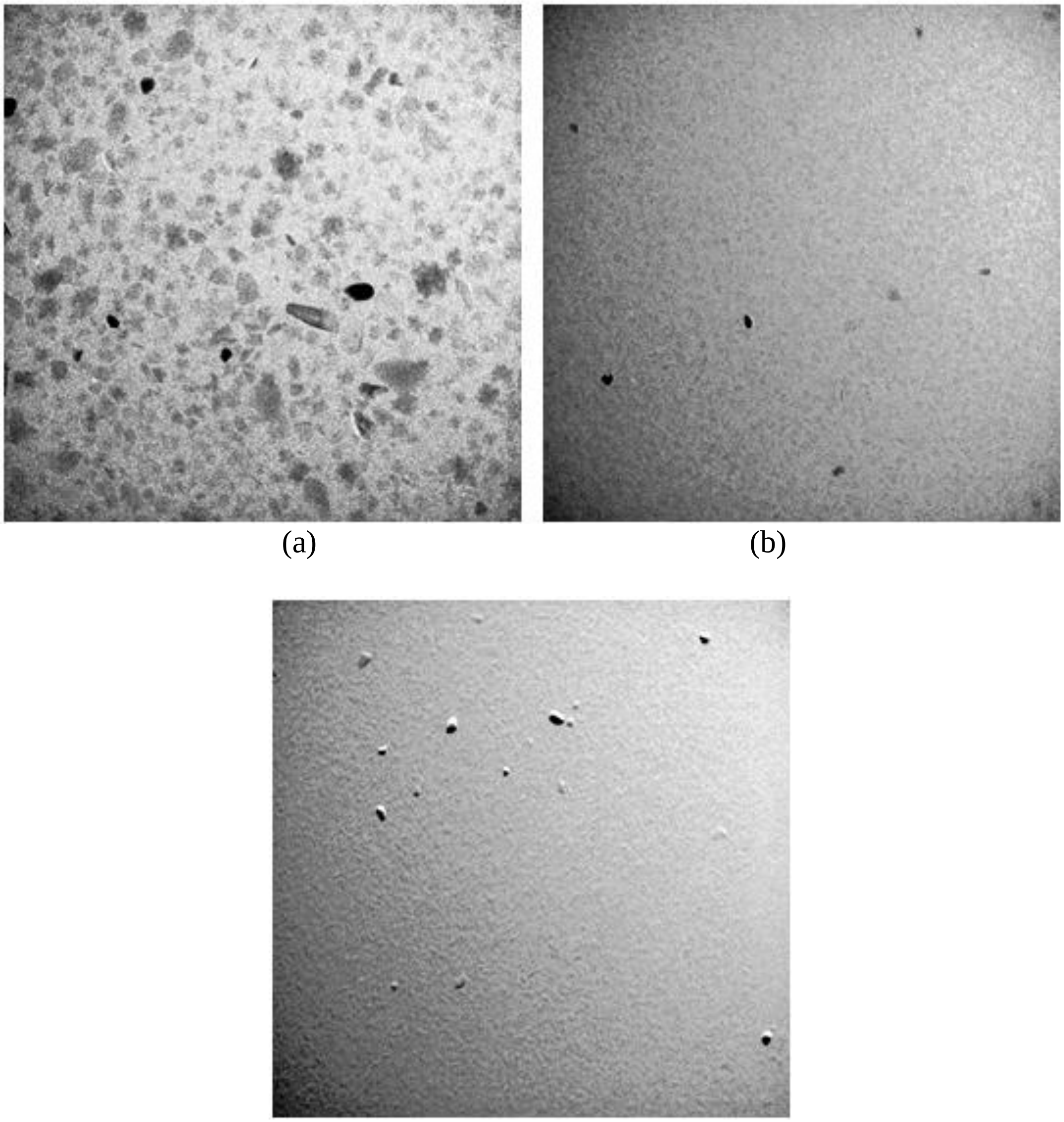

(a) (b)

(c)

Figure 3.22. Radiographs of the relative reflex calculated using Matlab for the phosphogypsum with size fraction (a) >106 μm, (b) 75–106 μm, and (c) 53–75 μm.

bastnaesite, seen in Figure 3.23, which has a similar effective atomic number as monazite.

There was some difficulty in determining which threshold value to use. Initially this difficulty had to do with the Matlab code being written incorrectly, and so no particles were being shown as potential RE particles. Once the code had been fixed, a threshold value of X = 0.64 was tried, which corresponds to $Z_{eff} \approx 62$. However, this also resulted in completely black images. It was then recommended to test a pure sample of bastnaesite to see if there simply were not any RE particles on the slides or if the code or thresholding were wrong instead. After scanning and running the radiographs through Matlab, it was discovered that the error was in the threshold value. After testing several values, X = 0.70 was chosen as the appropriate threshold value.

When reexamining the calibration curve, 0.70 might seem a little high and Z_{eff} = 38 a little low when looking for RE particles. However, as the particle density increases,

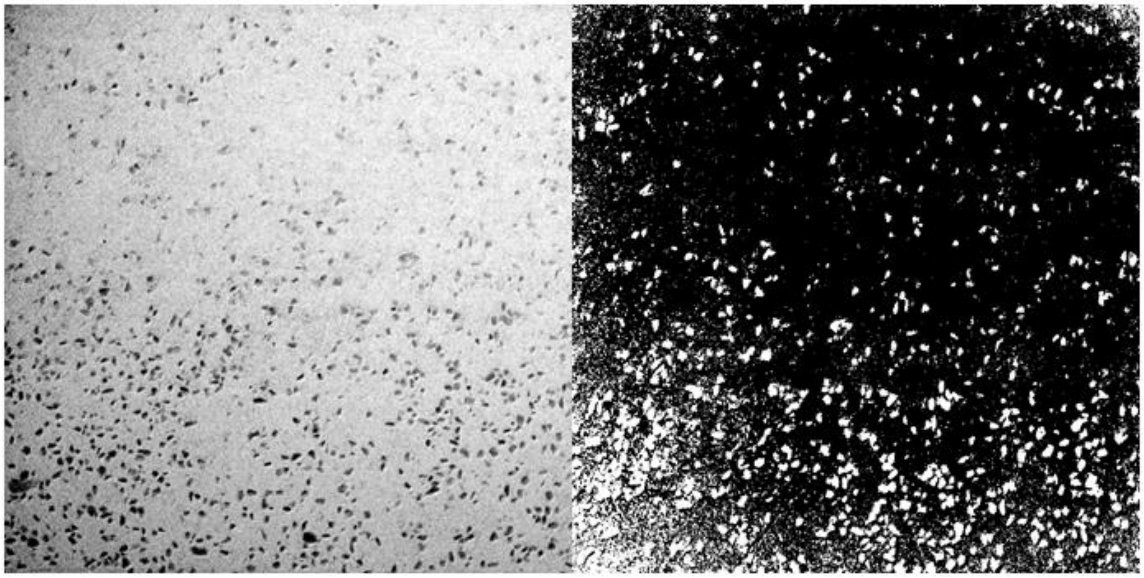
(a) (b)

Figure 3.23. Bastnaesite (a) radiograph and (b) resulting thresholded image used for threshold verification.

the 80 kV and 140 kV energies may have some difficulties penetrating the particles. Due to this effect, as it was discovered, the accuracy of the calibration curve as it nears higher atomic numbers decreases. This is why it was ultimately discovered that 0.70 needed to be used to make sure all the potential RE particles were gathered.

The corresponding thresholded images from the radiographs shown above can be seen in Figures 3.24, 3.25, and 3.26. Note that the white portions in the Figures correspond with potential RE particles. While some of these thresholded images appear to have a good number of potential rare earth particles, it is important to remember that each image is only one of 120 possible images for each size group of each sample, and the majority of the other images have no potential particles shown.

3.6 Step 6: HRXMT Sample Preparation

Using the thresholded images as a guide, the HRXMT samples were then prepared. For this particular sample type, meaning both the particle size and the amount to be scanned, a 5 mm syringe was secured to a toothpick using hot glue. The sample was set between two plungers cut to size. Because the plungers fit the syringe perfectly, the sample was prevented from moving during scanning.

The initial idea was to use very sharp tweezers to pull the individual particles off the DE slides. However, after several attempts with multiple pairs of tweezers, it was nearly impossible to locate and remove the particle of interest by itself. Therefore, it was determined to take the entire sections wherever a potential RE particle appeared. An additional slide with the 4x10 grid etched into it, shown in Figure 3.27, was used as a guide of where each section was located on each sample slide. Even taking whole sections, some difficulties were encountered in removing the particles, especially the

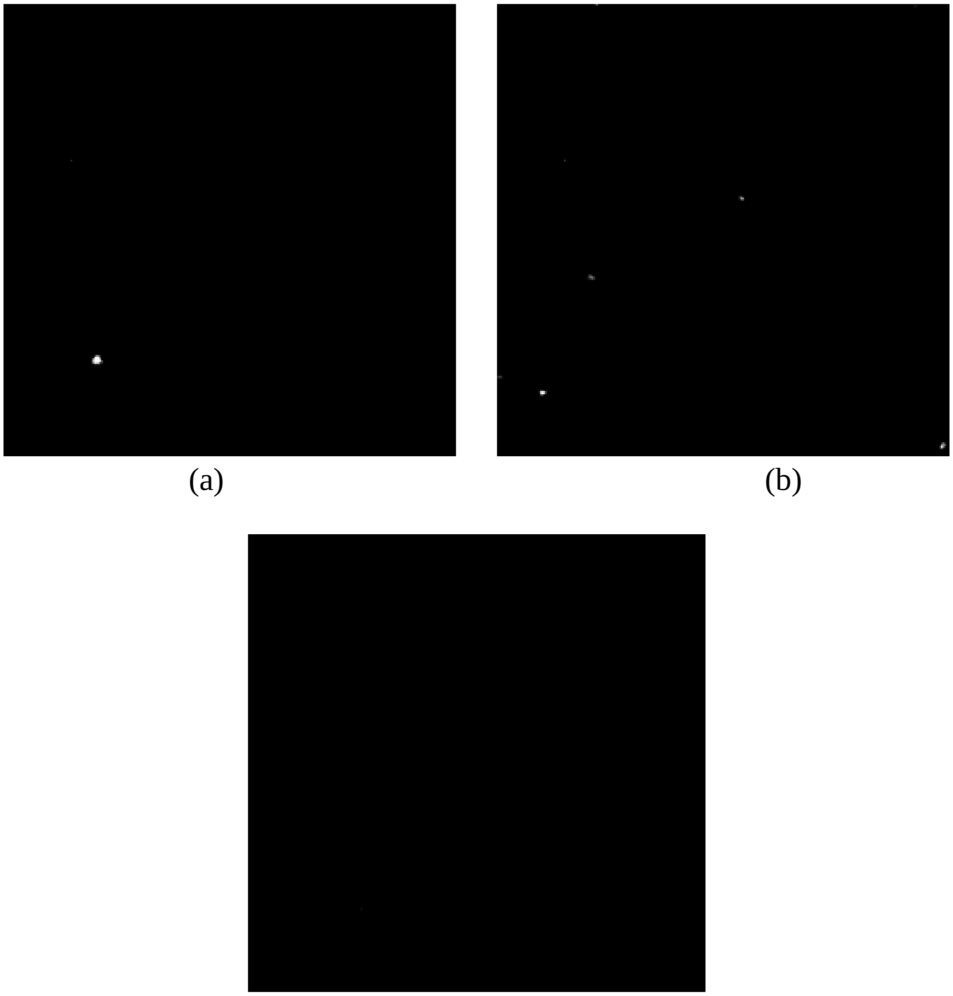

(a)

(b)

(c)

Figure 3.24. Thresholded images identifying potential RE particles of the shaking table concentrate at size fraction (a) >106 μm, (b) 75–106 μm, and (c) 53–75 μm.

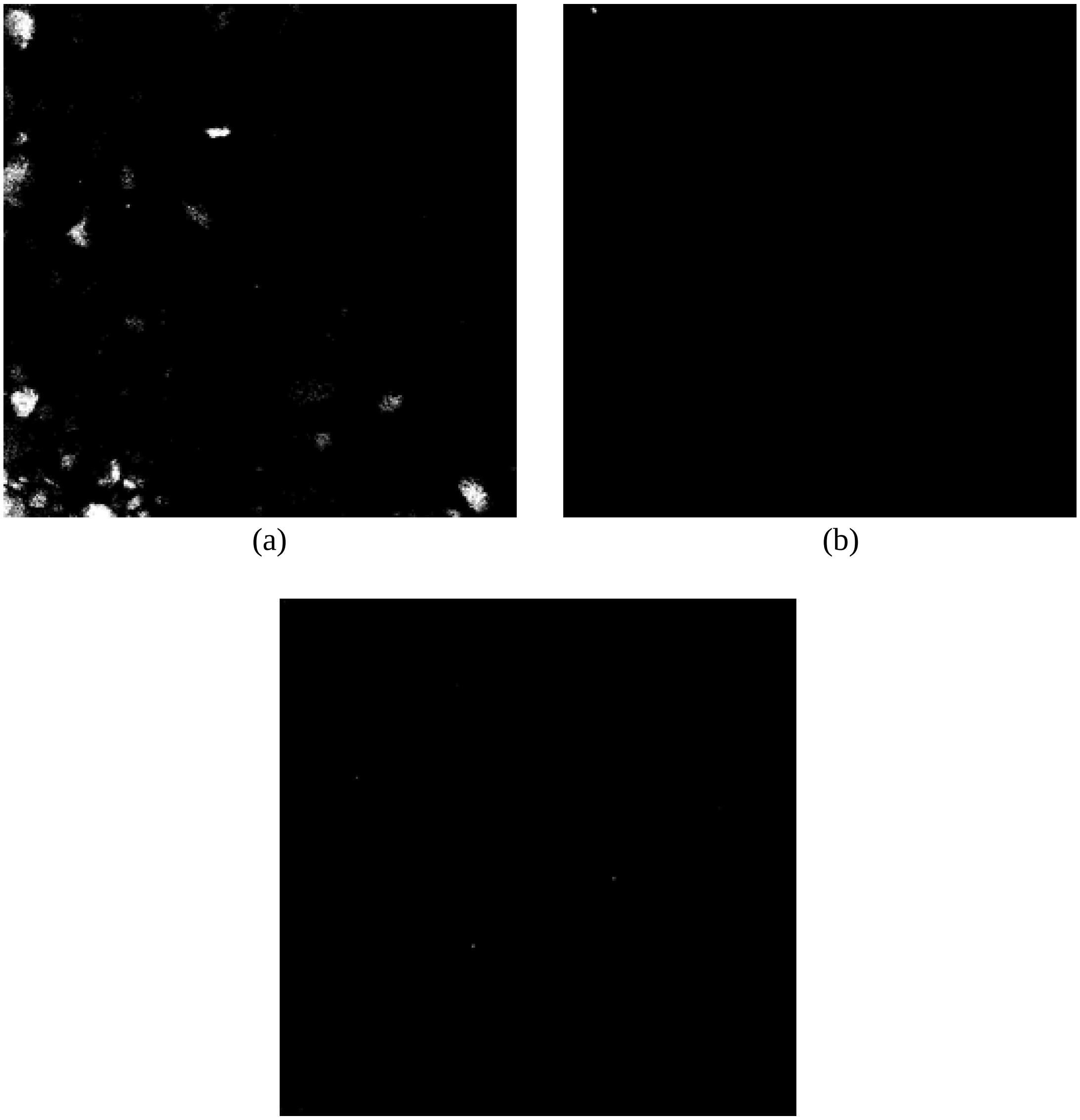

(a) (b)

(c)

Figure 3.25. Thresholded images identifying potential RE particles of acid plant feed at size fraction (a) >106 μm, (b) 75–106 μm, and (c) 53–75 μm.

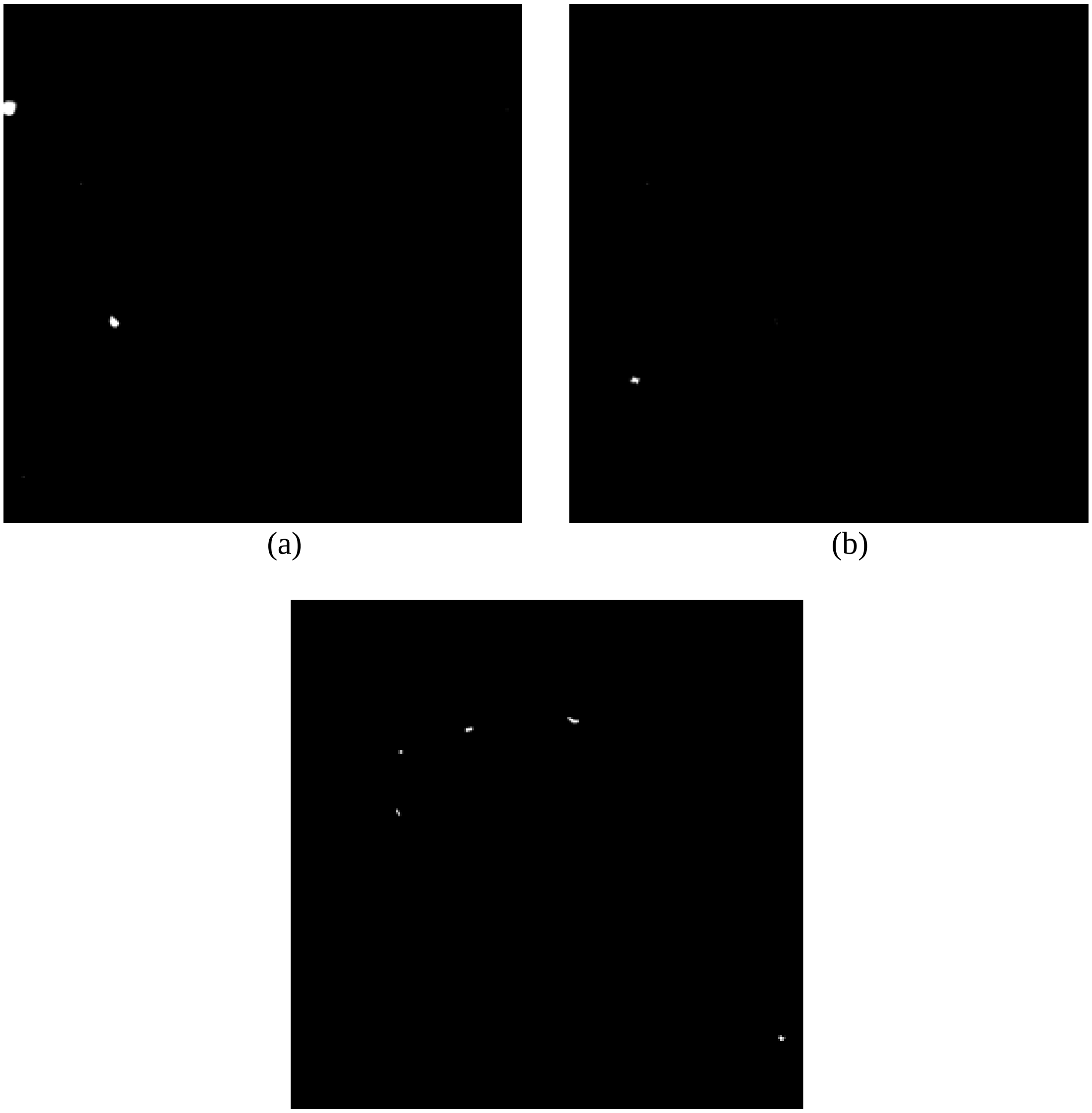

(a)

(b)

(c)

Figure 3.26. Thresholded images identifying potential RE particles of phosphogypsum at size fraction (a) >106 μm, (b) 75–106 μm, and (c) 53–75 μm

Figure 3.27. Slide with 4x10 grid etched onto its surface to aid in section identification with particles of interest.

smaller ones, due to the adhesive on the tape coming off with the particles. After some frustration, it was discovered that this was could be avoided by using less pressure to remove the particles. The sample particles from each slide were separated from each other using a layer of circular paper, as demonstrated with Figure 3.28, for interest in comparing the DE readings to the final HRXMT analysis. In order to maintain the integrity of the bulk sample streams themselves, three HRXMT samples were prepared, one each for the shaking table concentrate, acid plant feed, and phosphogypsum. This prevented any stream from even accidentally mixing and allowed for an accurate RE accounting of each sample stream in the final analysis. The HRXMT samples can be seen in Figure 3.29.

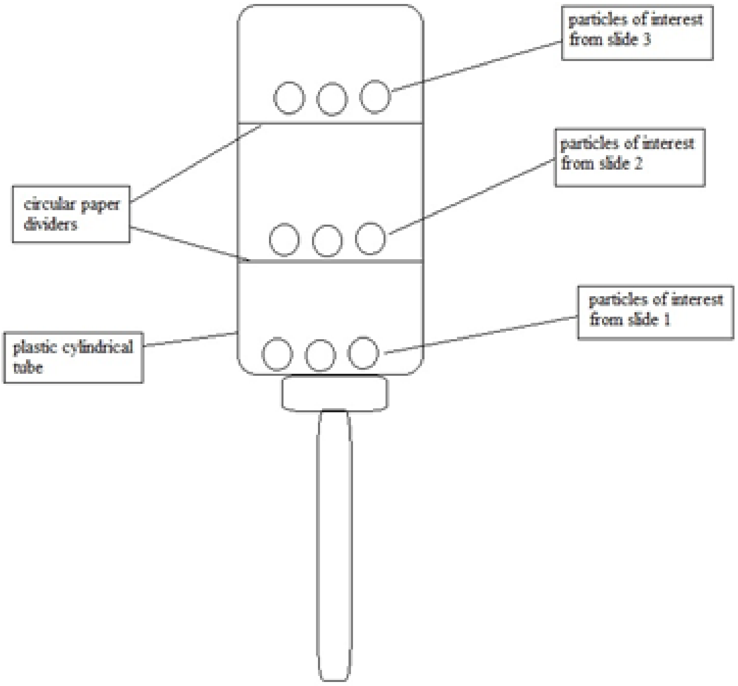

Figure 3.28. Drawn example of HRXMT sample setup, showing the potential RE particles from each slide, separated from each other using circular pieces of paper.

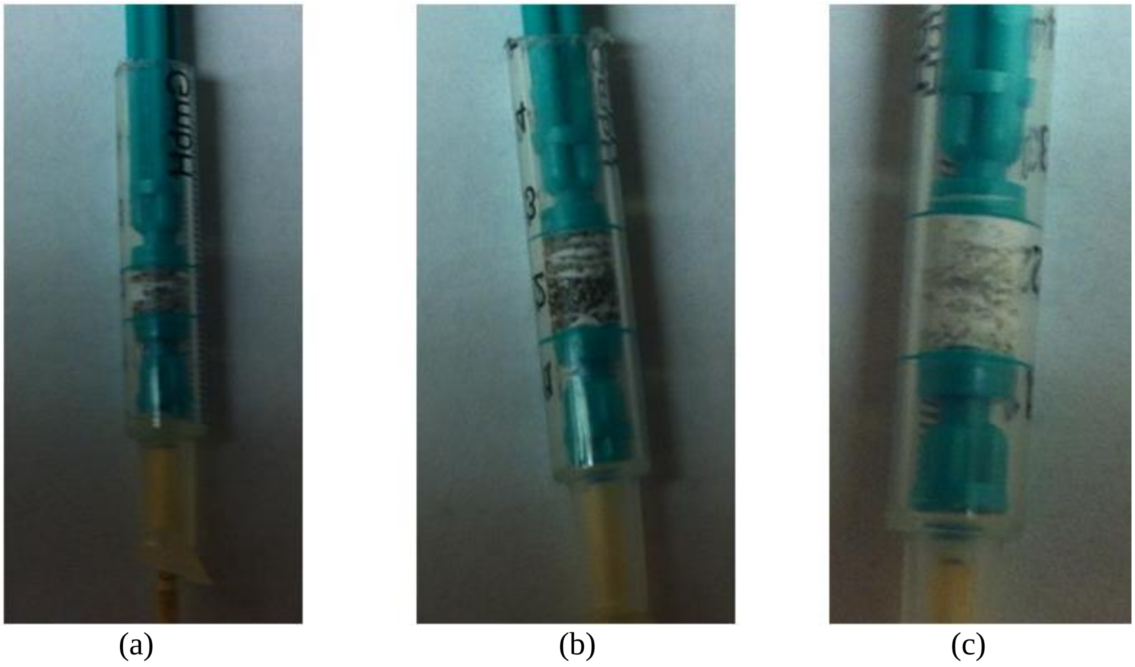
(a) (b) (c)

Figure 3.29. Final HRXMT samples for each (a) shaking table concentrate, (b) acid plant feed, and (c) phosphogypsum.

3.7 Step 7: HRXMT Scans

Completing the actual HRXMT scans was the next step. The scans were completed at the energy level determined in the HRXMT calibration in Step 2 (see section 3.4.2). Using the XMController, the sample was first positioned so that the edges of the sample aligned with the edges of the field of view on the scan, at both 0° and –90°, and the center position saved. From here, the recipe was created. The recipe includes all the possible variables and allows the user to change them as desired. For these particular samples, the values that were chosen are shown in the recipe window in Figure 3.30. The most important of these settings are the start angle (–180°), end angle (180°), number of images (1000), exposure time (10 s), binning (1), source voltage (70 kV), source power (10 W), objective magnification (4X), source–sample distance (-44 mm), detector–sample distance (20 mm), and inserting the saved center position into the tomography locations. Each recipe was saved in case they needed to be referenced in the future and then the recipe was run. Because each projection is taken for 10 seconds and 1000 images are taken in addition to the references, the total time for each HRXMT scan is over 4 hours.

3.8 Step 8: HRXMT Reconstruction

The next to last step was the HRXMT reconstruction described in the background section 2.2.4. To recap, after the projections have been completed, several of which are shown in Figures 3.31, 3.32, and 3.33, the file was opened in XMReconstructor. First, the center shift was established. The values for each of the samples all turned out to be -3. Then the reconstruction was started by entering the file name, the center shift for that particular sample, and the beam hardening and selecting the phosphate rare earth mineral

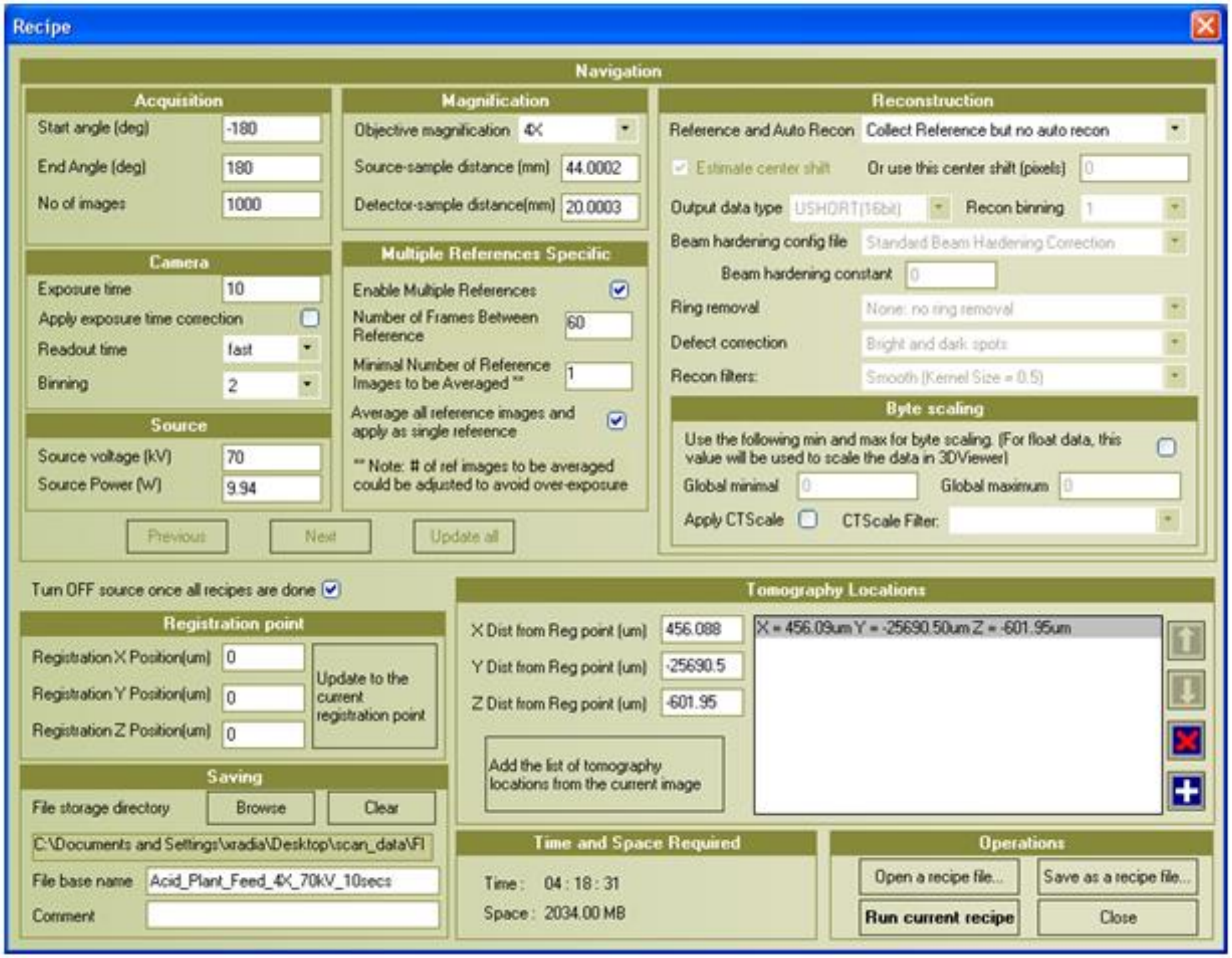

Acquisition
Start angle (deg): -180
End Angle (deg): 180
No of images: 1000

Camera
Exposure time: 10
Apply exposure time correction ☐
Readout time: fast
Binning: 2

Source
Source voltage (kV): 70
Source Power (W): 9.94

Magnification
Objective magnification: 4X
Source-sample distance (mm): 44.0002
Detector-sample distance(mm): 20.0003

Multiple References Specific
Enable Multiple References ☑
Number of Frames Between Reference: 60
Minimal Number of Reference Images to be Averaged **: 1
Average all reference images and apply as single reference ☑
** Note: # of ref images to be averaged could be adjusted to avoid over-exposure

Reconstruction
Reference and Auto Recon: Collect Reference but no auto recon
☑ Estimate center shift
Or use this center shift (pixels): 0
Output data type: USHORT(16bit)
Recon binning: 1
Beam hardening config file: Standard Beam Hardening Correction
Beam hardening constant: 0
Ring removal: None: no ring removal
Defect correction: Bright and dark spots
Recon filters: Smooth (Kernel Size = 0.5)

Byte scaling
Use the following min and max for byte scaling. (For float data, this value will be used to scale the data in 3DViewer) ☐
Global minimal: 0
Global maximum: 0
Apply CTScale ☐
CTScale Filter:

Turn OFF source once all recipes are done ☑

Registration point
Registration X Position(um): 0
Registration Y Position(um): 0
Registration Z Position(um): 0
Update to the current registration point

Saving
File storage directory
C:\Documents and Settings\xradia\Desktop\scan_data\Fl
File base name: Acid_Plant_Feed_4X_70kV_10secs
Comment:

Tomography Locations
X Dist from Reg point (um): 456.088
Y Dist from Reg point (um): -25690.5
Z Dist from Reg point (um): -601.95
Add the list of tomography locations from the current image
X = 456.09um Y = -25690.50um Z = -601.95um

Time and Space Required
Time : 04 : 18 : 31
Space : 2034.00 MB

Operations

Figure 3.30. Recipe used for HRXMT scan of acid plant feed.

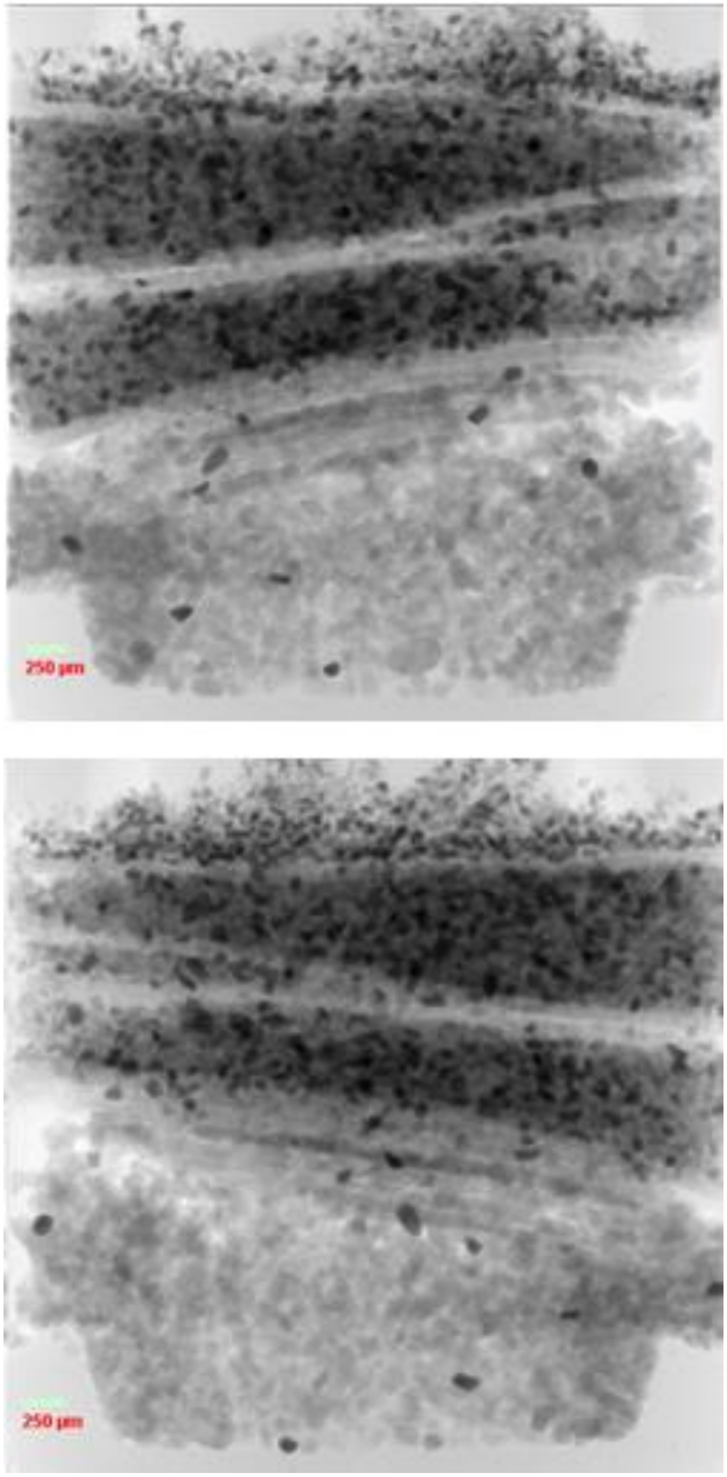

Figure 3.31. Some of the shaking table concentrate projections taken during HRXMT before reconstruction.

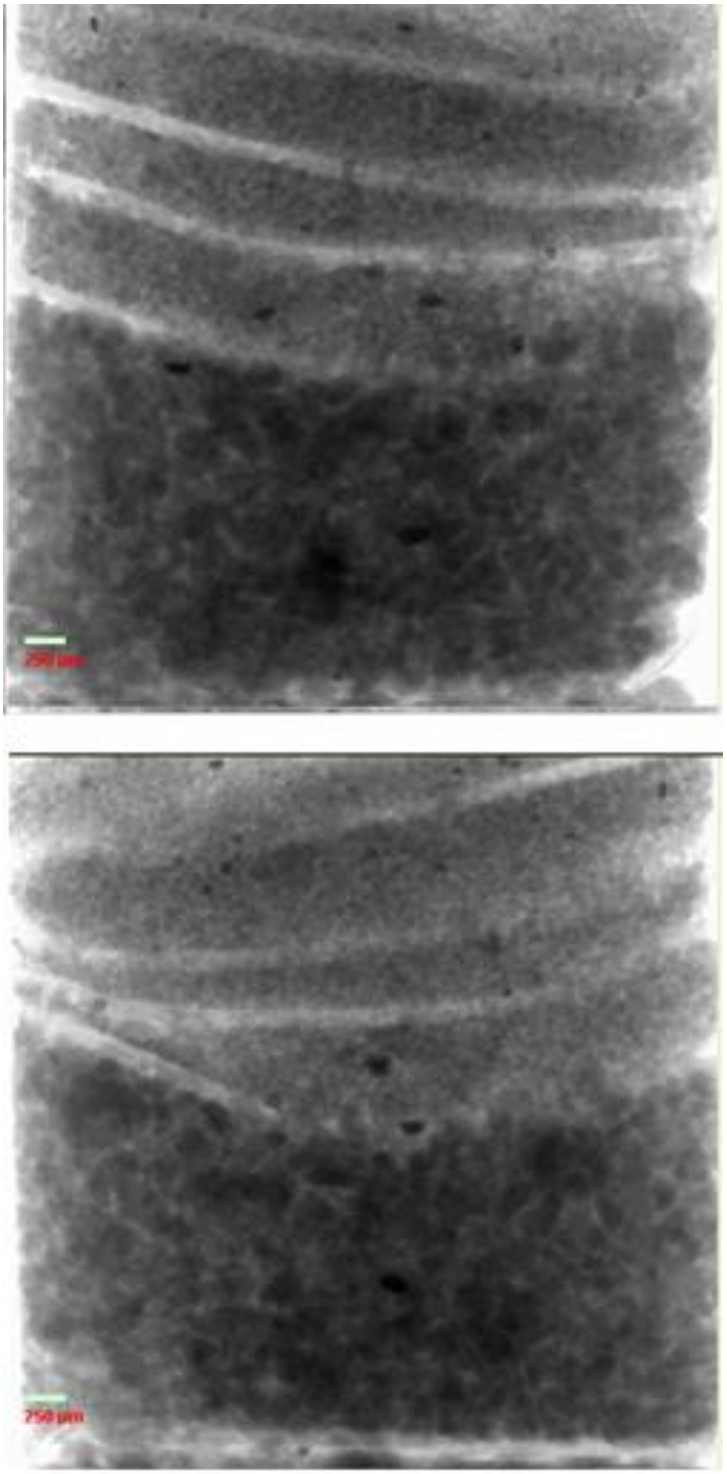

Figure 3.32. Some of the acid plant feed projections taken during HRXMT before reconstruction.

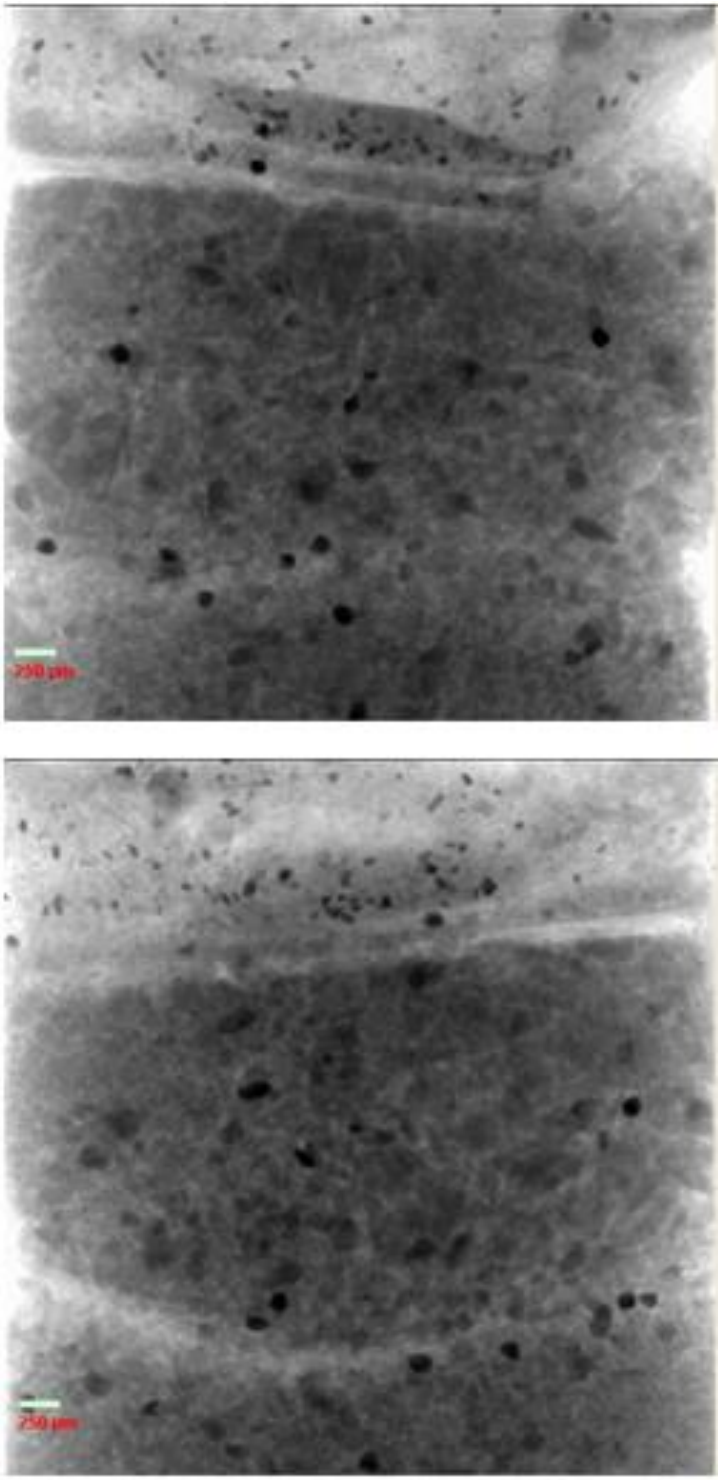

Figure 3.33. Some of the phosphogypsum projections taken during HRXMT before reconstruction.

standard. The beam hardening for all three samples was chosen to be one, as this was the same value chosen for the rare earth mineral standard, and the conditions need to be the same for the standard to be applied. The 3D reconstructions of each sample are shown in Figure 3.34 and will be further discussed in the results section.

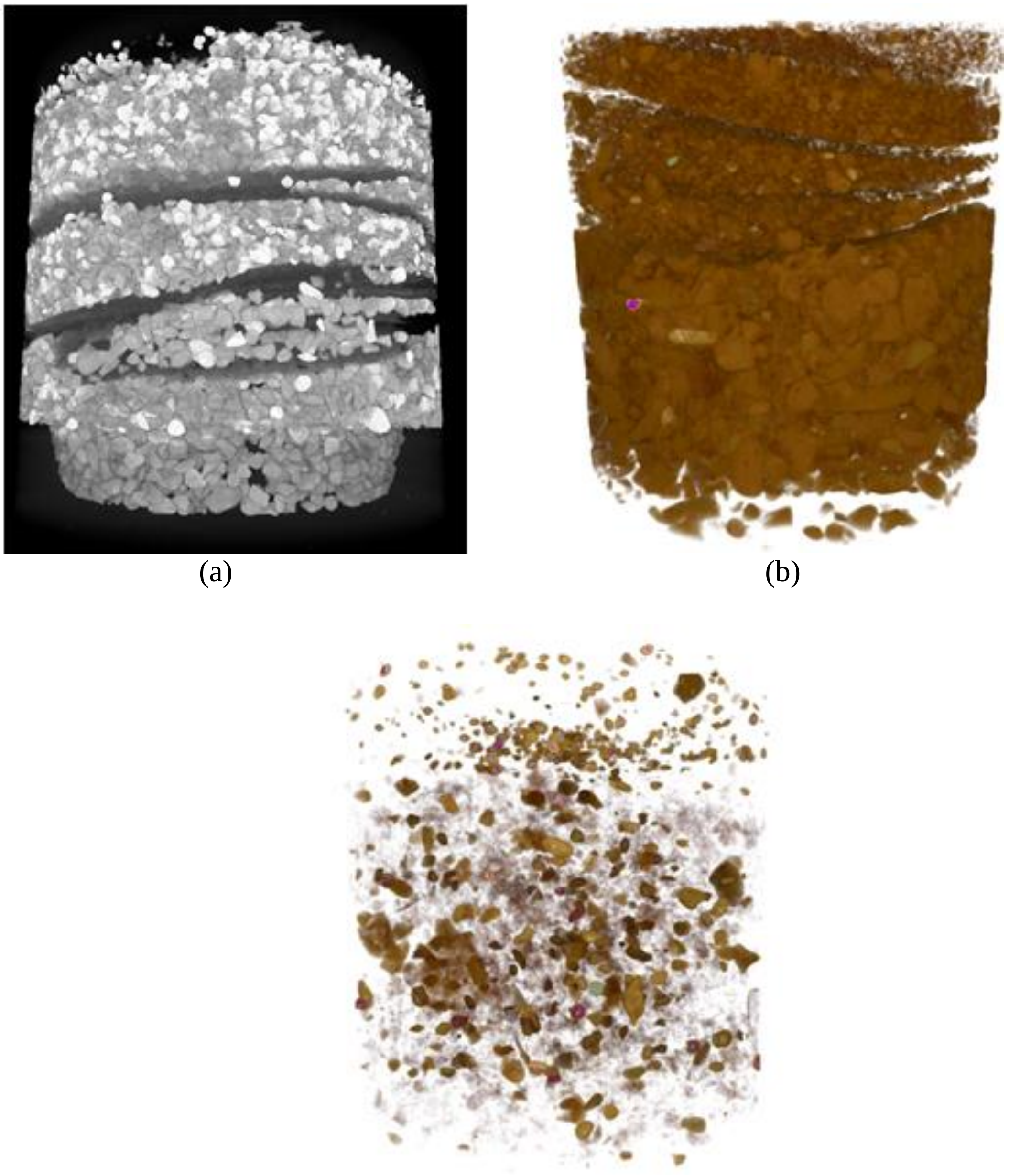

(a)

(b)

(c)

Figure 3.34. Rendering from 3D reconstructed image set of (a) shaking table concentrate, (b) acid plant feed, and (c) phosphogypsum. The shaking table concentrate is shown using XM3DViewer, and the acid plant feed and phosphogypsum were created using Drishti. Note that the blank lines within the samples are the paper used to separate samples from different slides.

CHAPTER 4

RESULTS

4.1 Particle Analysis

Out of the 27 slides scanned using DE radiography, 11 slides had no potential RE particles after thresholding. The number of sections removed from each slide and which slides contained potential RE particles can be seen in Table 4.1. The breakdown of the final 3D reconstruction of each HRXMT sample by mineral is shown in Figures 4.1, 4.2, and 4.3. For comprehensiveness, several 2D slices of each sample are also included in Figures 4.4, 4.5, and 4.6, generated using ImageJ. The final mineral count per sample was found using the 3D Object Counter plugin through ImageJ and using the thresholding values per mineral found in Figure 3.10. The final mineral count can be found in Table 4.2.

During the final thresholding of the particles, there was some inevitable overlap between the monazite scaled CT numbers and the zircon scaled CT numbers, as shown in Figure 3.10. There could be some error in the particles identified as monazite. Per sample, 18 particles from the shaking table concentrate, five particles from the acid plant feed, and seven particles from the phosphogypsum belong to this somewhat nebulous zone. However, as these are at the very edge of the zircon identification zone, where the scaled CT number is between 9000 and 10000, it was ultimately decided that these particles are most likely monazite, and so they were counted in the RE particle category.

Table 4.1. Amount of sections with potential RE particles on each slide

Sample Stream	Size Range	Slide Number	# of sections with potential RE particles
Shaking Table Concentrate	>106 µm	2	3
Shaking Table Concentrate	>106 µm	3	3
Shaking Table Concentrate	75–106 µm	11	8
Shaking Table Concentrate	75–106 µm	13	5
Shaking Table Concentrate	53–75 µm	22	1
Acid Plant Feed	>106 µm	32	2
Acid Plant Feed	>106 µm	33	8
Acid Plant Feed	75–106 µm	41	8
Acid Plant Feed	75–106 µm	42	6
Acid Plant Feed	75–106 µm	43	3
Acid Plant Feed	53–75 µm	53	10
Phosphogypsum	>106 µm	61	11
Phosphogypsum	>106 µm	62	14
Phosphogypsum	75–106 µm	71	1
Phosphogypsum	75–106 µm	72	7
Phosphogypsum	53–75 µm	82	12

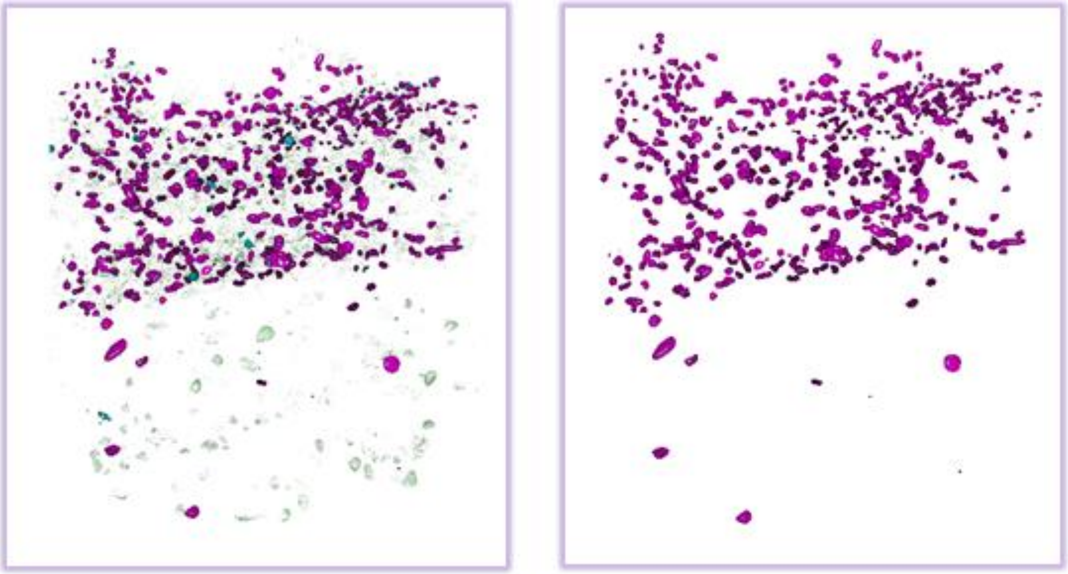

(a) all minerals (b) monazite

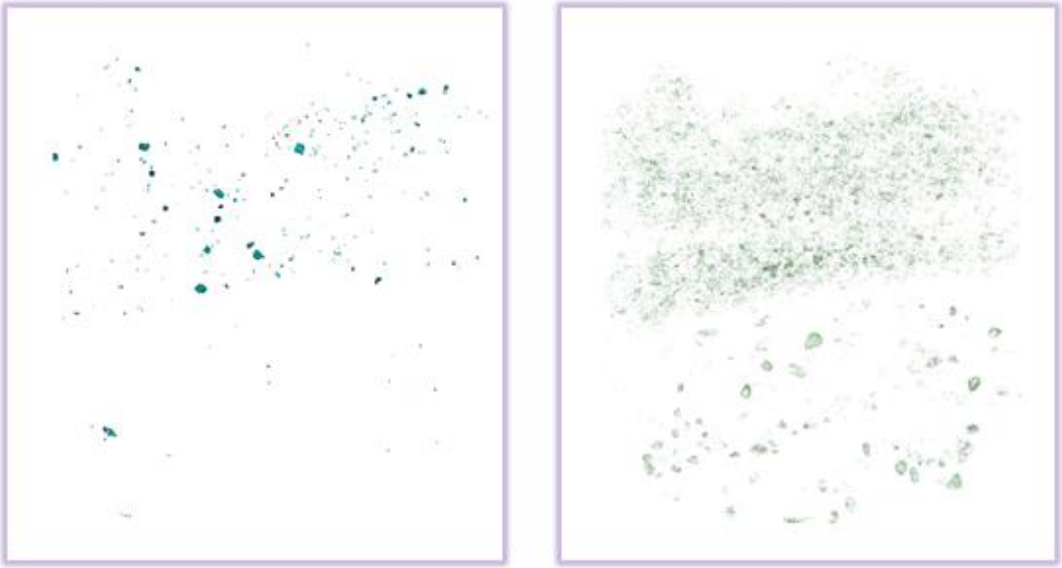

(c) zircon (d) apatite

Figure 4.1. Shaking table concentrate 3D rendering from reconstructed image set broken down by mineral composition using Drishti.

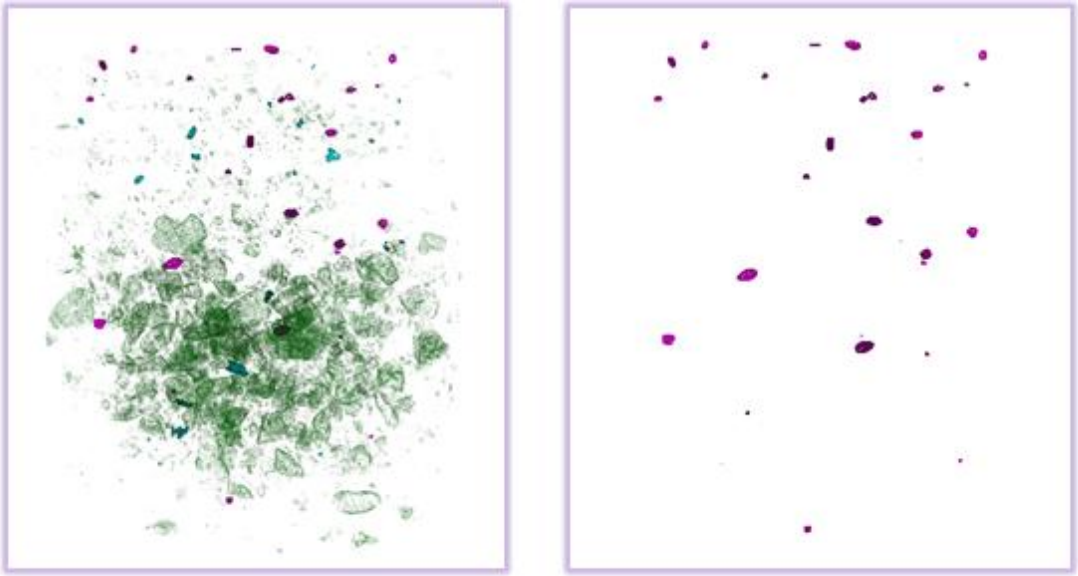

(a) all minerals (b) monazite

(c) zircon (d) apatite

Figure 4.2. Acid plant feed 3D rendering from reconstructed image set broken down by mineral composition using Drishti.

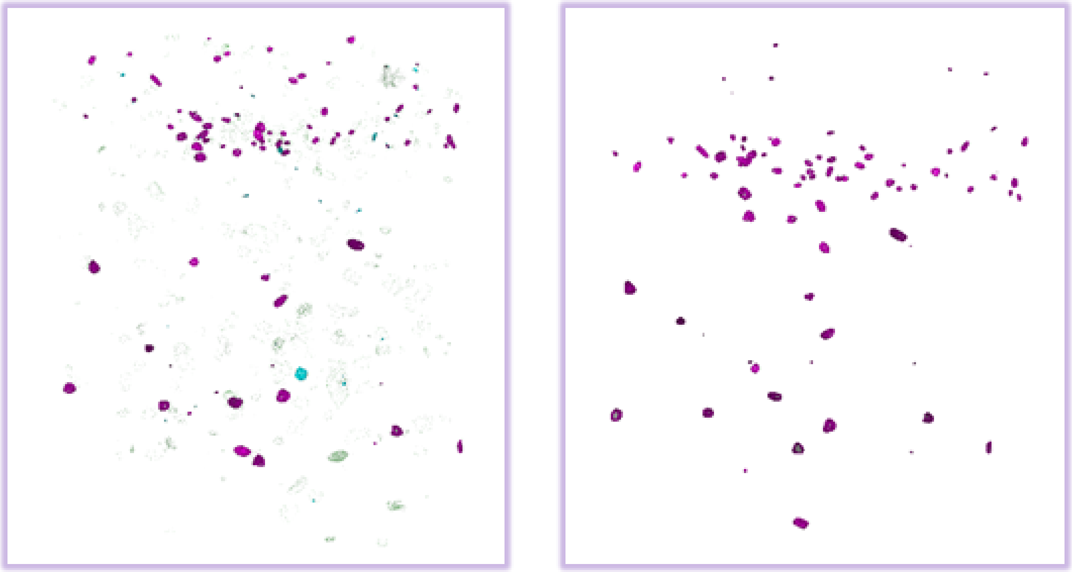

(a) all minerals (b) monazite

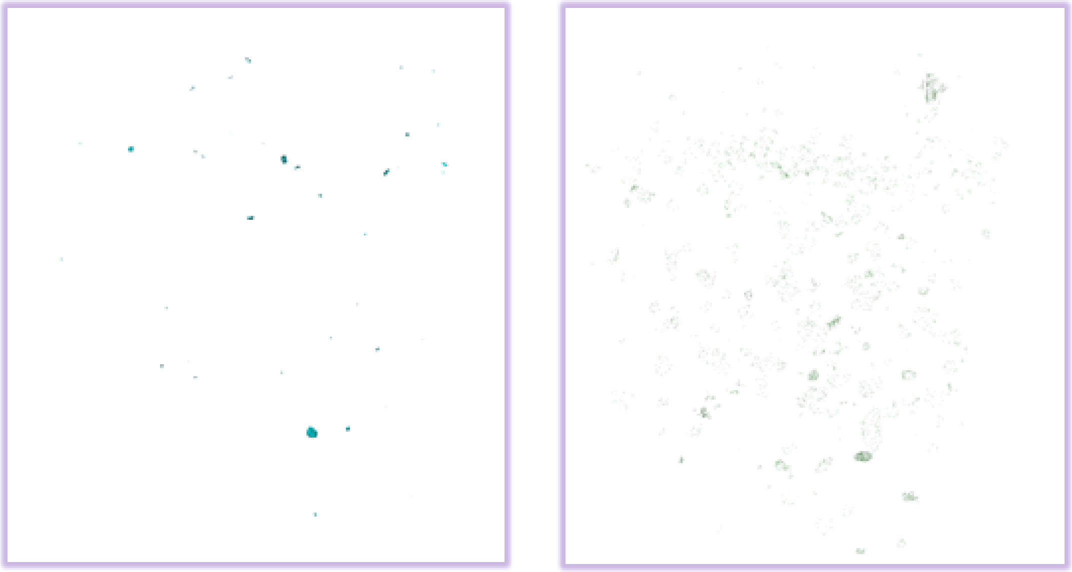

(c) zircon (d) apatite

Figure 4.3. Phosphogypsum 3D rendering from reconstructed image set broken down by mineral composition using Drishti.

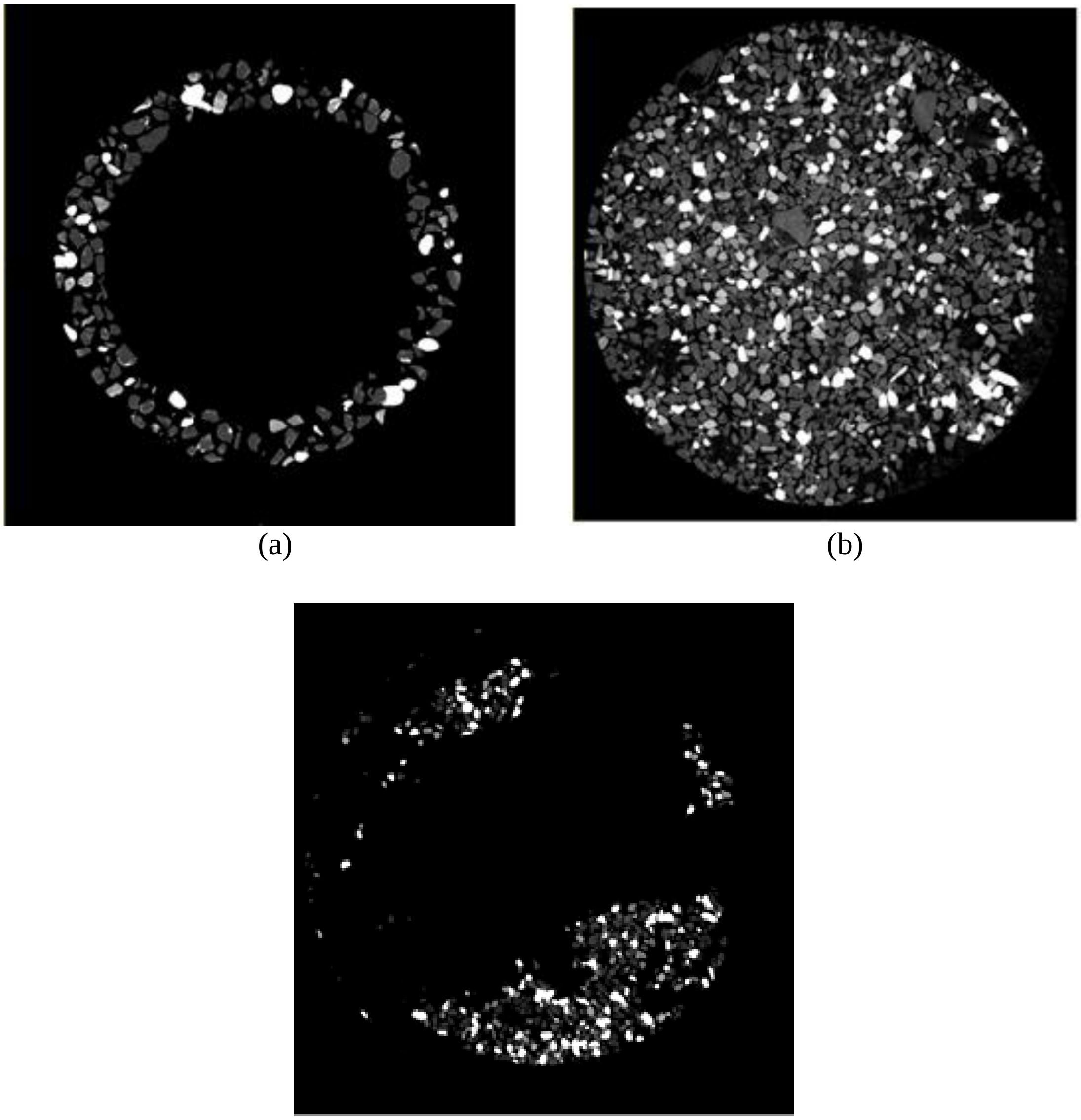

(a) (b)

(c)

Figure 4.4. 2D slice of 3D reconstructed image set of the shaking table concentrate, taken at the section of the sample where the particles of the size class (a) >106 µm, (b) 75–106 µm, and (c) 53–75 µm were located. Note the bright white particles, which are the monazite particles, and the light gray particles, which are the zircon particles, and the pure black spaces running through the images, which are the paper dividers.

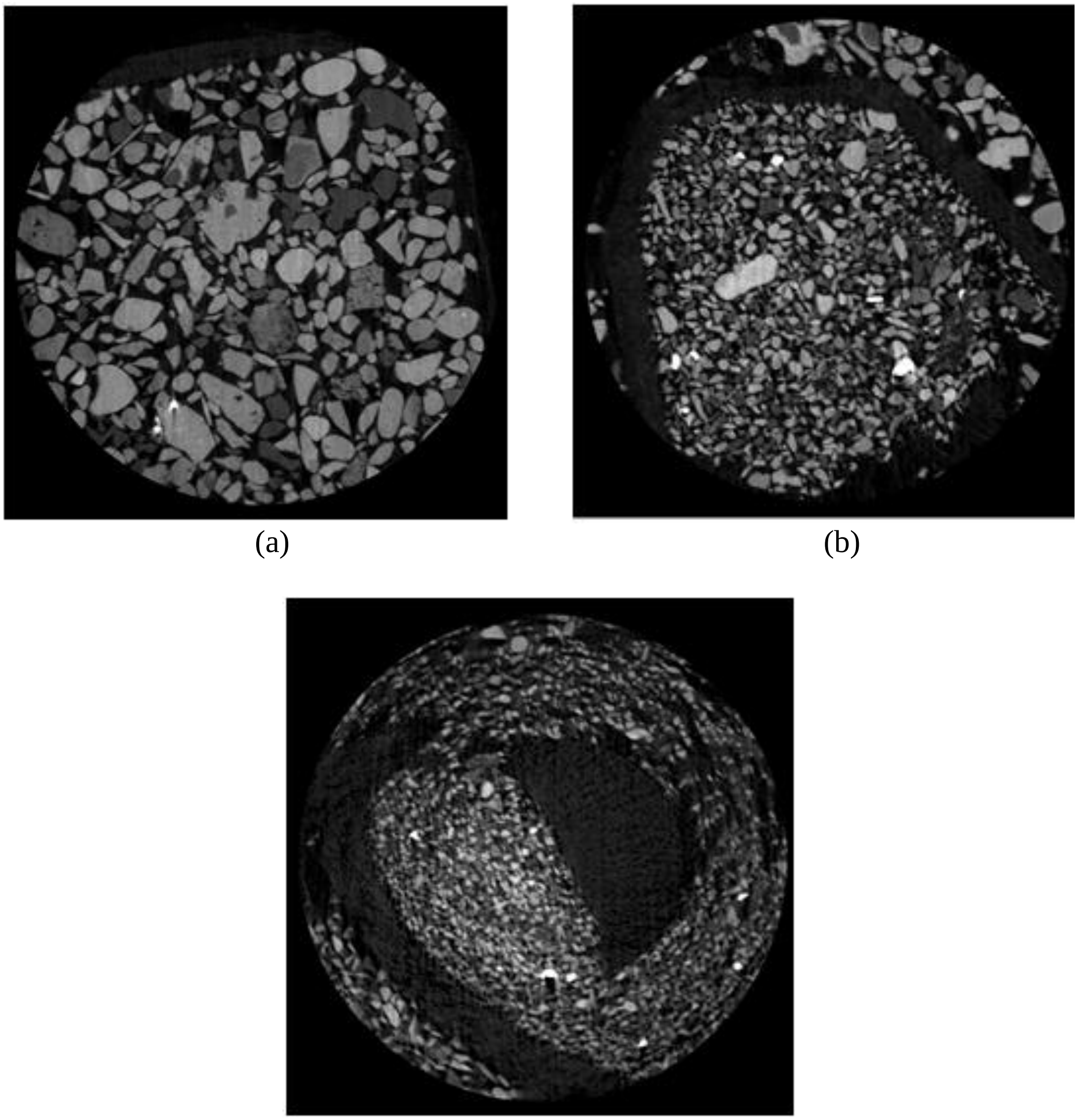

(a)

(b)

(c)

Figure 4.5. 2D slice of 3D reconstruction image set of the acid plant feed, taken at the section of the sample where the particles of the size class (a) >106 μm, (b) 75–106 μm, and (c) 53–75 μm were located. Note the bright white particles, which are the monazite particles, and the light gray particles, which are the zircon particles, and the pure black spaces running through the images, which are the paper dividers.

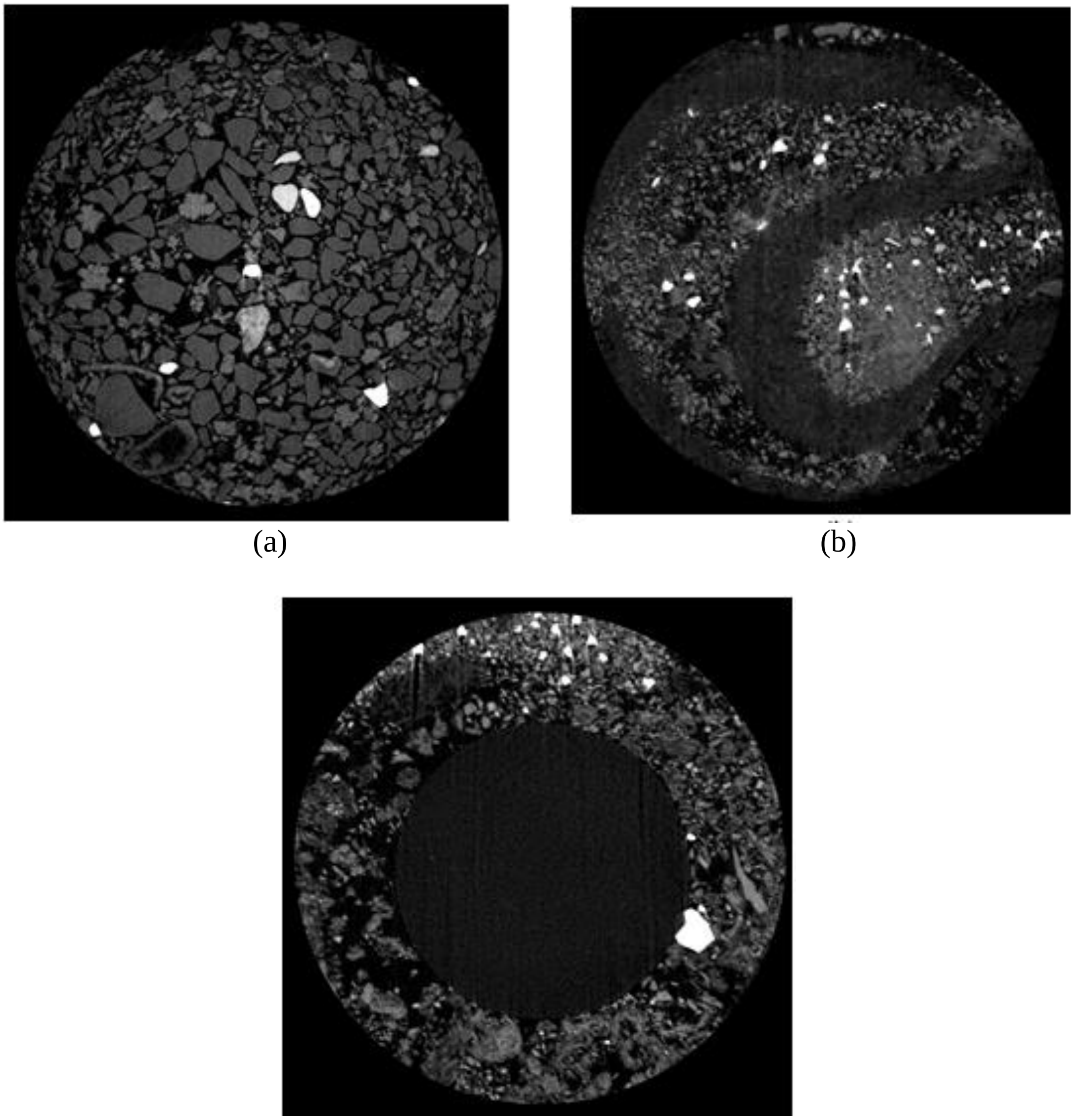

(a)

(b)

(c)

Figure 4.6. 2D slice of 3D reconstructed image set of the phosphogypsum, taken at the section of the sample where the particles of the size class (a) >106 μm, (b) 75–106 μm, and (c) 53–75 μm were located. Note the bright white particles, which are the monazite particles, and the light gray particles, which are the zircon particles, and the pure black spaces running through the images, which are the paper dividers.

Table 4.2. Final mineral count per sample

Shaking Table Concentrate		# of particles found in HRXMT sample	Particle count in ppm
	Monazite	660	2157
	Zircon	1169	3820
Acid Plant Feed			
	Monazite	32	104
	Zircon	233	761
Phosphogypsum			
	Monazite	87	284
	Zircon	193	631

Of those identified as zircon, 164 particles from the shaking table concentrate, 26 particles from the acid plant feed, and 28 particles from the phosphogypsum also belong to the region covered by both monazite and zircon. However, the scaled CT numbers in this range, between 8000 and 9000, are closer to the peak of the zircon region and are only at the edge of the monazite region, so the particles can be reasonably identified as zircon. Therefore, the ppm count shown in Table 4.2 can be concluded as accurate in respect to the given mineral standard.

Using ImageJ, a visual examination of each sample can determine the degree of liberation of the monazite particles. Because the DE slides were separated in the HRXMT samples by paper, it is possible to look at each size class individually to examine the degree of liberation for each size class of each sample. For the shaking table concentrate, the monazite particles in all three size classes are fully liberated, an example of which can be seen in Figure 4.7. Additionally, reexamining the monazite breakdown by approximate size classes, found in Figure 4.8, notice that the majority of the monazite is found at the top of the sample. All three HRXMT samples were prepared so that the largest particles were found at the bottom and the smallest at the top. However, because the shaking table concentrate only contained one section of one slide in the size range 53–75 µm, most of these particles near the top of the sample were located on the slides with particle size 75–106 µm. This means that the majority of the monazite particles can be found in this size range and fully liberated, making it the optimum size for grinding and processing.

The phosphogypsum is liberated to a similar degree. In the size range >106 µm, the majority of the monazite particles are fully liberated, like the example shown in Figure 4.9, though with a few particles that are partially locked, making about a 95% degree of liberation. For the size classes 75–106 µm and 53–75 µm, all the monazite

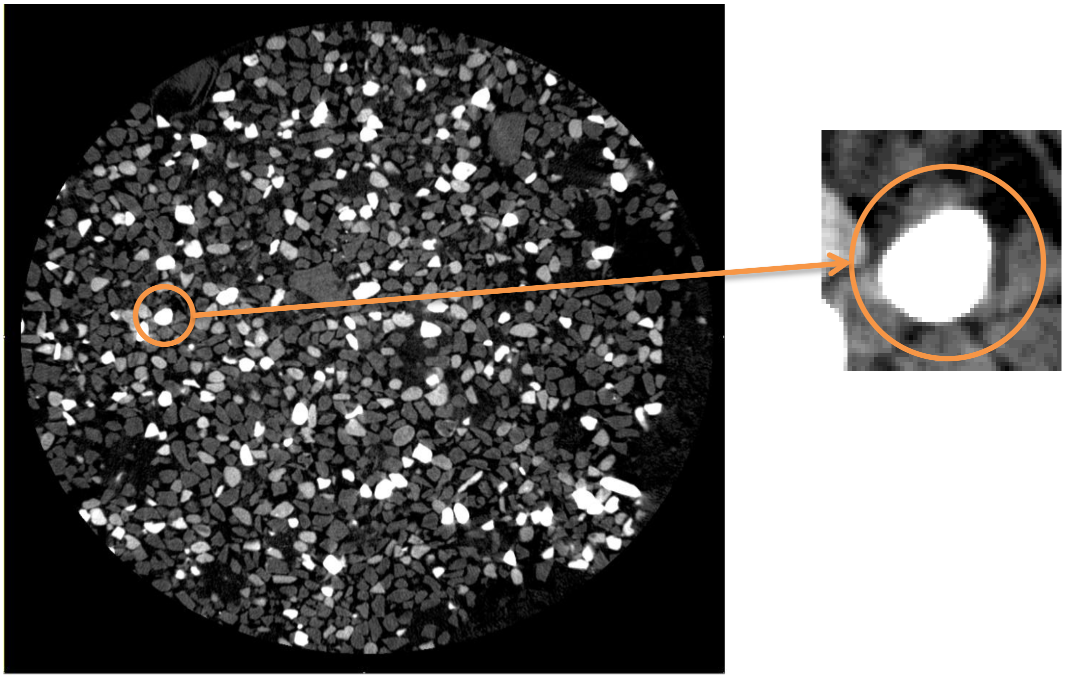

Figure 4.7. An example of a 2D reconstruction slice of shaking table concentrate displaying a fully liberated particle in the size class 75–106 µm.

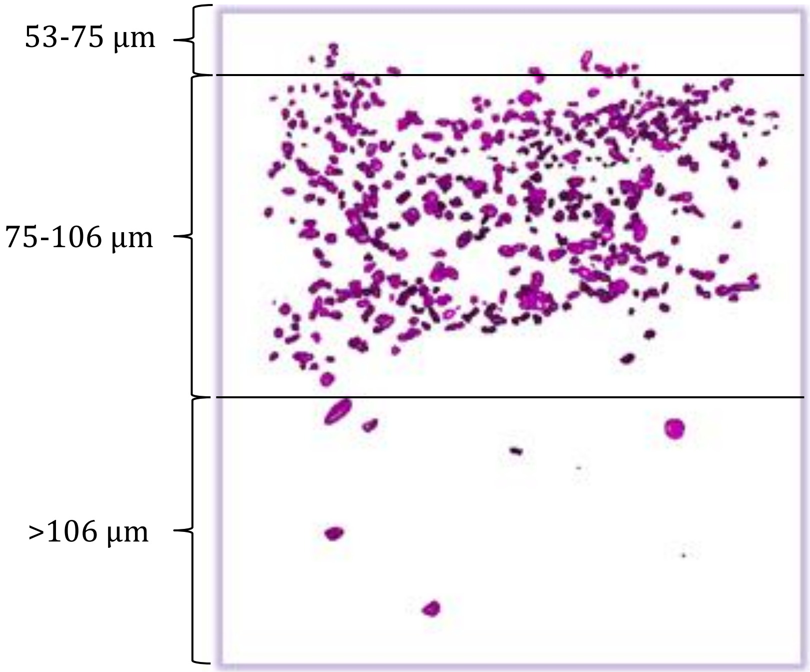

Figure 4.8. Monazite particles in 3D rendering from reconstructed image set of shaking table concentrate approximately broken down by size classes.

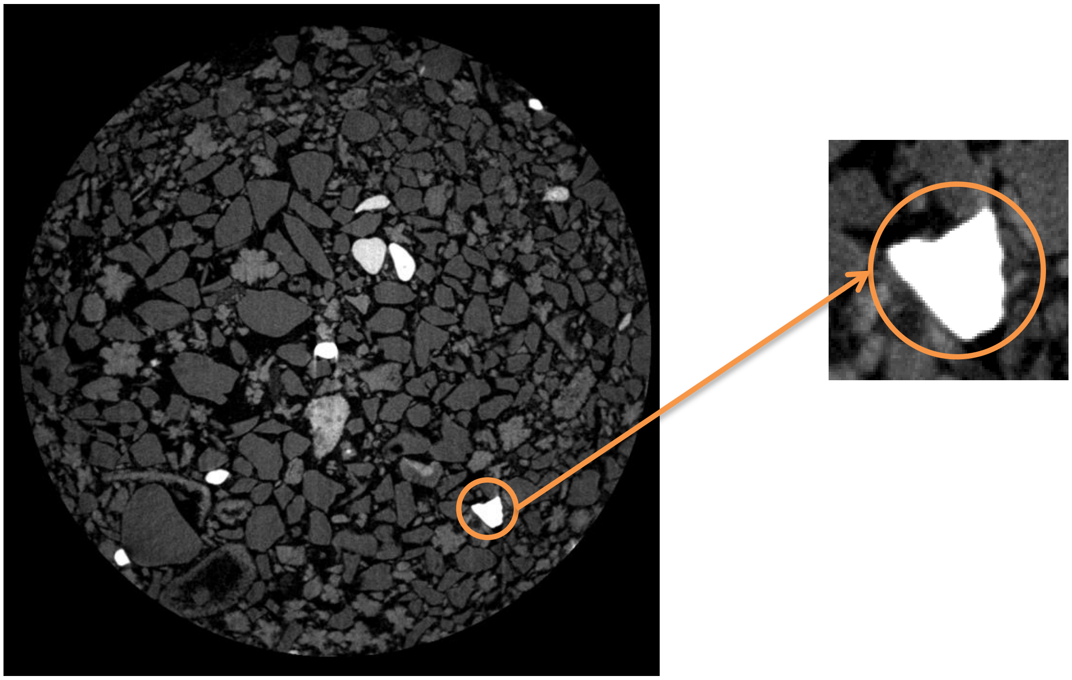

Figure 4.9. An example of a 2D reconstruction slice of phosphogypsum displaying a fully liberated particle in the size class >106 µm.

particles are fully liberated. As is visible in Figure 4.10, The phosphogypsum sample has a similar grouping as the shaking table concentrate further from the top of the sample, where particles from the 75–106 μm were located as well. However, there are many particles grouped together throughout the rest of this sample as well, especially in the >106 μm range. Because the majority of the RE particles are liberated as well, the optimum size range cannot be stated as clearly as the shaking table concentrate, but should be in the approximate range of 75–106 μm, although a larger size could reasonably be considered.

The acid plant feed had a bit different liberation analysis than the other two samples. For the size class >106 μm, the majority of the monazite particles are not liberated at all, such as the example shown in Figure 4.11. In fact, the RE particles are

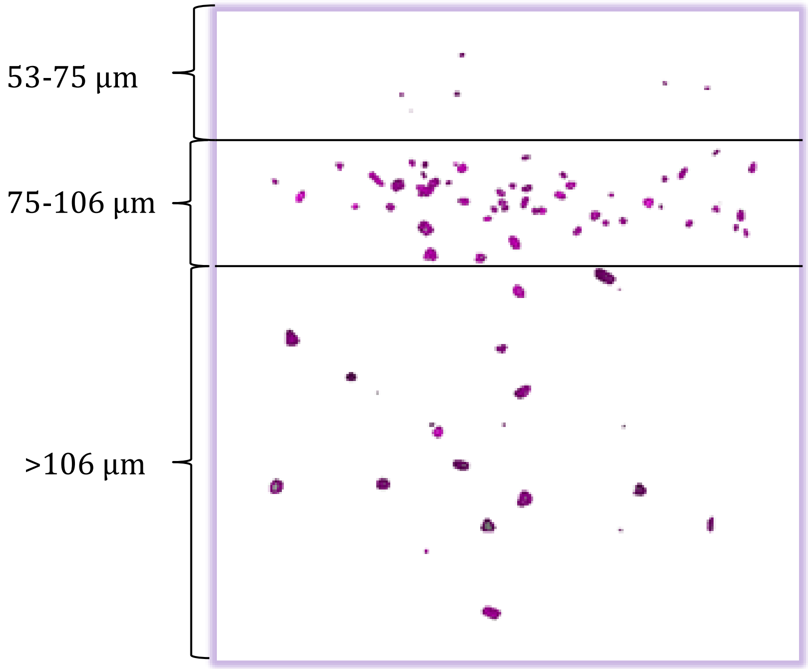

Figure 4.10. Monazite particles in 3D rendering from reconstructed image set of phosphogypsum approximately broken down by size classes.

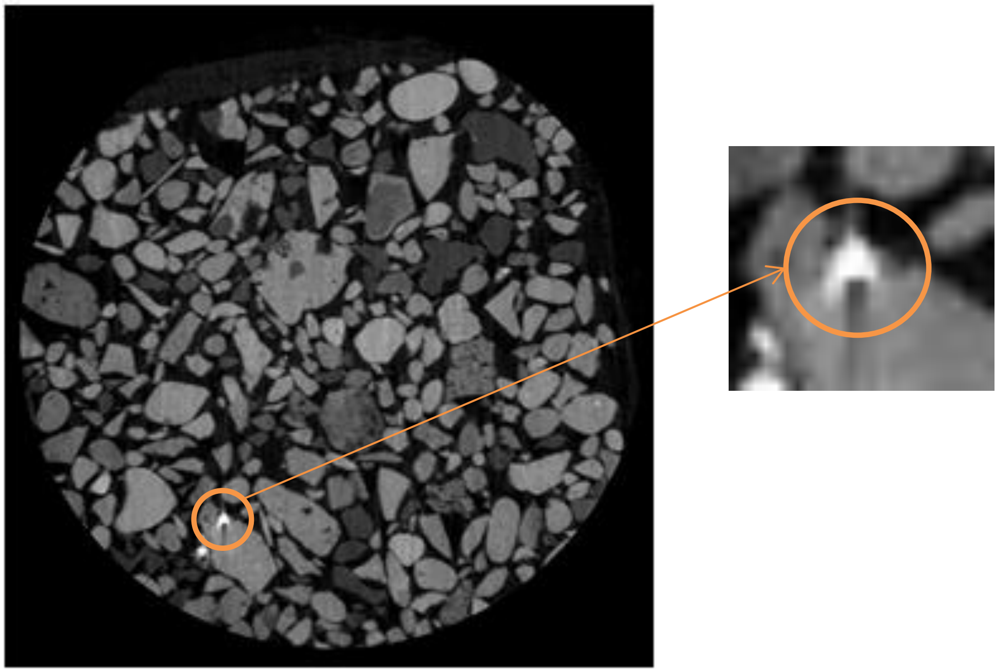

Figure 4.11. An example of a 2D reconstruction slice of acid plant feed displaying a locked particle in the size class >106 µm.

about 95% fully locked. However, in the smaller size ranges, the monazite is nearly fully liberated. As shown in the monazite mineral breakdown in Figure 4.12, like the other two samples, only a small amount of the HRXMT sample came from the size range 53–75 µm, therefore making this size range not ideal for grinding, even though monazite particles in this size range are fully liberated. The acid plant feed has a much lower concentration of monazite than the other two samples, and it is concentrated relatively uniformly throughout the sample and throughout the size groups. Because the particles >106 µm are not liberated, but not many particles from 53–75 µm were potential RE minerals, the size class 75–106 µm should be considered as a good size range for monazite retrieval.

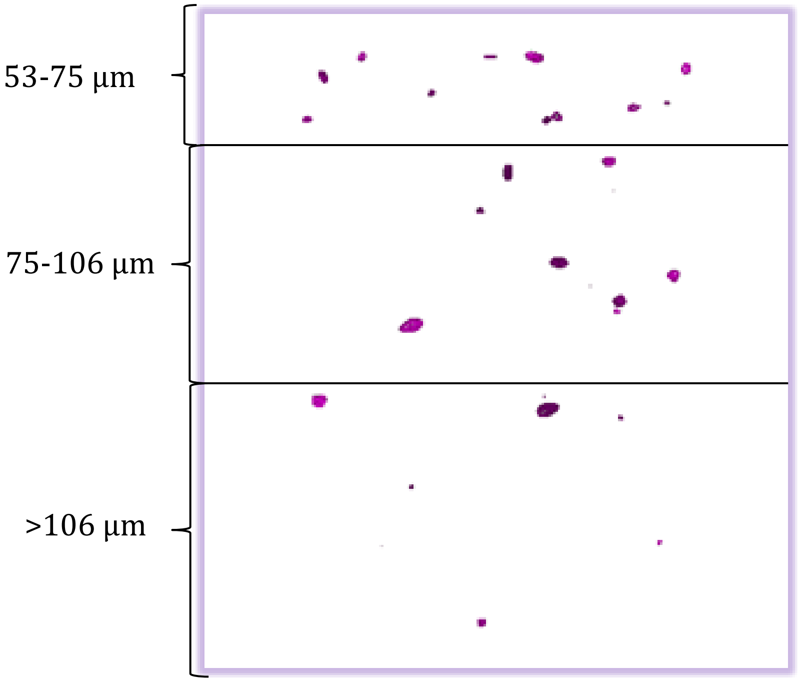

Figure 4.12. Monazite particles in 3D rendering from reconstructed image set of acid plant feed aproximately broken down by size classes.

4.2 Particle Analysis Verification

In order to verify the radiography/tomography concentration analysis, provided for comparison purposes in Table 4.3, and compare different methods of resource identification, the institute provided an approximate chemical analysis of the shaking table concentrate and acid plant feed, shown in Tables 4.4 and 4.5. While the radiography/tomography concentrations follow the trend from the chemical analysis, meaning that the shaking table concentrate has a higher RE mineral concentration than the acid plant feed, the concentration for the acid plant feed is much lower than anticipated from the provided analysis.

Part of this error can be explained due to a portion of all the samples, the particles that were <53 µm, being excluded from this scanning process. If a large number of RE particles were in this size class, the radiography/tomography concentration results could

Table 4.3. Radiography/tomography RE concentration

Sample	RE ppm
Shaking Table Concentrate	2157
Acid Plant Feed	104
Phosphogypsum	284

Table 4.4. Provided chemical analysis of acid plant feed

	ICP P2O5	Lachat P2O5	Insol	MgO	Fe2O3	Al2O3	CaO
Acid Plant Feed	26.46	27.36	15.84	0.50	1.19	1.19	38.84

	Pr ppm	Eu ppm	Tb ppm	Dy ppm	Ho ppm	Er ppm	Tm ppm
Acid Plant Feed	7.92	3.48	2.17	13.81	3.25	9.62	1.22

	Yb ppm	Lu ppm	Sc ppm	Gd ppm	Sm ppm	Th ppm	U ppm
Acid Plant Feed	8.69	1.34	4.90	16.46	12.04	9.15	87.77

	Ce ppm	Y ppm	La ppm	Nd ppm	Total RE ppm
Acid Plant Feed	131.16	132.06	77.58	85.26	607.88

Table 4.5. Provided estimated chemical analysis of shaking table concentrate

	ICP P2O5	Lachat P2O5	Insol	MgO	Fe2O3	Al2O3	CaO
Shaking Table Con	6–9	6–9	70–80	0.03–0.08	0.29–0.9	0.28–0.8	8–15

	Pr ppm	Eu ppm	Tb ppm	Dy ppm	Ho ppm	Er ppm	Tm ppm
Shaking Table Con	10–16	2–3	0.5–0.7	5.0–7.5	2–3	6–11	1.0–1.5

	Yb ppm	Lu ppm	Sc ppm	Gd ppm	Sm ppm	Th ppm	U ppm
Shaking Table Con	4–6	0.10–0.15	3.0–4.5	8–11	10–18	8–10	30–50

	Ce ppm	Y ppm	La ppm	Nd ppm	Total RE ppm
Shaking Table Con	130–150	70–100	60–90	80–110	430.3–592.35

be severely skewed in this manner, lowering the resulting concentration from its anticipated value or the value shown in other test results. If this is the case, this size class is most likely the ideal size to find RE particles in this particular sample stream. However, some error could also be caused by RE particles not being properly transferred to the HRXMT sample after DE identification or RE particles not being identified on the DE slides in the first place and so were not transferred to the HRXMT sample. For this to happen, there could have been a manual error in the physical process of removing the particles or an error due to an incorrect thresholding value, most likely in the DE radiography stage. The lower than expected concentration for the acid plant feed from radiography/tomography could be caused by any of the three described scenarios or all three compounded.

It was not expected that much of the concentration error seen here was due to the DE thresholding value. This was because of the earlier confirmation of the proposed threholding value using the pure bastnaesite sample, as well as the results from the shaking table concentrate. The radiography followed by tomography used here found a much higher concentration of RE particles than the chemical analysis states. Because the same thresholding value was used for both samples, if it were incorrect, the radiography/tomography concentrations should either both increase or both decrease, but not have one sample increase and one decrease. Therefore, logically, the error from the thresholding value should be slim.

To verify this, it was decided that a new sample from the most densely RE populated size class of the shaking table concentrate should be scanned but in reverse order. To this purpose, an HRXMT sample was prepared using the 75–106 μm size class and scanned using the same conditions as previously stated in Chapter 3. This same sample was then physically deconstructed and placed onto DE slides for DE radiography scanning. The resulting scans were then analyzed for RE particles using the same thresholding as the previous slides.

As expected, the results from these scans corresponded well. Again using the 3D Object Counter plugin through ImageJ, 1734 particles were identified as RE particles in the new HRXMT sample. DE radiography of the same sample provided an estimation of about 2200 particles. The discrepancy between the two values can easily be explained by the possibility of the thresholding value being too low, as previously described in section

3.5 so that all possible RE particles would be included in further analysis. With this verification, it can be concluded that any error in this experiment is most probably caused by manual error during the transferring process or due to a portion of the bulk sample being excluded from the analysis.

4.3 Time Comparison

One important aspect of this project was getting an accurate accounting of the RE particles contained in the samples on a ppm scale. Another important facet was discovering if using DE radiography followed by HRXMT was more time efficient than just simply scanning by HRXMT. To discover this, the time taken for preparation and scanning at all stages was recorded and compared to previous times recorded for just the HRXMT scans and those for just DE radiography scans. The times are based on the rough estimate that one HRXMT sample contains approximately the same number of particles as three DE slides under the same HRXMT scan conditions. The time taken to separate the samples into size classes (i.e., wet and dry sieving) is not taken into account because this step is necessary for any scanning option and therefore cancels when compared. The times are recorded on Tables 4.6, 4.7, and 4.8.

As can be seen from these tables and their respective total times, DE radiography by itself would be much more time efficient than either of the other two methods. Unfortunately, as described in section 2.2.3 on the theory of DE radiography, there are flaws that can introduce a wide gap of error if DE radiography only is used for resource identification with the machine used for the current project. However, if a machine were employed that was powerful enough to produce sufficiently high energy X–rays so that the accuracy of DE radiography could be increased, this method, by itself, would be

Table 4.6. Recorded times to scan 27 DE slides followed by 3 HRXMT samples

Step	Time per sample	Total time per step
DE slide preparation	5 minutes	135 minutes
DE scans	35 minutes	945 minutes
DE thresholding	5 minutes	135 minutes
HRXMT preparation	15 minutes	45 minutes
HRXMT scans	260 minutes	780 minutes
HRMXT Reconstruction	20 minutes	60 minutes
Final particle identification	20 minutes	60 minutes

Total: 2160 minutes

Table 4.7. Recorded times to scan 9 HRXMT samples

Step	Time per sample	Total time per step
HRXMT preparation	15 minutes	135 minutes
HRXMT scans	260 minutes	2340 minutes
HRMXT Reconstruction	20 minutes	180 minutes
Final particle identification	20 minutes	180 minutes

Total: 2835 minutes

Table 4.8. Recorded times to scan 27 DE slides.

Step	Time per sample	Total time per step
DE slide preparation	5 minutes	135 minutes
DE scans	35 minutes	945 minutes
DE thresholding	5 minutes	135 minutes

Total: 1215 minutes

much preferred. For example, Xradia's Versa machine series offers a higher power flux that allows X–rays to be produced that can penetrate high density materials, as well as a built in dual scan setting that allows for two different X–ray levels to be taken and combined automatically (Carl Zeiss Inc., 2013). Using a machine with these capabilities would radically reduce the time required for particle identification and characterization to that described in Table 4.5, or even less, making it the ideal solution, if available. Because a Versa machine was not an option for this project, the comparison between DE radiography in addition to HRXMT and only HRXMT provides a more practical result.

Therefore, based on the time tables, it can be seen that using DE radiography followed by X–ray tomography is much more time efficient that scanning the same amount of particles by only HRXMT. Based only on these numbers, 675 minutes are saved by using the proposed methodology. As it is, this could be an underestimate. The assumption here was that it would take the particles on just three DE slides to make one HRXMT sample. However, that is based on an average particle diameter of about 96 μm. The estimate is fitting for this project because in two out of the three samples, the majority of the particles came from the size range of 75–106 μm, and the majority of the third came from >106 μm. If the average particle size is larger than this, however, the number of particles per HRXMT sample can be much lower, even so much that there is nearly a one to one ratio between the number of particles on the slide and the number in an HRXMT sample. It is easy to see that using DE radiography to identify potential particles of interest and using X–ray tomography to verify those particles is much more time efficient, by a minimum of nearly 11 ½ hours, than scanning the same amount of particles by only HRXMT.

4.4 Results Discussion

Based on the results given in the previous sections, it is clear that the methodology of using DE radiography to identify potential particles of interest and then verifying using HRXMT is highly effective and more efficient than simply completing HRXMT on the entire sample, especially in regards to RE minerals. This can be seen in particular when examining the acid plant feed sample. As the sample with the least concentrated monazite, more particles must be scanned for this sample in order to get a reliable estimate of its concentration. Without being able to concentrate the HRXMT sample with potential RE particles, finding the concentration could take hours longer.

Being more time efficient is not the only advantage to this method. As the shaking table concentrate sample demonstrates, arranging the HRXMT by size classes from the DE slides allows for not only quantitatively identifying the particles of interest, but also the best size range to find the mineral. This could lead to valuable information regarding the ideal grind size for these particles if they were to be mined on an industrial scale. By allowing for the preconcentration of the potential RE particles by DE radiography, this information becomes readily apparent in the 3D images without having to compare hundreds of particle sizes in multiple scans and scan data, which is both difficult and allows for further possibilities of mistakes.

Realistically, the time saved in this particular project is not so great as to make that much of a difference in this specific situation. Eleven hours can be made up for within a week or two without too much effort. However, the results from this project can lead to the foundation of future projects where the time difference between these two methodologies is much greater. For example, in this project, only approximately 306,000 particles of each sample type were scanned and analyzed. If a project were to be embarked upon that required many more particles than this to be analyzed, knowing that DE radiography followed by X–ray tomography is more time efficient than simply jumping straight to HRXMT scanning could potentially save weeks or even months of work. Supposing that the machine had to be shared between multiple projects, and so using this methodology saved 2 weeks on this particular project, it is easy to see how scanning particles on a magnitude of only three times greater could save 6 weeks or more of work. A project only three times greater in magnitude than this one would be scanning approximately a million particles of each sample which, considering the concentration of RE particles on a ppm scale, is a completely reasonable expectation to have for a research project at the university. Saving 6 weeks of work could make a big difference for both the company desiring the data as well as the researchers themselves, allowing more time for future steps in the project to be completed or proceed ahead of schedule or more time for other projects altogether.

Between the advantages of both the preconcentration of the HRXMT sample leading to potentially useful size grinding and liberation information as well as being more time efficient than straight HRXMT scanning, the proposed methodology has proven that it is a valuable process to be used in future projects.

CHAPTER 5

SUMMARY

Because accurate and efficient particle identification is increasingly becoming a topic of concern in the mineral processing industry, it was proposed that dual energy (DE) radiography followed by high resolution X–ray microtomography (HRXMT) be used to identify rare earth (RE) particles in several sample streams from the Florida Industrial and Phosphate Research Institute. These two processes were chosen in conjunction because the flaws of one method were benefits of the other. DE radiography is extremely time efficient, especially compared to HRXMT. However, DE radiography has difficulties distinguishing between materials of similar densities and effective atomic numbers. In contrast, one of the prominent features of HRXMT is the ability to differentiate between any two materials, regardless of their similarities in effective atomic numbers. By using both methods together, it was proposed that both time would be saved and more useful data gathered at the same time.

In order to prove this methodology, the times for each step of the project were recorded and compared to the times it would take to complete the same project by only HRXMT. In addition, the final 3D reconstructions were examined to see if any useful data could be gathered by the preconcentration caused by the preliminary DE radiography that may have been overlooked by skipping this step and jumping straight to HRXMT. The hope for this proposal was that if proven correct, this methodology could be used for future projects to improve accuracy, save time, and gather more detailed data about the samples being researched. This method was proposed for this particular project with the Florida Industrial and Phosphate Research Institute due to the difficulty in identifying RE particles as a general rule. Because RE particles are generally only available on a ppm scale, they are easily overlooked by other methods, and so identifying them in several sample streams was a prime test for the proposed methodology.

The proposed methodology involved the following steps for the project: particle separation, calibration, DE slide preparation, DE scans, DE analysis, HRXMT sample preparation, HRXMT scans, HRXMT reconstruction, and results analysis. Once these steps were completed, the total time for each step, excluding the first, were totaled and compared to the time necessary for the same number of particles to be scanned only by HRXMT under the same conditions.

Based on the results from this project, the proposed methodology has proven itself to be a useful process and should be considered for future projects. Based on the size concentration data the shaking table concentrate sample provided, this methodology could provide useful data that would be much more difficult to see as a trend in an HRXMT sample that was not concentrated by DE radiography beforehand. Based on the time measurements, this methodology could save weeks or months of time, depending on the breadth of the project and the concentration of the samples in question.

It is my belief, supported by the results contained within this thesis, that using DE radiography to identify potential particles of interest and following it with HRXMT scanning to quantitatively identify these desired particles provides useful data that would be hard to come by using other processes. This saves valuable time and should be considered as a possible avenue of research for future projects requiring particle identification on a parts per million scale.

APPENDIX A

SOLVING FOR MATERIAL THICKNESS USING DE RADIOGRAPHY

Continued from equation 2 in section 2.2.3. When two materials A and B of differing densities and thicknesses and therefore attenuation coefficients are placed side by side, equation 2 can be rewritten to be

$$\ln\left(\frac{I}{I_0}\right) = -\mu_A(E) * x_A - \mu_B(E) * x_B \qquad \text{(A.1)}$$

This is also called the log transmission. Because there are two unknowns in this equation, x_A and x_B, two equations are needed to solve for them. This is the point where DE radiography can be applied. By taking scans at both low and high energy levels, the following system of equations can be created:

$$\ln\left(\frac{I_L}{I0L}\right) = -\mu_A(E_L) * x_A - \mu_B(E_L) * x_B \qquad \text{(A.2)}$$

$$\ln\left(\frac{I_L}{I0H}\right) = -\mu_A(E_H) * x_A - \mu_B(E_H) * x_B \qquad \text{(A.3)}$$

Solving for the unknowns creates the equations

$$x_A = \frac{1}{\Delta}(-\mu_B(E_H)LA_L - \mu_B(E_L)LA_H) \qquad \text{(A.4)}$$

$$x_B = \frac{1}{\Delta}(-\mu_A(E_H)LA_L - \mu_A(E_L)LA_H) \qquad \text{(A.5)}$$

where $\Delta = \mu_A(E_L)\mu_B(E_H) - \mu_A(E_H)\mu_B(E_L)$ and the log of the attenuations are $LA_L =$

$\ln\left(\frac{I_{0L}(E_L)}{I_L(E_L)}\right)$ and $LA_H = \ln\left(\frac{I_{0H}(E_H)}{I_H(E_H)}\right)$.

However, polychromatic X–ray sources cannot be solved as easily. Because polychromatic X–rays output photons with a distribution of energy levels instead of just a single energy level, the photon absorption must be solved with a nonlinear function for the log of the attenuations. The solution for polychromatic X–rays is

$$x_A = \frac{a_0+a_1L+a_2H+a_3L^2+a_4LH+a_5H^2}{1+b_0L+b_1H} \tag{A.6}$$

$$x_B = \frac{c_0+c_1L+c_2H+c_3L^2+c_4LH+c_5H^2}{1+d_0L+d_1H} \tag{A.7}$$

The 16 unknown coefficients can be estimated by calibration of five known thickness levels for the two materials A and B and L = LA_L and H = LA_H.

APPENDIX B

MATHEMATICS BEHIND 3D RECONSTRUCTION

To begin the step by step mathematic walk through of the 3D reconstruction, it is easiest to start again with the Radon transform, as in section 2.2.4. As a reminder, the Radon transform is defined as a function's line integral parallel to the y'–axis at a distance x' from the origin. This is denoted by

$$\begin{aligned} p_\varphi(x') &= \Re[f(x,y)] \\ &= \iint_{-\infty}^{\infty} f(x,y)\delta(x\cos\varphi + y\sin\varphi - x')\,dx\,dy \\ &= \int_{-\infty}^{\infty} f(x'\cos\varphi - y'\sin\varphi\,, x'\sin\varphi + y'\cos\varphi)\,dy' \end{aligned} \tag{A.8}$$

Where

$$\begin{aligned} x' &= x\cos\varphi + y\sin\varphi \\ y' &= -x\sin\varphi + y\cos\varphi \end{aligned} \tag{A.9}$$

Or

$$\begin{aligned} x &= x'\cos\varphi - y'\sin\varphi \\ y &= x'\sin\varphi + y'\cos\varphi \end{aligned} \tag{A.10}$$

For the purpose of 3D reconstruction, $p_\varphi(x')$ is the 1D projection of f(x,y) at an angle of φ of the 2D image data, where f(x,y) is a 2D slice of the sample on the xy–plane and each slice in the z–direction is a new and individual function f(x,y) (refer to Figure 2.3 for axis orientation). As the sample rotates, a new Radon transformation is created for each 2D slice. The 2D projection image that is outputted is each Radon transform for that angle of rotation stacked together to create the full image. Figure 2.7 demonstrates this concept visually.

If the 1D Fourier transform is then taken of the projection data, represented by the function $p_\varphi(x')$, it forms the equation

$$\begin{aligned} P_\varphi(\omega) &= \mathcal{F}_1\left[p_\varphi(x')\right] = \int_{-\infty}^{\infty} p_\varphi(x') \exp(-i\omega x')\, dx' \\ &= \iint_{-\infty}^{\infty} f(x'\cos\varphi - y'\sin\varphi, x'\sin\varphi + y'\cos\varphi) \exp(-i\omega x')\, dx'\, dy' \end{aligned} \tag{A.11}$$

By substituting in the change of coordinates in equation set A.9, this becomes

$$= \iint_{-\infty}^{\infty} f(x,y) \exp[-i\omega(x\cos\varphi + y\sin\varphi)]\, dx\, dy = \mathcal{F}_2[f(x,y)] \tag{A.12}$$

The Fourier transform maps to a circular frequency domain that can be written in either Cartesian coordinates or polar coordinates. Taking the Cartesian coordinates to be ($\omega_{x'}$, $\omega_{y'}$) and the polar coordinates to be (ω, φ), and the change of coordinates equations to be $\omega_{x'} = \omega \cos \varphi$ and $\omega_{y'} = \omega \sin \varphi$. Using this knowledge, equation A.12 can be written in the form of

$$P_\varphi(\omega) = F(\omega\cos\varphi, \omega\sin\varphi) = F\left(\omega_{x'}, \omega_{y'}\right)\big|_\varphi = F(\omega, \varphi) \tag{A.13}$$

Because $F(\omega_{x'}, \omega_{y'})$ is the 2D Fourier transform of f(x,y), the equations A.11–A.13 state mathematically that the 1D Fourier transform of the projection data through a given angle φ is the exact same as the radial data passing through the origin at the same angle φ in the 2D Fourier transform frequency domain. This is known as the projection theorem. This can be seen visually by combining a number of Figures from section 2.2.3 to create the

Figure shown here, Figure A.1.

The projection theorem is the basis for 3D reconstruction. Because of this theorem, the original sample can be reconstructed by doing a 2D inverse Fourier transform after the 1D Fourier transform has been performed on the projection data, which can be seen visually in section 2.2.3, Figure 2.11. This is written mathematically as

$$\begin{aligned}\hat{f}(x,y) &= \mathcal{F}_2^{-1}\left[F\left(\omega_x,\omega_y\right)\right]\\ &= \iint_{-\infty}^{\infty} F\left(\omega_x,\omega_y\right)\exp\left[i\left(x\omega_x + y\omega_y\right)\right] d\omega_x d\omega_y\\ &= \hat{f}(r,\theta)\end{aligned} \qquad \text{(A.14)}$$

By rewriting $\left(\omega_x,\omega_y\right)$ into polar coordinates (r,θ) into equation A.14, this becomes

$$\hat{f}(r,\theta) = \int_0^{\pi}\int_0^{\infty} F(\omega,\varphi)\exp[i\omega(x\cos\varphi + y\sin\varphi)]\,|J|d\omega\,d\varphi \qquad \text{(A.15)}$$

From the equations converting polar coordinates and Cartesian coordinates, and the change of coordinates equations in A.9, as well as knowing that the Jacobian |J| is defined

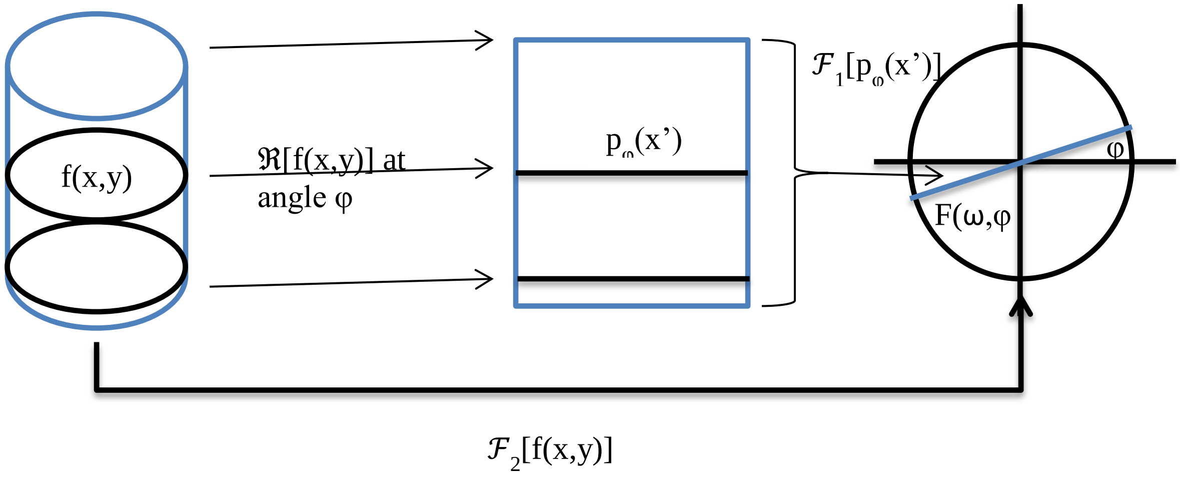

Figure A.1. Visual representation of projection theorem, where the 1D Fourier transform of the projection at angle φ is equivalent to the radial data running through the origin of the 2D Fourier transform of the original sample at the same angle φ.

as

$$|J| = \begin{vmatrix} \frac{\partial \omega_x}{\partial \omega} & \frac{\partial \omega_y}{\partial \omega} \\ \frac{\partial \omega_x}{\partial \varphi} & \frac{\partial \omega_y}{\partial \varphi} \end{vmatrix} = \begin{vmatrix} \cos\varphi & \sin\varphi \\ -\omega\sin\varphi & \omega\cos\varphi \end{vmatrix} = \omega\cos^2\varphi + \omega\sin^2\varphi = |\omega| \quad \text{(A.16)}$$

equation A.15 can be rewritten as

$$\hat{f}(r,\theta) = \int_0^{\pi} \int_{-\infty}^{\infty} |\omega| P_{\varphi}(\omega) \exp[i\omega(x\cos\varphi + y\sin\varphi)]\, d\omega\, d\varphi \qquad \text{(A. 17)}$$

after changing the integration limits to $0 \leq \varphi < \pi$ and $-\infty < \omega < \infty$ and replacing $F(\omega,\varphi)$ with $P_{\varphi}(\omega)$. At this point, the formula is complete and the original sample can be reconstructed from here. However, with a little more mathematical maneuvering, this equation can lead to the inverse Radon transform, which is interesting to see. To start, equation A.17 can be rewritten as

$$\hat{f}(r,\theta) = \int_0^{\pi} \mathcal{F}_1^{-1}\left[|\omega| P_{\varphi}(\omega)\right] d\varphi = \int_0^{\pi} \mathcal{F}_1^{-1}\left[\omega P_{\varphi}(\omega)\right] * \mathcal{F}_1^{-1}[sgn(\omega)]\, d\varphi \quad \text{(A.18)}$$

From here, by using Fourier transform tables, it is easy to see that the following substitutions can be made

$$\mathcal{F}_1^{-1}\left[\omega P_{\varphi}(\omega)\right] = \frac{1}{i2\pi} \frac{\partial p_{\varphi}(x')}{\partial x'}$$
$$\mathcal{F}_1^{-1}[sgn(\omega)] = -\frac{1}{i\pi x'}$$

Which transforms equation A.18 to

$$\hat{f}(r,\theta) = \int_0^{\pi} \frac{1}{i2\pi} \left(\frac{\partial p_{\varphi}(x')}{\partial x'} \right) * \left(\frac{-1}{i\pi x'} \right) d\varphi$$
$$= \frac{1}{2\pi^2} \int_0^{\pi} \int_{-\infty}^{\infty} \frac{\partial p_{\varphi}(x')}{\partial x'} \left(\frac{1}{x'-t} \right) dt\, d\varphi \qquad \text{(A.19)}$$

Because $\beta = \int_0^{\pi} d\varphi\, 1/\pi$ is a backprojection process and $\mathcal{H} = \int_{-\infty}^{\infty} \frac{\partial p_\varphi(x')}{\partial x'} \left(\frac{1}{x'-t}\right) dt/2\pi^2$ is a filtering process, equation A.19 becomes

$$\begin{aligned} \hat{f}(r,\theta) &= \beta\mathcal{H}\{p_\varphi(x')\} \\ &= \beta\mathcal{H}\{\Re[f(x,y)]\} \\ &= \Re^{-1}\{\Re[f(x,y)]\} = \hat{f}(x,y) \end{aligned} \tag{A.20}$$

and therefore the inverse Radon transform is defined by $\Re^{-1} = \beta\mathcal{H}$.

In order to expand this theorem to a 3D reconstruction, the 1D Fourier transforms in the above equations must be written as 2D Fourier transforms and the photons being emitted in all 4π directions must be taken into account, as well as the blur factor. Writing the 2D projection data as the 2D Fourier transformation,

$$\mathcal{F}_2\left[p_{\theta,\varphi}(s,t)\right] = F(\omega_s, \omega_t; \theta, \varphi) \tag{A.21}$$

Equations A.17 and A.18 can be combined together and rewritten, after expanding the Fourier transform and convolution operation to 2D instead of 1D and taking into account all 4π directions, to be

$$f(x,y,z) = \frac{1}{4\pi^2} \int_0^{\pi} d\theta \cos\theta \int_0^{2\pi} d\varphi\, [\mathcal{F}_2^{-1}[\rho] ** p_{\theta,\varphi}(s,t)] \tag{A.22}$$

where ρ is the filter to counteract the traditional 1/r blur factor when $\rho = (\omega_s^2 + \omega_t^2)^{1/2}$ and ** indicates a 2D convolution operator. This is the last mathematical concept used in the computer algorithm to solve the 3D reconstruction of a sample that will be reviewed here.

APPENDIX C

MATLAB CODE USED FOR DE RADIOGRAPHY

```
clear;
clc;
close all;
size=1014;
offset=49152;
% clears previous coding and any previously saved variables and defines variables for the
% size of the future images and the pixel offset to the center

p=3.8;
k1=–8.97e11;
k2=7.97e11;
k3=1.88e6;
k4=–1.16e6;
% defines calibration variables

name=sprintf('/uufs/cmes.utah.edu/home/u0562752/Desktop/FIPR XRM Data/Acid_Plant/FIPR_Acid_Plant_75_106_4X_slide41/FIPR_Acid_Plant_75_106_4X_80kV_slide41_reference.xrm');
```

```
fid=fopen(name,'rb');
fseek(fid,offset,'bof');
LER=fread(fid,size*size,'float32');
fclose(fid);
% opens lower energy reference image file and defines as a variable within Matlab to
% allow for future changes without changing original file and then closes original file
% while leaving variable still defined;  note that the reference file will change for each
% slide

name=sprintf('/uufs/cmes.utah.edu/home/u0562752/Desktop/FIPR XRM
Data/Acid_Plant/FIPR_Acid_Plant_75_106_4X_slide41/FIPR_Acid_Plant_75_106_4X_
140kV_slide41_reference.xrm');
fid=fopen(name,'rb');
fseek(fid,offset,'bof');
HER=fread(fid,size*size,'float32');
fclose(fid);
% opens lower energy reference image file and defines as a variable within Matlab to
% allow for future changes without changing original file and then closes original file
% while leaving variable still defined;  note that the reference file will change for each
% slide
for i=1:10
for j=1:4
% loops through all sections on slide for efficiency
```

```
name=sprintf('/uufs/cmes.utah.edu/home/u0562752/Desktop/FIPR XRM
Data/Acid_Plant/FIPR_Acid_Plant_75_106_4X_slide41/FIPR_Acid_Plant_75_106_4X_
80kV_slide41_%ix%i.xrm', i, j);
fid=fopen(name,'rb');
fseek(fid,offset,'bof');
LE=fread(fid,size*size,'float32');
fclose(fid);
% opens lower energy section jxi image file and defines as a variable within Matlab to
% allow for future changes without changing original file and then closes original file
% while leaving variable still defined

name=sprintf('/uufs/cmes.utah.edu/home/u0562752/Desktop/FIPR XRM
Data/Acid_Plant/FIPR_Acid_Plant_75_106_4X_slide41/FIPR_Acid_Plant_75_106_4X_
140kV_slide41_%ix%i.xrm', i, j);
fid=fopen(name,'rb');
fseek(fid,offset,'bof');
HE=fread(fid,size*size,'float32');
fclose(fid);
% opens higher energy section jxi image file and defines as a variable within Matlab to
% allow for future changes without changing original file and then closes original file
% while leaving variable still defined

X=((HER./HE))./((LER./LE));
```

```
% calculates relative reflex

Check = X;
% allows to output relative reflex value to verify code is correct

Th = X;
% defined for future use

Rad=reshape(X,size,size);
formatSpec='Radiography Image %ix%i';
example=sprintf(formatSpec,i,j);
save=sprintf('/uufs/cmes.utah.edu/home/u0562752/Desktop/FIPR XRM Data/Acid_Plant/slide41_radiographs_redo/slide41_%ix%i',i,j);
imwrite(Rad, save, 'tiff');
title(example);
% takes relative reflex back into image formatting and writes and saves relative reflex
% radiography image

Zeff=((k1*X+k2)./(k3*X+k4));
Zeff=Zeff.^(1/p);
Zeff(Zeff<0) = 0;
Zeff = reshape(Zeff,size,size);
% calculates effective atomic number and reshapes into image formatting
```

```
for row=1:size.*size
   for col=1:1
if Th(row,col)<0.70;
   Th(row,col)=1;
else
   Th(row,col)=0;
end
   end
end
% thresholding relative reflex so that the values smaller than 0.70 are set to 1 and the
% ones larger than 0.70 are set to 0

X = Check.*Th;
z1 = Zeff
z1 = z1.*reshape(Th,size,size);
% applies the 0 and 1 thresholding to effective atomic number image so that only values
% of interest appear on the image and reformats into proper image formatting

formatSpec='Calculated Zeff %ix%i';
last=sprintf(formatSpec,i,j);
save=sprintf('/uufs/cmes.utah.edu/home/u0562752/Desktop/FIPR XRM
Data/Acid_Plant/slide41_threshold_redo/slide41_%ix%i',i,j);
imwrite(z1, save, 'tiff');
```

```
title(last);

% writes and saves final thresholded image


end

end

% indicates end of coding for DE thresholding
```

REFERENCES

Beckhoff, B.; Kanngieber, B.; Langhoff, N.; Wedell, R.; Wolff, H. *Handbook of Practical X–Ray Fluorescence Analysis*; Springer: Berlin, 2006.

Carl Zeiss Inc. ZEISS Xradia 520 Versa. http://www.zeiss.com/ (Accessed July 2014).

Chapman, H. N.; Barty, A. ; Marchesini, S. ; Noy, A. ; Hau–Riege, S. P. ; Cui, C.; Howells, M. R.; Rosen, R.; He, H.; Spence, J.C. H.; Weierstall, U.; Beetz, T.; Jacobsen, C.; Shapiro, D. High–resolution ab initio three–dimensional x–ray diffraction microscopy. *J. Opt. Soc. Am.*, **2006**, *23*, 1179–1200.

Cho, Z.–H.; Jones, J. P.; Singh, M. *Foundations of Medical Imaging;* John Wiley & Sons Inc: New York, 1993.

Dutrow, B. L.; Clark, C. M. Geochemical Instrumentation and Analysis—X–ray Powder Diffraction (XRD). http://serc.carleton.edu/ (Accessed May 2014). The Science Education Resource Center at Carleton College.

Humphries, M. Rare Earth Elements: The Global Supply Chain. Congressional Research Service, 2013.

Limaye, A. *Drishti-volume exploration and presentation tool*. ANU Vizlab: Baltimore, 2006.

Lin, C. L.; Hsieh, C.-H.; Tserendagva, T.-A.; Miller, J. D.; Dual energy rapid scan radiography for geometallurgy evaluation and isoluation of trave mineral particles. *Miner. Eng.,* **2013***, 40*, 30–37.

Markowicz, A. An overview of quantification methods in energy–dispersive X–ray fluourescence analysis. *Pramana–J. Phys.*, **2011**, 321–329.

McAuliffe, M. *Medical Image Processing, Analysis and Visualization*. Center for Information Technology: Maryland, 2012.

Naydenov, S. V.; Ryzhikov, V. D.; Smith, C. F. Direct reconstruction of the effective atomic number of materials by the method of multi–energy radiography. *Nucl. Instrum. Methods in Phys. Res.*, **2003,** *B215*, 552–560.

Radiological and Environmental Management. Scanning Electron Microscopy. http://www.purdue.edu/ (Accessed March 2014). Purdue University.

Rasband, W. ImageJ 1.47v. 2014, National Institutes of Health, 2014.

Rhodes, G. *Crystallography Made Crystal Clear: A Guide for Users of Macromolecular Models.* Academic Press: San Diego, 2000.

Rosenfeld, A.; Kak, A. C. *Digital Picture Processing.* Academic Press, Inc.: Orlando, 1982.

Smythe, D. M.; Lombard, A.; Coetzee, L. L. Rare earth element deportment studies utilising QEMSCAN technology. *Miner. Eng.,* **2013**, *52*, 52–61.

Takahashi, Y.; Nishino, Y.; Tsutsumi, R.; Zetttsu, N.; Matsubara, E.; Yamauchi, K.; Ishikawa, T. High–resolution projection image reconstruction of thick objects by hard x–ray diffraction microscopy. *Phys. Rev. B: Condens. Matter,* **2010**, *82,* 214102.

Van Grieken, R. E.; Markowicz, A. A. *Handbook of X–Ray Spectrometry,* 2nd ed. CRC Press: New York City, 2001.

Xradia. *MicroXCT–400 User Manual, 4th ed*. Xradia, 2010.